Fall 12-20-2019

Theranostics for Antiretroviral Biodistribution and Pharmacokinetics

Brendan M. Ottemann
University of Nebraska Medical Center

THERANOSTICS FOR ANTIRETROVIRAL BIODISTRIBUTION AND PHARMACOKINETICS

By

Brendan Mark Freemon Ottemann

A DISSERTATION

Presented to the Faculty of

the University of Nebraska Graduate College

in Partial Fulfillment of the Requirements

for the Degree of Doctor of Philosophy

Pharmacology and Experimental Neuroscience Graduate Program

Under the Supervision of Howard E. Gendelman, M.D.

University of Nebraska Medical Center
Omaha, Nebraska

December, 2019

Supervisory Committee
Dr. R Lee Mosley
Dr. Yutong Liu
Dr. Jered Garrison
Dr. Balasrinivasa Sajja

TABLE OF CONTENTS

TABLE OF FIGURES

TABLE OF TABLES

ACKNOWLEDGEMENTS

First and foremost, I would like to thank my parents, Mark and Connie Ottemann. They have always supported me and my endeavors and have always been there for me, through good times and bad. Without their emotional support, wisdom and guidance I would not have made it as far as I have. I cannot put into words how much I truly appreciate their endless generosity and support which has pushed me through my struggles. My siblings Heather and Corbin Ottemann have been great friends to me throughout my life and I can't thank them enough for always reminding me to forge my own path in life and to do what I enjoy. I am deeply grateful for my family, as they have shaped me into the person I am today.

Next, I would like to thank my advisor, Dr. Howard Gendelman for giving me the opportunity to pursue my graduate degree in his laboratory. Dr. Gendelman has been an incredibly kind and supportive of me throughout my time in his laboratory. His impact on my development as a researcher cannot be understated. At the lowest point in my career, he reached out to me and gave me a chance to succeed. His patience and understanding have been beyond my comprehension. I can't thank him enough as he changed my life. In addition, he has provided valuable insight and expertise at every step, and for that I am very thankful. His examples and lessons of leadership both in my graduate education as well as numerous other students as been deeply impactful on me, and will continue to influence me as I proceed further into my career

I would like to extend my gratitude to the members of my committee: Dr. R. Lee Mosley, Dr. Balasrinivasa Sajja, Dr. Yutong Liu, and Dr. Jered Garrison. Their advice and guidance through my PhD was extremely helpful, and I greatly appreciate the time they provided. Their inputs and constructive criticism proved invaluable for the completion of my degree. I would also like to thank Dr. Benson Edgawa, Dr. JoEllyn McMillan, and Dr. Aditya Bade. They were also incredibly supportive during the completion of my PhD, and were always willing to lend helpful advice, both scientifically and emotionally. To them I am very grateful.

I also have a special place in my heart for my good friend Dr. Bhavesh Kevadiya, a postdoctoral fellow who guided me every day. First, he is a remarkable scientist and chemist. Endlessly patient, consistently good natured and kind, and relentlessly hardworking, Bhavesh truly is representative of the researcher I aspire to be. As the second author on the major manuscript of my thesis, his work and support has been immensely helpful for the completion of my degree. Without his expertise and contributions, particularly within the synthesis and characterization of our nanoparticles, the completion of my doctorate degree would not have been possible. Beyond the science, Bhavesh tirelessly worked to make me a better person, a better scientist, and a harder worker. For that and much more, I am eternally grateful, and wish him the best of luck as he continues on what surely will be a great scientific career.

I would also like to extend my gratitude to the members of the radiology core lab for having lent their expertise and assistance in the completion of my projects and were very kind and patient with me. Dr. Balasrinivasa Sajja, Melissa

Mellon, Ahmad Tanwir, Shea Lundeby and Lirong Xu have all provided support or guidance with my projects. I would not be here without their assistance. Additionally, I would like to thank Dr. Javier Seravalli who works at UNL and performed all of the ICP-MS/MS work that we needed. His endless patience and willingness to help were instrumental in the completion of my project.

Many thanks to our department administrative staff, Theresa Grutel, Lana Reichardt , Robin Taylor, Kim Morrison, Julie Ditter, Johna Belling, Myhanh Che, Na Ly, and Reed Felderman for their enormous administrative help and support throughout my Ph.D.

Lastly I would like to extend gratitude to my lab mates and close friends who made coming into laboratory each day a bit more fun and enjoyable: Dr. Christopher Woldstad, Dr. Brady Silman, Dr. Jimmy Hilare, Dr. Ted Kocher, Denise Cobb, Dr. Mary Banoub, Dr. Ibrahim Ibrahim, Insiya Mukadam, Tanmay Kulkarny, Mahmudul Hasan, Wilson Bloomberg, Ben Lamberty, Dr. Kelly Stauch, Katy Emmanuel, Hang Su, Jonathon Herskovitz, and many others. I wish each and every one of you continued success and happiness.

LIST OF ABBREVIATIONS

%ID/g	Percent Injected Dose per Gram
3TC	Lamivudine
ABC	Abacavir
AFM	Atomic Force Microscopy
AIDS	Acquired Immunodeficiency Syndrome
ANOVA	Analysis of Variance
ART	Antiretroviral Therapy
ARV	Antiretroviral
AZT	Azidothymidine
BD	Biodistribution
Bq	Becquerel
BSA	Bovine Serum Albumin
CAB	Cabotegravir
cART	Combination Antiretroviral Therapy
CCR5	CC Chemokine Receptor 5
CD4	Cluster of Differentiation 4
CD8	Cluster of Differentiation 8
CF	Cobalt Ferrite
Ci	Curie
CNS	Central Nervous System
CPMG	Car-Purcell-Meiboom-Gill
CSF	Cerebral Spinal Fluid
CT	Computed Tomography
CTL	Cytotoxic T-lymphocyte
CXCR4	C-X-C Chemokine Receptor Type 4
d4T	Stavudine
DAPI	4′,6-diamidino-2-phenylindole
DC	Dendritic Cells

DC-SIGN	Dendritic Cell–specific Intercellular Adhesion Molecule-3-grabbing Nonintegrin
ddC	Zalcitabine
ddI	Didanosine
DMEM	Dulbecco's Modified Eagle Medium
DMSO	Dimethyl Sulfoxide
DNA	Deoxyribonucleic Acid
DOPE	1,2-Dioleoyl-sn-glycero-3-phosphoethanolamine
DOTA	Dodecane Tetraacetic Acid
DSPE-PEG2000	1,2-distearoyl-phosphatidylethanolamine-methyl-polyethyleneglycol conjugate-2000
DTG	Dolutegravir
Env	Envelope
EuCF	Europium Cobalt Ferrite
FACS	Fluorescence-activated Cell Sorting
FCM	Flow Cytometry
gag	Group-specific Antigen
GALT	Gut-associated Lymphoid Tissue
GIT	Gastrointestinal Tract
gp	Glycoprotein
H&E	Hematoxylin and Eosin
HAART	Highly Active Antiretroviral Therapy
HIV	Human Immunodeficiency Virus
HLA	Human Leukocyte Antigen
HPC	Hematopoietic Progenitor Cells
HPLC	High-performance Liquid Chromatography
HRP	Horseradish Peroxidase
ICAM	Intercellular Adhesion Molecule
ICC	Immunocytochemistry

ICP-MS	Inductively Coupled Plasma Mass Spectrometry
InEuCF	Indium Europium Cobalt Ferrite
IS	Internal Standard
LA	Long Acting
LAMP-1	Lysosomal-associated Membrane Protein 1
LASER ART	Long-acting Slow Effective Release Antiretroviral Therapy
LN	Lymph Node
MDM	Human Monocyte-Derived Macrophages
MDR	Multi-drug Resistance
MHC	Major Histocompatibility Complex
MIP-1/2	Macrophage Inflammatory Protein ½
MRI	Magnetic Resonance Imaging
MRM	Multiple Reaction Monitoring
MS	Mass Spectrometry
MTT	3-(4,5-dimethylthiazol-2-yl)-2,5-diphenyltetrazolium bromide
Nef	Negative Regulatory Factor
NMDTG	Nanoformulated Myristoylated Dolutegravir
NMR	Nuclear Magnetic Resonance
NNRTI	Non-nucleoside Reverse-transcriptase Inhibitors
NRPV	Nanoformulated Rilpivirine
NRTI	Nucleoside Reverse Transcriptase Inhibitor
OCT	Optimal Cutting Temperature Compound
PBPK	Physiologically Based Pharmacokinetic
PBS	Phosphate-buffered Saline
PC	L-α-phosphatidylcholine
PCL	Polycaprolactone
PD	Pharmacodynamics
PDI	Polydispersity Index
PEG	Poly(Ethylene Glycol)

PFA	Paraformaldehyde
PI	Protease Inhibitor
PK	Pharmacokinetic
Pol	DNA Polymerase
PVA	Polyvinyl Alcohol
RANTES	Regulated on Activation, Normal T Expressed and Secreted
Rev	Regulator of Viral Protein Expression
RNA	Ribonucleic Acid
ROI	Region of Interest
RPV	Rilpivirine
RT	Reverse Transcriptase
SPECT	Single Photon Emission Computed Tomography
Tat	Trans-activator of Transcription
TEM	Transmission Electron Microscopy
TUNEL	Terminal Deoxynucleotidyl Transferase dUTP Nick EndLabeling
UPLC	Ultra-performance Liquid Chromatography
UV/Vis	Ultraviolet and Visible Absorption Spectroscopy
Vif	Viral Infectivity Factor
VLP	Virus Like Particles
Vpr	Viral Protein R
XRD	X-Ray Diffraction

ABSTRACT

RATIONALE: Our laboratories birthed the field of human immunodeficiency virus (HIV) theranostics. The new field allows simultaneous detection (diagnostics) and treatment (therapeutic) for the identification, treatment and inevitable elimination of virus in cell and tissue compartments. By employing theranostics, antiretroviral drugs (ARVs) can be tracked in lymph nodes, gut, spleen and liver. Cellular viral reservoirs including CD4+ T cell populations and mononuclear phagocytes (MP; monocytes, macrophages, microglia and dendritic cells) along with subcellular endosomal structures can now be targeted for drug delivery bringing therapeutics to areas where virus replicates. The overarching idea rests in improving precision targeted ARV delivery. Bringing ART to anatomically privileged tissues can be visualized and confirmed through single photon emission computed tomography (SPECT) imaging facilitated by multimodal antiretroviral drug (ARV) nanoprobes. To deploy such technologies, we have successfully placed rilpivirine into a theranostic nano system, taking advantage of state of the art physical and chemical properties of nano-sized particles for maximal biodistribution to viral sites. This allowed measurements of optimal antiretroviral responses. To achieve this outcome, we made particles with combinations of bioimaging detectors and ARV deliverers. This platform, in future studies, will utilize LASER ART and HIV-1 excision payloads (for example, CRISPR Cas9) for the inevitable elimination of viral infection. Our overall goal is to facilitate long-acting slow effective release antiretroviral therapy (LASER ART) development. To this end, in a first step analysis we created “multimodal imaging theranostic nanoprobes” with the hydrophobic antiretroviral drug rilpivirine (RPV). These unique nanoprobes allowed combined bioimaging, drug pharmacokinetics and tissue biodistribution tests in animal models. Combination of SPECT/CT and MR imaging modalities resulted in a highly accurate and sensitive nanoprobe. Because of this

combination, the imaging data acquired from these nanoprobes after administration in mice proved predictive of future drug pharmacokinetics and biodistribution.

METHODS: ^{111}Indium (^{111}In) and Europium (Eu3+)-doped cobalt ferrite (CF) rilpivirine (RPV)-loaded (^{111}InEuCF-RPV) nanoparticles were synthesized then fully characterized based on their size, shape and stability. The particles were tested *in vitro* for uptake, retention and antiretroviral efficacy in human monocyte-derived macrophages (MDMs) along with the intracellular location of particles. These were then used as platforms for nanoformulated drug biodistribution. For multimodal imaging and biodistribution studies; ^{111}InEuCF-RPV, ultra-small lipid coated ^{177}LuEuCF and NRPV particles were injected intravenously into mice at various concentrations of drug or radioisotope. One group was treated with ultra-small lipid-coated ^{177}LuEuCF particles at ~ 74 MBq (2000 µCi) to assess the effect of particle size on biodistribution. Drug levels were quantified in plasma and tissues by UPLC-MS/MS and cobalt levels were quantified by ICP-MS. Pearson's correlations were used to assess the predicative potential of imaging data and future ARV biodistribution and pharmacokinetics.

RESULTS: ^{111}InEuCF-RPV particles were synthesized and were shown to be of consistent size and were stable in a variety of different media conditions for over a week. Physiochemical characterizations and TEM imaging confirmed the structure and components of the system were correct. Formed theranostic particles were shown to be non-toxic to MDMs and at high concentrations were much less cytotoxic than native RPV. Particles demonstrated excellent intracellular relaxivity values of r_2 = 732.8 $mM^{-1}s^{-1}$ and thus served as excellent MRI contrast agents. Drug particles were detected in macrophage Rab compartments by dual fluorescence labeling. Replicate particles elicited sustained antiretroviral responses similar to nanoformulated RPV. After administration to Balb/c mice particles could be localized to the spleen, liver, as well as

popliteal and axillary lymph nodes. Imaging showed that nanoparticles accumulated in the spleen over 5 days and gradually left the liver as confirmed by *ex vivo* autoradiographic imaging and gamma scintillation spectrometry. Imaging data acquired up to 5 days proved predicative of drug biodistribution and pharmacokinetics up to 28 days post administration.

CONCLUSIONS: We conclude that this novel nano system can be used broadly for theranostic antiretroviral drug biodistribution. In particular, in the not so distant future, it will enable the merger of LASER ART with detection methods to realize the long term goal of improving patient outcomes by assessing where and to what levels antiretroviral drugs are delivered into viral compartments. The long term goals are to best prevent new infections, achieve viral elimination, and facilitate drug delivery to human immunodeficiency virus cell and tissue reservoirs.

CHAPTER 1
Introduction

1.1 Global significance of HIV

Human Immunodeficiency virus (HIV) is a progressive retrovirus of the human immune system which, if left untreated, can eventually lead to acquired immunodeficiency syndrome (AIDS). This virus represented a global pandemic shortly after its discovery in the early 1980's and at the time an HIV diagnosis was practically a death sentence. However since its discovery, HIV has been a major focus of medical research for several decades, with the molecular structure, function, regulation, tropism, and means of viral persistence having been documented [1-3]. Regardless of such efforts, more than 70 million people have been infected with HIV since its discovery and 35 million people have succumbed to the virus after initial infection [4]. Additionally, in 2018 there were approximately 38 million people living with HIV, with 1.7 million people becoming newly infected in 2018. Treatment and management of patients infected with the virus has become and continues to be one of the greatest challenges of the modern medical era.

Development of treatment options for patients infected with HIV is arguably one of the most significant victories in pharmaceutical research, with dozens of effective antiretroviral therapies (ART) being brought to market since azidothymidine (AZT) was first approved in 1987 [5, 6]. There is no cure for HIV infection. However, effective antiretroviral (ARV) drugs can control the virus and help prevent transmission so that people with HIV, and those at substantial risk, can enjoy healthy, long and productive lives. Furthermore, more recent innovations

in ART technology have allowed concurrent administration of multiple antiretroviral compounds to patients, drastically increasing their effectiveness in limiting HIV replication and inhibiting viral resistance. Combination ART (cART) markedly reduces HIV replication such that HIV RNA is undetectable within plasma, which halts further loss of $CD4^+$ T cells and prevents progression to AIDS [7, 8]. However, despite such pharmacological advances and sustained viral suppression, ART cannot eliminate viral infection. Complete viral eradication will require the development of novel drug technologies, with improvements in drug design and delivery being at the forefront of significance

1.2 HIV-1 virology

1.2.1 Structure of HIV

HIV is a retrovirus, whose genome encodes its own reverse transcriptase which, after translation by the host cell, is used to transcribe single stranded viral RNA into a double stranded DNA that can be integrated into the host genome. HIV isolates are currently grouped into two types, HIV-type 1 (HIV-1) and HIV-type 2 (HIV-2) [9, 10]. The worldwide main agent of AIDS is HIV-1, while HIV-2 is restricted to some regions of Western and Central Africa [11]. However, both tropisms share many similarities in terms of genetics and structure. HIV is a genetically related member of the lentivirus genus of the retroviridae family. Infections with lentiviruses typically show a chronic course of the disease, with a long period of clinical latency, persistent viral replication, and involvement of the central nervous system [12].

Two identical copies of single stranded RNA reside within the cylindrical capsid of the virus and are characterized by the presence of structural genes *gag, pol, env* [1, 13]. The group-specific antigen gene, or *gag*, encodes the proteins that comprise viral core and matrix, such as viral capsid proteins HIV p24, p6 and p7. *Gag* also encodes matrix protein HIV p17 [14]. The *env* gene encodes proteins that form the viral envelope, specifically glycoprotein 120 (HIV gp120) and transmembrane glycoprotein 41 (HIV gp41). The *pol* gene encodes for enzymes crucial for viral replication, which are the reverse transcriptase that converts viral RNA into DNA, the integrase that incorporates the viral DNA into host chromosomal DNA (the provirus), and the protease that cleaves large gag and pol protein precursors into their functional proteins. [15]. All three genes are critical for the propagation of HIV within an infected host, and as such these genes and the proteins they encode have become biological targets of antiretroviral drug (ARV) therapy.

In addition to these enzymes, several genes that encode accessory and immune-regulatory proteins play a vital role in viral infectivity. Trans-activator of transcription, or Tat, causes substantially increased levels of reverse transcription to occur after a small number of RNA transcripts are made via a positive feedback loop [14]. Regulator of viral protein expression, or Rev, dictates the movement of RNA from cytoplasm to nucleus. Other necessary proteins include viral protein R (Vpr), viral infectivity factor (Vif), negative regulatory factor (Nef), and HIV-1p7 [16]. While the biological mechanism in which Vpr, Vif, and Nef influence HIV-1

replication are not completely known, it has been established that these proteins positively affect HIV-1 replication.

HIV viral particles have a diameter of 100 nm and are surrounded by a lipoprotein-rich membrane. Each viral particle membrane includes glycoprotein heterodimer complexes composed of trimers of the external surface gp120 and the transmembrane spanning gp41 glycoproteins bound together [17, 18]. During the process of budding from the infected cell (discussed in the next section), the virus may also incorporate into its membrane different proteins from the host cell membrane, such as HLA class I and II proteins, or adhesion proteins such as ICAM-1 that may facilitate adhesion to other target cells [19].

The primary target of progeny infectious HIV-1 and the most commonly infected cell is the CD4+ T lymphocyte [20, 21]. This was shown by isolation, propagation and molecular analyses of the viral genome in HIV-1 infected patients [22, 23]. These investigations definitively showed that proviral DNA is integrated within the genomes of CD4+ T cells and to more limited degree monocyte-macrophages [24]. Indeed, impaired immune response is characteristic of all stages of the disease with parallel deficits in $CD4^+$ T cell numbers and function [25].

1.2.2 The HIV replication cycle

The HIV replication cycle can be summarized in six steps; 1) binding and entry; 2) uncoating; 3) reverse transcription; 4) provirus integration; 5) virus protein

synthesis and assembly and 6) budding. The entry process of HIV-1 and HIV-2 can be divided into three major events: virus binding to the cell, activation and fusion. The viral envelope trimeric complex, composed of the heterodimer proteins gp120 and gp41, is essential for virus recognition and entry into target cells [26]. HIV gp120 binds a 58 kDa monomeric glycoprotein, designated as CD4, which is expressed on the cell surface of circulating T-lymphocytes, on T-cell precursors within the bone marrow and thymus, monocytes/macrophages, eosinophils, dendritic cells and microglial cells of the central nervous system [27-30]. The CD4 molecule normally functions as a co-receptor of the major histocompatibility complex class II molecule during T-cell recognition of a foreign antigen [31]. Upon gp120 binding with the CD4 protein, the virus envelope complex undergoes a structural change, exposing a specific domain in the gp120 protein that is able to bind chemokine receptors, which function as viral “co-receptors”, on the cell membrane. The most common co-receptors used by HIV are CCR5 and CXCR4, but other potential co-receptors have been described [32, 33]. The double binding of gp120 to both CD4 and one chemokine receptor creates a more stable two-pronged attachment of the virus, which in turns allows the N-terminal fusion peptide gp41 to penetrate the cell membrane, eventually leading to fusion of the cell and viral membranes [34].

Following membrane fusion, the virus core uncoats into the cytoplasm of the target cell freeing the viral RNA (uncoating). The conversion of viral RNA into proviral DNA takes place because of the action of the reverse transcriptase [35]. The integration of proviral DNA is accomplished via the integrase enzyme and the

expression of the provirus requires that the target cell is in an activated state [36, 37]. Monocytes/macrophages, microglial cells, and latently infected quiescent CD4+ T-cells contain integrated provirus and are important long-living cellular reservoirs of HIV [38]. Upon cell activation, transcription of proviral DNA into a messenger RNA occurs. Transcription process initially results in the early synthesis of regulatory HIV proteins such as Tat and Rev. Tat binds to the TAR site (Transactivation Response Element) at the beginning of the HIV RNA in the nucleus and stimulates the transcription and the formation of longer RNA transcripts. Rev also facilitates the transcription of longer RNA transcripts but it also induces expression of structural and enzymatic genes while inhibiting the production of regulatory proteins, therefore promoting the formation of mature viral particles [39-41].

Viral messenger RNA coding for large precursor proteins migrates into the cytoplasm, where structural proteins of new virions are synthesized. The proteins coded by *pol* and *gag* genes form the nucleus of the maturing HIV particle and the gene products coded by the *env* gene form the glycoprotein spikes of the viral envelope [42-44]. Large gp160 precursor molecules are cleaved by the cellular proteases into gp120 and gp41 [45]. The viral protease, integrase, RNase H, and reverse transcriptase (RT) are always expressed within the context of a Gag-Pol fusion protein, the gag-pol precursor (gp160).

The cleavage of the precursor molecules by the HIV protease is necessary for the generation of infectious viral particles. The formation of new viral particles is a stepwise process: two viral RNA strands associate together with replication

enzymes, while core proteins assemble over them forming the virus capsid. This immature particle migrates towards the cell surface. Large precursor env molecules are then cleaved by the HIV protease, resulting in new infectious viral particles, which bud through the host cell membrane thus acquiring a new envelope [46]. During the budding process, the virus lipid membranes may incorporate various host cell proteins and become enriched with phospholipids and cholesterol. Ultimately, the massive release of HIV virion leads to the death of the $CD4^+$ T cells [47].

Importantly, reverse transcription is completed by HIV enzymes utilizing the infected host cell's deoxynucleotides. Viral DNA synthesis occurs concurrently with the degradation of the original viral RNA, as the reverse transcriptase enzyme also has RNase activity. During each iteration of RNA to DNA reverse transcription within an infected host cell, the probability of a random mutation is relatively high due to reverse transcriptase's relatively poor proof reading capabilities [48]. This is what allows HIV to develop viral mutations over time that potentially are beneficial to its propagation within the host, such as developing ART resistance. Reverse transcription is performed twice to produce a double stranded DNA molecule, after which there is binding to the viral integrase enzyme. Integrase can then transport the double stranded viral DNA into the nucleus of the host cell as well as creating a cut within the host cell genome for viral DNA integration [49].

1.3 Viral transmission

Transmission occurs by separate routes (through contaminated needles, by transfusion of blood and blood products, from mother to fetus and by receptive

anal or vaginal intercourse) [50]. The actual process ensues through cells or by the virus itself. As per the latter, HIV is released to float freely within plasma until they come in contact and interact with a host cell suitable for entrance and infection. “Cell-to-cell transmission” is the alternative mechanism for the progression of HIV infection, in which direct contact between an infected cell with an uninfected naïve cell results in HIV transmission. Cell-to-cell transmission occurs during the fusion of HIV infected cells with that of uninfected susceptible cells; the fusion process causes the viral components to be deposited into the uninfected cell, subsequently causing multinucleated giant cells [51, 52].

1.4 Immune Response to HIV-1

AIDS occurs as a consequence of progressive viral infection and CD4+ T cell depletion. It is classified as patients infected with HIV-1 that have CD4+ T cell counts below 200 per µl, which compromises cell-mediated immunity. This lack of cell-mediated immunity leaves patients extremely vulnerable to opportunistic viral, fungal, parasitic and mycobacterial infections as well as immune related cancers that are strongly associated with advanced HIV infection [16, 53]. Ultimately, patients succumb to HIV not directly from the virus itself, but rather indirectly as opportunistic infections take advantage of a weakened and dysfunctional immune system. However, the progression of the HIV disease state, from initial infection/transmission to complete immune failure, is a process taking many years or even decades, and is characterized into several distinct stages defined by the current immune response [54]. These four stages are: primary infection, a clinically asymptotic period, symptomatic HIV infection, and HIV to AIDS progression. Each

infected individual varies in their respective length, severity, and symptoms of each stage; it is of importance to mention that patients consistently taking ARV medication generally will not progress to the later stages of the disease [54].

Primary infection is the beginning of HIV disease progression as the virus establishes itself within the host body. This stage typically lasts only a few weeks after initial transmission. Within the first 24 hours after infection, HIV virions infect dendritic cells within the mucous membrane; after about 5 days, these infected dendritic cells are recruited to lymph nodes and the peripheral blood, where replication rates dramatically increase. The primary infection stage is characterized by substantially decreasing CD4+ T cells and exponentially increasing levels of viremia, often millions of virus copies per milliliter of plasma [55]. Such a large number of HIV viral particles within the blood allows for systemic infection of peripheral lymphoid organs. Regardless of this viral spike, the body's immune response during primary infection eventually results in reduction of virus levels within the peripheral blood. Virus specific cytotoxic T lymphocytes (CTLs) appear early in infection and potentially downregulate HIV replication [56, 57]. CD8+ T cells are also credited in controlling the initial viremia peak that is characteristic of primary infection; activated and mature CD8+ T cells possess different anti-HIV processes. Specifically, CD8+ T-cells can release cytokines such as RANTES, MIP-1 alpha, and MIP-1 beta that can effectively block the entry of HIV into host cells by competing for or downregulating cellular co-receptor CCR5 [56, 57]. Following a severe reduction in plasma viremia and a small rebound in CD4+ T-cell populations, patients progress to the clinically asymptomatic stage.

The period of time between the initial primary infection stage and the development of AIDS is classified as the clinically asymptomatic stage. After the initial viremia peak and subsequent decrease in HIV plasma characteristic of the primary infection stage, HIV continues to replicate within infected cells and is readily detected in almost all lymphoid tissue [58, 59]. Consistent viral replication results in chronic immune stimulation; this strain on the immune system is thought to be responsible for its eventual deterioration as well as the progressive death of lymphoid tissue [60]. Despite continual propagation of the virus and gradually decreasing CD4+ T-cell populations, infected patients generally don't exhibit any clinical symptoms at this stage, as immunodeficiency has not progressed enough to compromise cell-mediated immune function.

The final phase includes both the stage of symptomatic HIV infection as well as the progression of HIV-1 to AIDS. While the immunological hallmark of the progression from the asymptomatic stage is gradual loss of CD4+ T-cells, the symptomatic stage is defined by a steeper decline in CD4+ T cell populations and overall increase in systemic viral load [61]. This is due to systemic viral replication at multiple sites in addition to the high amount of replication happening within lymphoid tissue. The amount of time required for the development of clinical immunodeficiency from the asymptomatic stage is variable among infected individuals: indeed, the complexity of host and viral factor interactions are integral to the eventual outcome of the disease [54]. Overall, low amounts of viral replication and retention of immune function favors a slow progression of HIV

infection, while high viremia and immune dysfunction leads to a more rapid disease progression.

1.5 HIV-1 reservoirs

The establishment and maintenance of HIV reservoirs that lead to persistent viremia in patients on antiretroviral drugs remains the greatest challenge of the HAART era. Cellular reservoirs include resting memory $CD4^+$ T lymphocytes, which are implicated as the major HIV reservoir [62]. Some anatomical reservoirs that may harbor such cells include the central nervous system, the gastrointestinal tract and the gut-associated lymphoid tissue, other lymphoid organs, and the genital tract [63, 64]. The presence of immune cells and other HIV susceptible cells, occurring in differing compositions in anatomical reservoirs, coupled with variable and poor drug penetration that results in suboptimal drug concentrations in some sites, are all likely factors that fuel the continued low-level replication and persistent viremia during treatment [65, 66]. Latently, HIV- infected CD4+ T cells harboring replication-competent virus, HIV cell-to-cell spread, and HIV- infected T cell homeostatic proliferation due to chronic immune activation represent further drivers of this persistent HIV viremia during highly active antiretroviral therapy [67].

1.5.1 Genital tract

Evidence suggests that both male and female genital tracts may be important reservoirs of HIV. In the male genital tract, drug resistance persists longer than in blood that may indicate local drug penetration barriers and independent selection pressures although antiretroviral therapy can effectively reduce HIV-1 levels in semen [68]. Even with antiretroviral therapy, irregular

seminal HIV shedding can occur [69]. This may be due to the presence of both the virus and CD4+ T lymphocytes in semen, which support and provide an environment for continued replication within the seminal tract [70]. In females, HIV is also archived in the genital tract early in infection and has been detected in some women with undetectable levels in blood. Mutation patterns from blood and genital tract specimens may differ and even within the genital tract, viruses from cervicovaginal lavage specimens exhibited genetically distinct characteristics when compared to viruses from endocervical secretions which supports the theory of this tissue acting as a viral reservoir [71]. Low-level HIV replication in the male and female genital tract remains a possible explanation for persistent viremia during HAART possibly because of poor drug penetration and suboptimal drug concentrations and the presence of infected long-lived cells in these compartments [72].

Additionally, activated cells in the genital tract mucosa are very important for the initial establishment of infection and the spread of virus to different reservoirs. Dendritic cells (DCs) in the genital tract mucosa are the main HIV targets during sexual transmission [73, 74]. Dendritic cells express the HIV receptors CD4, chemokine receptors CCR5 and CXCR4 together with CD209 protein, also known as dendritic cell–specific intercellular adhesion molecule-3-grabbing nonintegrin (DC-SIGN) [75]. The DC-SIGN enhances infection through high affinity binding to the HIV glycoprotein gp120, aiding transmission of the virus to T lymphocytes [76]. HIV particles in DC-SIGN–positive cells are not degraded and can remain stable and infectious for more than 9 months [76, 77].

1.5.2 Lymphoid Organs

After initial exposure to antigen presenting DC-SIGN–positive DCs at mucosal surfaces, the virus is internalized, processed, and presented to T lymphocytes initiating an adaptive immune response [55]. HIV takes advantage of immature DCs in the genital tract, which capture the virus to gain access to lymphoid tissue compartmentalized CD4+ T cells. HIV then replicates in CD4+ T cells in the lymph nodes before infected T cells and free viruses enter the thoracic duct and spread into the bloodstream, to other lymphoreticular tissues and immune-associated organs such as the thymus, bone marrow, gut-associated lymphoid tissue (GALT), and spleen, and CNS [55, 78, 79]. Persistent replication in lymph nodes and lymphatic tissues despite HAART and lower concentrations of the antiretroviral (ARV) drugs compared to levels in peripheral blood provides a “hiding place” for HIV in this compartment [80]. Animal model studies have demonstrated that the lymph nodes may harbor viral reservoirs responsible for virological failure if treatment is terminated whereas some drugs such as nonnucleoside reverse transcriptase inhibitor efavirenz, the nucleoside/nucleotide reverse transcriptase inhibitor drugs tenofovir and emtricitabine, and atazanavir a protease inhibitor have all been shown to have much lower levels in lymph nodes compared to peripheral blood.

Spleen and bone marrow may also be important HIV reservoirs with studies showing increased splenic inflammatory activity in HIV- infected individuals compared to noninfected individuals. Abnormalities in hematopoietic progenitor cells (HPCs) due to bone marrow infection and the establishment of latent HIV

infection have also been reported. Not much is known about the importance of the thymus as an HIV reservoir, but in vitro infection of thymocytes by HIV has been reported [79]. In vivo studies show that HIV can infect the thymus and is accompanied by increased activation and depletion of CD4+ T cells [81]. Animal model studies using bone marrow-liver-thymus–humanized mice demonstrated that ARV drugs adequately penetrated the human thymic organoid but did not eliminate HIV replication in this tissue or other tissues including the spleen and lymph nodes, further highlighting these tissues as possible reservoirs and sources of persistent viremia during HAART [82].

1.5.3 Gastrointestinal Tract

The GIT contains a high proportion of the total lymphocytes in the body through the GALT that also harbors numerous innate immune cells such as macrophages and DCs making this a favorable site for both HIV acquisition and replication [83, 84]. Prolonged immune activation results in depletion of GALT lymphocytes early in infection and levels remain depressed for the duration of the disease with incomplete restoration during HAART despite undetectable virus levels in the blood [85]. Early initiation of HAART also does not seem to completely restore and prevent CD4+ T cell activation and depletion in the GALT although it may aid in maintaining homeostasis in the GALT mucosa [86, 87].

The HIV persistence in GALT even after 10 years of therapy has been reported with evidence of peripheral blood mononuclear cell infection from this reservoir [85]. As a major site of HIV replication, a mechanism underlying HIV persistence in the GIT and GALT may be the persistent immune activation caused

by antigenic stimulation of resting T and B cells resulting in their proliferation and increased turn- over providing HIV with a constantly available source of susceptible cells [88]. In addition to CD4+ T lymphocytes, the GIT macrophages and follicular DCs may also significantly contribute to the reservoir size of the GIT. Considering the large size of the GIT-associated mucosa, these cells have been reported as a significant source of viral RNA in this reservoir [83].

1.5.4 Central Nervous System

Different routes have been proposed by which HIV can invade the brain, and these include access through the blood-brain barrier, the choroid plexus, and the CSF [89, 90]. On entering the CNS, HIV has access to susceptible microglial cells and macrophages, which express the CD4 primary receptor and CCR5 chemokine co-receptor [91]. Other CNS cells not bearing the primary CD4 receptor such as astrocytes can also be infected by HIV, but the mechanisms involved are still not well understood [92]. The virus may remain detectable in the CSF 10 years after initiation of therapy, and there is strong evidence of the CNS acting as an HIV reservoir and site that supports low-level replication [93, 94]. Suboptimal ARV drug levels in the CNS most likely result in continued replication in this compartment leading to the selection for neurotropic variants and development of neurological symptoms in patients with undetectable plasma virus levels [95-97]. In line with this, drugs with better CNS penetration seem to result in improved outcomes [98, 99].

1.5.5 Cellular Reservoirs

Resting memory CD4+ T lymphocytes are the major cellular HIV reservoir, and this source is considered a major barrier to HIV eradication during HAART [100]. These cells harbor inactivated HIV proviral DNA that persists for long periods despite treatment. This reservoir is suspected to be the source of persistent low-level viremia in patients on HAART who otherwise seem to have suppressed the virus [101]. Macrophages are also a source of persistent HIV viremia during HAART although their exact role is still controversial [102]. These cells can withstand the cytopathic effects of viral infection, which gives them an extended period of existence during which they produce and release large numbers of viruses [103, 104]. Follicular DCs are also a potential cellular reservoir as they can trap infectious HIV on their surfaces for months and lead to CD4+ T lymphocyte infection [105]. HIV can also infect hematopoietic precursor cells that include mast cell progenitors, multipotent HPCs, and monocytes which suggests that HPCs can act as a cellular reservoir [79, 106-108].

Cellular reservoirs in the brain may include non-CD4+ cells such as astrocytes and microglia [109]. The HIV replication in astrocytes is known to be very low and only a few astrocytes are infected, but since astrocytes are an abundant cell type in the brain, the infection of a small percentage of these cells may have significant results in regards to neurotoxicity and brain cells damage. The slow turnover of glial cells also means that infected cells could potentially harbor the virus for several years [110, 111].

1.6 Antiretroviral therapy (ART)

The natural progression of HIV infection that is described in the previous section is dependent on infected individuals not being administered any HIV specific treatment during their infection. This is representative of the clinical landscape in the decade following the discovery of HIV-1 in 1983, in which medical professionals knew very little about the virus and its pathology. Treatment options were limited if not non-existent during this period; testing positive for HIV was universally fatal, with survival time directly dependent on the individual's own progression from initial infection to AIDS.

This changed in 1987 with the development and testing of a dideoxynucleoside reverse transcriptase inhibitor (NRTI), azidothymidine (AZT), the first antiretroviral drug used to treat HIV [6]. Benefits of AZT treatment were limited; greater survival times were found in patients at 24 weeks, but this effect was short-lived and by 48 weeks' time, survival benefits were no longer observed [112, 113]. Additionally, AZT treatment showed side effects of transient anemia and malaise due to off target toxicities, particularly in high doses given to HIV patients shortly after approval. Regardless of AZT's limitations, the effects seen on the survivability of HIV patients spurred medical research to investigate the potential of antiretroviral therapy. Three additional NRTIs were then released in quick succession: zalcitabine (ddC), didanosine (ddI), and stavudine (d4T). All three medications had particular toxicities and as of present none are widely administered within the clinic [114, 115]. However, the development and administration of these early antiretroviral drugs, and their associated toxicities, inevitably led physicians to give treatment sequentially or to alternate between

different therapies, a strategy that would serendipitously prove effective as more antiretrovirals became developed [116]. Patients continued to fare poorly within the clinic, but with small reductions in the rate of adverse reactions there was optimism antiretroviral research was heading in the right direction.

Combination NRTI therapy, in which two or more antiretrovirals are given as a treatment concurrently, was another clinical concept that showed encouraging results in the early 1990s. The development of lamivudine (3TC), a cytidine analog, allowed for another drug to be used in combination with other NRTIs and proved to be synergistic with the other compounds [117]. But despite such progressions, the quality of life for HIV patients continued to be poor. Triple drug combination strategies were the only cases showing any sign of significantly controlling HIV infection, and early NRTIs, particularly thymidine analogs, continued to have issues with toxicity [115].

The development of different classes of ARVs was perhaps the most substantial advancement of HIV-1 therapeutics. Groups of drugs that have a direct effect on HIV viremia but do so via different biological mechanisms; when given in combination, have proved effective at limiting viral resistance while decreasing viral plasma levels. Saquinavir became the first protease inhibitor (PI) approved in 1995, but initial formulations struggled with poor bioavailability and deactivation by enzymatic metabolization [115]. Ritonavir, another PI, was developed shortly after saquinavir. Ritonavir was found to be a potent inhibitor of one of the enzymes responsible for deactivating saquinavir, and when given in combination, dual saquinavir and ritonavir administration was found to be quite effective at HIV

suppression, though tolerability was low [118]. Eventually it was determined that high-dose saquinavir and low-dose ritonavir in combination was optimal for effective protease inhibition, and still represents the recommended usage for protease inhibition in the clinic at present [115]. Nevirapine became the first non-nucleoside reverse transcriptase inhibitor (NNRTI) to be approved in 1996, and it was found that if given as a monotherapy that resistance develops relatively quickly. But with nevirapine given as part of three-drug regimen, in which two NRTIs are also administered, HIV was found to be nearly completely suppressed and proved superior to dual therapy NRTI control groups in the Italy, Netherlands, Canada, Australia Study (INCA Study) [119].

Different classes of ARV medications, which in turn could be given to patients in a variety of different combinations, ultimately proved the key in defeating HIV conferred drug resistance. Such drug regimens become referred to as “highly active antiretroviral therapy” (HAART) and truly marked a turning point in the battle against the HIV pandemic. A substantial decrease in HIV associated morbidity and mortality associated with HAART administration changed the world: the leading cause of death among young people within developed countries had become augmented to a chronic but manageable affliction [120]. Perpetual variety in HAART treatment not only prevents HIV for developing resistance to specific ARVs but also prevents HIV replication to the point where plasma viral levels are undetectable [121]. To date, there are five different classes of antiretroviral medications: NRTIs, NNRTIs, PIs, entry/fusion inhibitors, and integrase inhibitors.

- **Nucleoside/Nucleotide reverse transcriptase inhibitors (NRTIs)** work to inhibit the enzyme responsible for the transcription of the viral RNA into

DNA for integration. This is accomplished by NRTIs being nucleoside analogs; they compete with natural deoxynucleotides within the cell for incorporation into the growing DNA strand during reverse transcription. Such analogs lack the 3' OH group needed to successful chain elongation. When the next deoxynucleotide is incorporated into the growing DNA chain, the 5' to 3' phosphodiester bond needed for continuation cannot be formed. Failure to form this bond halts the process, effectively preventing viral RNA from being reverse transcribed [122]. Currently approved NRTIs used in treatment of HIV include: Zidovudine, Didanosine, Zalcitabine, Stavudine, Lamivudine, Abacavir, and Tenofovir. It should be noted that Tenofovir is a unique type of NRTIs. Nucleoside analogs normally undergo phosphorylation to be converted into nucleotides, which become active for incorporation. Tenofovir is administered as an already chemically active nucleotide analog, with no need for activation via phosphorylation [123, 124].

- **Non-nucleoside reverse transcriptase inhibitors (NNRTIs)** again inhibit the transcription of viral RNA into DNA but do so by more direct means. NNRTIs non-competitively bind to an allosteric site on reverse transcriptase, resulting in a confirmation change and inactivation of the enzyme [125]. If given as a monotherapy, HIV-1 resistance to NNRTIs can be established fairly quickly due to mutations in reverse transcriptase during continual iterations of replication; mutations in which NNRTIs cannot bind to the RT allosteric site are positively selected for [126, 127]. Because of this, NNRTIs are commonly given in conjunction with one or two other NRTIs. Currently approved NNRTIs include: Nevirapine, Delavirdine, Efavirenz, Emtricitabine, Etravirine, and Rilpivirine [128, 129].

- **Protease Inhibitors (PIs)** effectively prevent the maturation and release of newly synthesized viral proteins by inhibiting the enzyme needed for their cleavage and subsequent activation [130]. As described above, once viral RNA has been reverse transcribed into DNA and integrated into the host genome, viral proteins are transcribed by host cell machinery to produce new viral particles. Newly synthesized viral proteins must become cleaved by the viral protease to become fully activated and infectious. PIs bind to the active site of viral proteases, preventing them from having enzymatic activity and inhibiting the completion of HIV-1 life cycle [131]. Currently approved PIs include: Saquinavir, Ritonavir, Nelfinavir, Amprenavir, Lopinavir, Atazanavir, Fosamprenavir, Tipranavir, and Darunavir [132, 133].
- **Entry and fusion inhibitors** are a relatively new class of ARV drugs with only 3 compounds currently being approved for HIV treatment: Enfuvirtide, approved in 2003, Maraviroc, approved in 2007, and Ibalizumab in 2018 [134, 135]. For entrance of HIV into a host cell, viral envelope surface glycoproteins must interact with membrane surface receptors. HIV envelope glycoproteins are normally a heterotrimer consisting of three molecules of gp120 and three molecules of gp41. Binding of viral gp120 to the CD4 receptor of a host cell causes a conformational change in the glycoprotein, allowing interaction with host cell co-receptors CCR5 or CXCR4. Co-receptor binding ultimately allows fusion between the host cell membrane and portions of gp41 within viral envelope. Enfuvirtide is a synthetic oligopeptide whose sequence corresponds to that of the HR-2 region of the HIV-1 envelope gp41 subunit. Binding of enfuvirtide to the trimeric HR-1 complex prevents the association of HR-1 with HR-2, thereby

inhibiting fusion and blocking virus entry [136]. Maraviroc is a small molecule with high affinity for the co-receptor CCR5, binding to it and preventing association with gp41, effectively inhibiting entry into cells with the CCR5 co-receptor [137]. Ibalizumab is a recombinant humanized monoclonal antibody, and represents the first novel agent for HIV-1 management in over a decade and is the first monoclonal antibody for the treatment of multi-drug resistant (MDR) HIV-1 infection in combination with other forms of antiretroviral therapy in heavily treatment-experienced adults who are failing their current antiretroviral regimen [138, 139]. Ibalizumab has a novel mechanism of action that is worth discussing. Ibalizumab binds to the CD4 T cell extracellular domain on the interface between domains 1 and 2 of human CD4, on a surface opposite of the site where gp120 and the major histocompatibility complex II (MHC-II) molecule bind on domain 1 [135]. Traditionally, when the HIV envelope gp120 binds to CD4 T cell extracellular domain 1, a conformational shift occurs that causes the V1 and V2 loops to expose the V3 loop, which converts the trimer from the closed state to an open state [140, 141]. Ibalizumab binding prevents these conformational changes and subsequently inhibits the interaction of gp120 with CCR5 and CXCR4 co-receptors via the V3 loop. It also prevents conformational changes in gp41 that are needed for membrane fusion [142]. This novel mechanism of action makes ibalizumab effective against CXCR4- and CCR5-tropic strains and led to its classification as a parenteral CD4-directed post-attachment inhibitor [138, 143].

- **Integrase inhibitors** were developed to block the enzyme responsible for the integration of newly synthesized HIV DNA into the host cell genome. Integrase catalyzes two reactions within the HIV replication life cycle. The

first is 3' end processing in which two nucleotides are removed from one or both of the 3' ends of the viral DNA, while the second is the "stand transfer reaction" in which the processed 3' ends are covalently bound to host chromosomal DNA. Inhibition of integrase prevents these steps from occurring, effectively preventing the infection of the host cell [144-146]. Currently approved integrase inhibitors are: Raltegravir, Dolutegravir, Elvitegravir, and Bictegravir [146, 147].

Despite such significant advancements in the development of HIV-1 treatment options, complete eradication of HIV-1 remains an extremely active subject of research. Though HAART can reduce plasma viral levels to undetectable levels and allow patients to live decades after their initial infection and diagnosis, HIV-1 continues to persist throughout the world.

1.6.1 LASER ART

ART has transformed the prognosis of HIV infection from certain death to a manageable chronic disease by reducing plasma viral loads to undetectable limits and preventing $CD4^+$ T cell depletion. However, achieving this requires strict adherence to drug regimens as prolonged or frequent deviations from this can result in viral rebound, and in some cases viral mutations that render the current treatment ineffective. In fact, adherence to antiretroviral medications continues to be a major predictor of treatment success (and source of variability in outcomes in clinical practice and research studies) [148]. It is true that newer medications have become safer and easier to take; most of them are now co-formulated in a single tablet that is taken once-a-day. However, ART adherence is still challenged by multiple individual (i.e., education, health literacy, poverty, substance use) and

community or structural (i.e., stigma, disclosure, access to care) barriers that limit its durability [149].

With the goal of improving regimen adherence and thus treatment outcomes researchers have been actively developing long-acting ARVs [150-154]. Generally, ART medication has been given as oral medication and thus drug design has focused on aqueous solubility of drugs. Long-acting ARVs are not designed for oral administration and therefore hydrophobicity and lipophilicity are enhanced in order to affect bioavailability and pharmacokinetics. In fact this idea is already being tested by major healthcare companies. In 2017, ViiV Healthcare announced results from their Phase IIb Long-Acting antiretroviral Treatment Enabling trial in which two long-acting ARVs, cabotegravir (CAB) and rilpivirine (RPV) were used in the treatment of HIV infection. Although CAB and RPV are hydrophobic in their native active forms, chemical modifications were employed to further improve their long-acting profiles. When placed in an aqueous nanosuspension with polysorbate 20, polyethylene glycol 3350, and mannitol, CAB demonstrates a long half-life. Similarly, RPV LA is stabilized by poloxamer 338 in aqueous suspensions. The two-drug combination of all-injectable, long-acting CAB plus RPV every 4 weeks or every 8 weeks was as effective as daily three-drug oral therapy at maintaining HIV-1 viral suppression through 96 weeks and was well accepted and tolerated [155]. These drugs were moved to a Phase III trial, named: Antiretroviral Therapy as Long-acting Suppression (ATLAS) study (clinicaltrials.gov identifier: NCT02951052). Both drugs formulations are produced top-down and using wet milling techniques, until drug particles of around 200 nm

are formed. The drug formulations were administered intramuscularly which formed depots in the muscle tissue (injection site), resulting in a sustained release of drug and dosing was performed once a month. CAB and RPV LA are administered at 800 and 1200 mg doses, respectively, as 2 ml gluteal injections. Thus, the high dosing volume requirement and resultant injection site reactions represent significant limitations. These limitations, together with limited formulation access to 'putative' cell and tissue viral reservoirs, open up opportunities for improvements [156, 157].

Our laboratory has sought to overcome these limitations through chemical modifications of native ARVs to generate lipophilic and hydrophobic prodrugs into Long-Acting Slow Effective Release antiretroviral therapy (LASER ART). LASER ART is defined as hydrophobic prodrug crystals stabilized by lipids or surfactants enabling sustained release of therapeutic drug concentrations in plasma and transfer across biological barriers and into anatomical viral reservoirs [158]. The inactive, lipophilic LASER ART prodrug easily crosses these barriers and once in cellular targets it is metabolized into the native active drug by enzymatic or chemical hydrolysis of the 'prodrug moiety. Prodrugs are a major component of LASER ART and enable high drug loading with improved membrane permeability. The advantages of LASER ART are in permitting rapid drug penetration across physiological barriers, slow drug dissolution, poor aqueous solubility, enhanced bioavailability, and reduced systemic toxicities [159-161].

Our laboratory has created ester prodrugs of abacavir (ABC), Lamivudine (3TC), DTG and CAB through myristolyation [154]. After uptake by macrophages

and other cells, intracellular esterases convert inactive prodrug into active drug. The rate of which can be affected by the steric hindrance afforded by the prodrug moiety. As seen with NMDTG, this results in enhancements in macrophage drug uptake, prolonged retention, and drug efficacy for up to 1 month. Pharmacokinetic (PK) tests in Balb/cJ mice showed blood and tissue DTG levels at, or above, the protein-adjusted 90% inhibitory concentration (PA-IC_{90}) for up to 56 days after a single 45 mg/kg intramuscular injection without adverse events [151]. Similarly, intramuscular administration of nanoformulated CAB prodrug at 45 mg/kg CAB equivalents provided plasma drug levels four times above the PA-IC_{90} for 56 days in rhesus macaques [162]. These data demonstrate that thoughtfully engineered prodrugs can improve PK and ARV biodistribution (BD) over-encapsulation of native drug.

1.7 Pharmacokinetic Modeling

The prediction of drug pharmacokinetics after dosing is sometimes accomplished through using mathematical modeling. Models are designed to best represent plasma drug and tissue drug levels over time while attempting to incorporate physiochemical properties and *in vivo* behavior of drug molecules [163-168]. Physiologically based pharmacokinetic (PBPK) models take this a step further by taking into account drug movement through individual anatomical compartments [169]. However, there are several limitations to PBPK modeling in the context of LASER ART that include complex formulation and prodrug design, variant *in vivo* drug biodistribution, metabolism, and transport. Nanoparticle size, shape, and surface characteristics all affect nanoparticle distribution. While some

nanoparticles are designed for uptake by the reticuloendothelial system, others are carried through the lymphatic system [170, 171]. Thus a one-size fits all PBPK model is not realistic. PBPK modeling requires significant clinical and *in vivo* experiment data related to physiologic conditions, biochemical changes, and tissue-specific enzymes that may be seen in some patients. This data may simply not be available. Moreover, variation in the number and type of drug transporters, type and species specificity of cell receptors, drug permeability, surfactant or excipient modulation of the activity enzymes such as cytochrome p450, can result in inaccurate predictions [172-174]. Additionally, the kinetics associated with various routes of administration, differences between animals and humans, and gender specific differences introduce ambiguity into the models [175-177]. Lastly, the PKs of highly hydrophobic drugs with different sizes and shapes of nanoformulations are difficult to predict due to high drug-protein binding and difficulty in mimicking the exact plasma environment [178]. These limitations could be overcome through the development of ARV theranostics.

1.8 Theranostics

Over recent decades, nanotechnology has garnered a considerable amount of interest within the scientific community, with medical research being no exception. Indeed, the ability to reliably and consistently produce materials with dimensions and tolerances of less than 100 nm has proven extremely useful across a diverse multitude of research fields. The impact nanotechnology has had on medicine, both in research laboratories and within the clinical landscape, cannot be understated. Constant innovation in the synthesis and characterization of nanoscale materials has resulted in products with high amounts of utility.

However, until recently, nanotechnology developed for medical purposes has largely been one-dimensional. Development and production of nanomaterials were done for the utilization of a single function; to diagnose and/or provide information on a disease state, or to provide therapy for the treatment of a disease state [179]. These nanoscale diagnostic agents and nanomedicines have proven to be independently useful, with particular success being found in sequential utilization of their single functions. To first make a diagnosis and acquire details on the progression of a disease, and then to administer specific, personalized treatments to abrogate and possibly eliminate said disease based on previously acquired diagnostic information, has proven useful in patient management. But these independent functions, diagnosis and therapy, have required independent nanomaterials. Such a two-part strategy has proven ineffectual for disease states with diverse presentations within the clinic and complicated underlying pathology. Furthermore, the most significant diseases impacting humanity today have complex disease progressions.

The term “theranostics” was coined from the concept of combining both therapeutic and diagnostic nanomaterials into a single platform [180]. Such combination would allow both nanomaterials to be delivered together, allowing for concurrent treatment and monitoring of a disease state. Theranostics is a cornerstone strategy for personalized medicines, allowing for identification of subgroups of patients with specific clinical profiles that are most likely to respond to specific therapies, while also identifying within those same subgroups patients that would have adverse reactions to these same therapies [179].

We developed theranostic nanoparticles for real-time tracking of therapy biodistribution in the treatment of HIV-1. Termed “multi-modal imaging theranostic nanoprobes”, such nanotechnology allowed combined bioimaging, drug

pharmacokinetics, and tissue biodistribution tests in animal models [179]. Individual components include 3 diagnostic components; 1) a paramagnetic contrast agent in cobalt ferrite (CF), 2) an intrinsically doped, gamma-emitting radionucleotide, ^{111}Indium, 3) a fluorescent component in incorporated Europium (Eu3+), and nanoformulated rilpivirine (RPV) as the therapeutic component. These particles were constructed to take advantage of magnetic resonance imaging (MRI) and single photon emission computed tomography/computed tomography (SPECT/CT) imaging modalities in order to correlate imaging data with long term drug pharmacokinetics

1.8.1 Paramagnetic and superparamagnetic contrast agents

MRI has proven to be a powerful and non-invasive diagnostic modality since it's development in the 1970's [181]. MRI utilizes strong magnetic fields, magnetic field gradients, and radio waves for interaction with the protons within a living organism, allowing for generation of internal images. Specifically, MRI generates contrast based on intrinsic differences between different tissue regions such as T1 (spin-lattice) and T2 (spin-spin) relaxation times, and proton density. In some disease states, it is possible to differentiate diseased tissue from healthy tissue based on disease's effect on these intrinsic differences. However, often times the effect of disease pathology on these factors is too limited for any meaningful diagnostic information to be discerned from the resulting images. Because of this, multiple "contrast agents" have been developed that can drastically change the intrinsic relaxation times of specific tissues.

"Paramagnetic" materials can be defined as those that are weakly attracted by an external magnetic field and form internal, induced magnetic fields in the direction of a specific applied magnetic field [182, 183]. Paramagnetic contrast agents include manganese (Mn2+) and gadolinium (Gd) that substantially shorten T1 relaxation of water protons, creating a brightened contrast in T1 MR images. Superparamagnetic contrast agents such iron oxide particles or cobalt ferrite nanoparticles shorten T2 relaxation times of water protons, creating a "darkening" effect on T2 weighted MR images [184]. Additionally, superparamagnetic contrast agents show much more magnetic susceptibility compared that paramagnetic contrast agents, leading to an increase in magnetic sensitivity. In our case, cobalt ferrite particles show exceptional magnetic sensitivity and thus are used in the core of our particles.

1.8.2 Single-photon emission computed tomography

SPECT is a nuclear medicine tomographic technique that uses emitted gamma rays to generate 3D images of radionucleotide location and quantity *in vivo*. The technique requires delivery of a gamma-emitting radioisotope such as Technetium-99m, Iodine-123, or Indium-111 [185]. In the case of nanoparticles, radioisotopes are most often attached to the particles by use of various chelators such as DOTA or NOTA creating a "radioligand" [186]. This allows for visualization of radioisotope concentration and location in the body. SPECT imaging is performed by using a gamma camera to acquire multiple 2D images (also called projections), from multiple angles. A computer is then used to apply a tomographic reconstruction algorithm to the multiple projections, yielding a 3D data set. This

data set may then be manipulated to show thin slices along any chosen axis of the body, similar to those obtained from other tomographic techniques [187]. A CT image is also acquired and acts as a guide for the SPECT rendering. This combined technique is referred to as SPECT/CT.

However, radiolabeling via chelators has several limitations that encouraged us to pursue a different labeling strategy, intrinsic doping of ^{111}indium directly into the cobalt ferrite core particles. *First*, the coordination chemistry of radioisotopes varies significantly. Choosing the right chelator for any specific isotope is challenging, as there are none that can bind multiple radioisotopes [188]. *Second*, external chelators can alter the hydrodynamic size and surface chemistry, which will alter biodistribution and obscure the true pharmacological behavior of the particles [189, 190]. This fact may be enhanced as the radiolabel could become unbound from particle leading to false positive results. Chelator free labeling forgoes the need for chelating moieties and therefore the native pharmacological behavior of the particle is maintained. *Third*, to optimize labeling the number of chelating moieties conjugated to the particle's surface should not impose any limitations. As intrinsic doping places radioisotopes directly into the lattice sites of the particle's metallic core, abundant labeling sites are available which results in high yields with enhanced stability [191]. *Fourth*, with chelator-free labeling, the surface of the particle can be easily modified with targeting ligands, therapeutic agents, or other imaging agents because no surface functional groups are required for the radiolabel [192]. *Lastly*, chelator-free labeling is simple, fast, and effective allowing for radiolabeling with a broader spectrum of isotopes, including ^{72}As and

^{69}Ge, both of which have proven extremely challenging to radiolabel via chelator chemistry [193].

1.8.3 Fluorescence

Fluorescence is the emission of light by a substance that has absorbed light or other electromagnetic radiation. It is a form of luminescence. In most cases, the emitted light has a longer wavelength, and therefore lower energy, than the absorbed radiation. Utilization of such a property has proven useful in biological sciences, as application of fluorescent materials to a vehicle allows for non-destructive tracking or analysis through different biological pathways. This can be performed at specific emission frequencies in which there is no background from excitation light, as very few biological components are naturally fluorescent. Such "fluorescent labeling" can be done via a very large variety of different fluorophores such as dyes and fluorescent proteins, each with a unique excitation and emission wavelength, molecular weight, and quantum yield [194]. Additionally, specific elements exhibit intrinsic fluorescence. Rare-earth doped phosphors such as Terbium, Cerium, Lanthanum, and Europium form the basis for fluorescent lighting [195]. Incorporation of rare earth element Eu3+ into our nanoparticle vehicle proved particularly useful, exhibiting fluorescence and emission wavelengths at 410 nm and 660 nm, respectively. Europium doping within the spinel ferrite structure of our theranostic nanoparticles allowed for subcellular tracking using both in vitro and ex vivo confocal microscopy, as described in chapter 2.

1.8.4 Nanoformulated ARVs

The final component of our theranostic nanoparticles was that of nanoformulated ARV drug, specifically the non-nucleoside reverse transcriptase inhibitor, rilpivirine. Considerable innovation has occurred in the production of long-acting ART regimens in efforts to reduce secondary toxicities, improved drug adherence, and prevent new infections [196]. Ultimately, such goals center on drastically increasing the half-life of ARV drugs by improving upon their hydrophobicity. Formation of cell and tissue penetrate nanocrystals that are protected by biodegradable polymers allow the establishment of drug depots within monocyte-macrophages, prolonging drug half-life. [196, 197] However, a major drawback of developing long-acting ARV formulations is that biodistribution and pharmacokinetic studies, often taking weeks to months, are tedious and burdensome. Incorporation of long acting ARV drug into theranostic nanoparticles, in conjunction with other components, allows a much more rapid screening of tissue biodistribution and pharmacokinetics, subsequently resulting in much more timely pharmacodynamics (PD) improvements and drug screening.

CHAPTER 2
Synthesis, characterization, and *in vitro* testing of multi-modal theranostic nanoformulations

2.1 Introduction

The development of effective antiretroviral therapy (ART) for human immunodeficiency virus type one (HIV-1) infection has dramatically reduced disease morbidities and mortality [198, 199]. ART's success, over the past several decades, is substantive as evidenced by the treatment's ability to efficiently reduce circulating plasma HIV-1 loads to undetectable levels. In so doing ART protects CD4+ T cells and reduces comorbid disease [200, 201]. However, current treatment limitations include drug pharmacokinetics (PK) and biodistribution profiles, viral mutations and drug toxicities [202, 203] . All affect optimal therapeutic efficacy [204]. Additionally, short antiretroviral (ARV) drug half-lives necessitate daily dosing and strict regimen adherence [205]. Reduced ARV access to virus target tissues can also affect the maintenance of drug levels at action sites and the ability to contain CD4+T cell infection [206]. Innate inflammatory and adaptive immune responses tied to HIV-1 infection continue despite therapeutic drug regimens, leading to diabetes, osteoporosis, cardiovascular diseases and neurocognitive disorders [207-212]. Therefore, a major unmet need in the treatment of human immunodeficiency virus type one (HIV-1) infection rests in long-term adherence to antiretroviral therapy (ART). If brought into clinical practice, long-acting ART regimens would substantively improve drug adherence, reduce secondary toxicities and prevent new infections. These could ultimately facilitate the realization of an AIDS-free world [196, 213-217].

Substantial efforts to overcome these limitations has led to the development of longer acting nanoformulated ART and recently to the chemical synthesis of lipophilic prodrug nanocrystals coined long acting slow effective release (LASER) ART which has further extended drug ARV half-lives and potencies [151, 218, 219]. LASER ART rests on four pillars; creation hydrophobic prodrug nanocrystals, the enhanced drug lipophilicity

associated with improved cell membrane drug penetration, slow drug release and hydrolysis, and facilitated viral reservoir drug penetrance. These transformative technologies have created ARVs that best penetrate viral reservoirs and increase the drug's apparent half-life creating medicines that maximally restrict viral growth [154] .

In order to realize the potential of long acting tissue viral reservoir penetrating ARVs, the drugs' pharmacokinetic (PK) and pharmacodynamic (PD) profiles must be optimized to minimize on and off-target effects. However, a significant obstacle remains in the ability to rapidly screen drug formulation tissue biodistribution and pharmacokinetics (PKs) in order to realize substantive PD improvements. This is of particular importance as, while the half-lives of each of the few existing long-acting drugs are measured in weeks or even months, drug tissue distribution is limited [216, 220-223]. Moreover, while mathematical descriptions of long-acting nanoformulated drug distribution have been developed, these cannot reflect the diversity of chemical alterations and physical characteristics now required for LASER ART nanoformulations [224] **.** To this end multimodal theranostic ARVs were created to serve as effective descriptor for drug biodistribution.

To overcome these technical and biologic challenges, multimodal decorated nanoparticles were produced with hydrophobic ARVs and bioimaging agents encased in a single nanoformulation. All were placed into one "multimodal imaging theranostic nanoparticle" using core-shell construction methods [225]. The surface of the particle was coated with lipids decorated with targeting moieties, while the drug, along with SPECT and MRI image contrast agents were incorporated into a polymeric core. Specifically, ^{111}indium and europium (Eu3+)- doped cobalt ferrite (CF, ^{111}InEuCF) crystals and hydrophobic drug rilpivirine (RPV) were packaged in a polycaprolactone (PCL) core. Intrinsic doping of the radioisotope, ^{111}indium into the core of the particle, imparted SPECT capabilities while also providing a highly stable association between particle and

radioisotope. A lipid layer coated the particle's "shell". L-α-phosphatidylcholine (PC), 1,2-distearoyl-phosphatidylethanolamine-methyl-polyethyleneglycol conjugate-2000 (DSPE-PEG2000) and 1,2-dioleoyl-sn-glycero-3-phosphoethanolamine (DOPE) lipids enhanced particle biocompatibility and lipophilicity, facilitating macrophage targeting [226] . Nanoparticles were produced with consistent size and stability, and were readily phagocytosed and retained by macrophages in culture, resulting in long-acting slow effective drug release (LASER) ART profiles [219, 227] . This was reflected by the multimodal theranostic particle's ability to effectively inhibit HIV viral growth *in vitro* to the same degree as nanoformulated RPV. Together these properties enable depot formation for viral reservoir targeting and bioimaging [227] .

2.2 Materials and Methods

2.2.1 Reagents

Iron(III) acetylacetonate ($Fe(acac)_3$), cobalt(II) acetylacetonate ($Co(acac)_2$), europium(III) nitrate hydrate ($Eu(NO_3)_3 \bullet 5H_2O$, oleic acid, oleylamine, poly(vinyl alcohol) (MW 30,000-70,000, 87-90% hydrolyzed), L-α-phosphatidylcholine (PC) (from egg yolk), 3-(4,5-dimethylthiazol-2-yl)-2,5-diphenyltetrazolium bromide (MTT), CF®633 succinimidyl ester (CF®633), poloxamer 407 (P407), low gelling temperature agarose, SIGMA*FAST*™ 3,3'-diaminobenzidine and propidium iodide were obtained from Sigma Aldrich, St. Louis, MO, USA. Polycaprolactone (PCL) (MW 43,000-50,000) was obtained from Polysciences, Inc. Warrington, PA, USA. 1,20-distearoyl-phosphatidylethanolaminemethyl-polyethyl-eneglycol conjugate 2000 ($DSPE\text{-}PEG_{2000}$) and 1,2-dioleoyl-sn-glycero-3-phosphoethanolamine (DOPE) were obtained from Corden Pharma International, Plankstadt, Germany. Rilpivirine (RPV) was acquired from Hangzhou Bingo Chemical Co., Ltd. Hangzhou, ZJ, China. ^{111}Indium chloride ($^{111}InCl_3$) was purchased from Cardinal

Health, Dublin, OH, USA. ^{177}Lutetium chloride ($^{177}LuCl_3$) was obtained from Oak Ridge National Laboratory, Oak Ridge, TN, USA. Pluronic® F 108 Pastille (P338) was bought from BASF, Florham Park, NJ, USA. Heat-inactivated pooled human serum was purchased from Innovative Biologics (Herndon, VA). Dulbecco's Modified Eagle Medium (DMEM) was purchased from Corning Life Sciences (Tewksbury, MA). Monoclonal mouse HIV-1 p24 (Clone Kal-1) and Dako EnVision+ detection system HRP labeled polymer anti-mouse antibodies were purchased from Agilent Technologies, Santa Clara, CA, USA. *In Situ* apoptosis detection kit (ab206386) was purchased from Abcam (Cambridge, UK) and assay was done per manufacturer's instructions. The following primary antibodies were obtained from Santa Cruz Biotechnology, Inc. (Dallas, TX, USA): Rab5 (D-11) (sc-46692), Rab7 (H-50) (sc-10767), Rab11 (C-19) (sc-6565), Rab14 (sc-98610) (H-55), and Lamp1 (sc-19992) (1D4B). The following Alexa Flour™ secondary antibodies were purchased from Thermo Fischer Scientific (Waltham, MA, USA): 594 goat anti-rabbit (A11037), 594 goat anti-mouse (A11005), 488 chicken anti-mouse (A21200), and 488 goat anti-rabbit (A11008). Optima-grade solvents and water were purchased from Thermo Fischer Scientific. Bovine Serum Albumin (BSA) purchased from Fischer Scientific.

2.2.2 Synthesis of Rilpivirine (RPV) freebase

RPV freebase was prepared by using as received RPV-HCL. To a 500 mL capacity beaker, 2g of RPV-HCL was added to a 250 ml mixture of ethyl acetate and HPLC grade water (4:1 v/v) stirred on ice. After 30 min, sodium hydroxide (1M) was carefully added until RPV was completely dissolved into the organic layer. Finally, using a separation funnel, organic and aqueous layers were separated. The organic layer was washed with

50 mL brine, collected and dried with sodium sulfate. Solvent evaporation yielded RPV freebase, which was characterized by ^{1}H NMR and HPLC.

2.2.3 Preparation of Nanoformulated RPV (NRPV) and CF®633-NRPV

Nanoformulated RPV (NRPV) and CF®633-labeled NRPV (CF®633-NRPV) were prepared by high-pressure homogenization (Avestin EmulsiFlex-C3; Avestin Inc., Ottawa, ON, Canada). In preparing NRPV, P338 (0.5% w/v) was fully dissolved in endotoxin-free water. For NRPV-CF®633 preparations, a 1:5 (w/w%) mixture of CF®633 and P407 (total 0.5% w/v) were dissolved in endotoxin-free water. Free-base RPV was then added (1.0% w/v), and the mixtures were bath-sonicated for 15 min and mixed overnight at high speed. The solutions were then homogenized at 20,000 psi until the desired particle size was reached (~260 nm). Suspensions were stored at 4°C and vials were wrapped in foil for protection from light.

2.2.4 Preparation of Radiolabeled ^{111}InEuCF-RPV Theranostic Nanoparticles

Production of chelate free, non-leachable and highly stable radiolabeled ^{111}InEuCF nanocrystals was accomplished by intrinsically co-doping the radionuclide, ^{111}In, along with europium into a core cobalt ferrite lattice structure. In a typical synthesis, Fe (acac)$_3$ (706 mg, 2 mmol), Co(acac)$_2$ (257 mg, 1 mmol), Eu(NO$_3$)$_3$_5H$_2$O (100 mg, 0.29 mmol), 1,2-hexadecanediol (2.584 g, 10 mmol), 5 ml of oleic acid, 5 ml of oleamine, and 30 ml of benzyl ether were mixed and sonicated for 2 min using a probe type sonicator (Cole-Parmer, Vernon Hills, IL, USA). Separately, ~555 MBq (~15 mCi) of $^{111}InCl_3$ was mixed with 750 μL of benzyl alcohol, vortexed and stirred for 30 min at room temperature. The two mixtures were combined and slowly transferred into a Teflon container for hydrothermal synthesis. The obtained mixtures of metal precursors, surfactants,

protective ligands and reducing agents were added to a Teflon container and sealed in a high-quality stainless steel autoclave reactor. This reactor was placed in a preheated vacuum oven for 90 min at 260°C then cooled to room temperature. ^{111}InEuCF nanocrystals were purified by washing with ethanol and collected with a magnet. Radioactivity of ^{111}InEuCF nanocrystals was quantitated by gamma counting (CRC®-25R dose calibrator, Capintec, Inc, Florham Park, NJ, USA). The encapsulations of ^{111}InEuCF nanocrystals were re-suspended in chloroform or hexane for the next formulation step. ^{111}InEuCF and RPV in PCL and further coating with a lipid shell was accomplished using a modified solvent evaporation process [225, 228]. Specifically, PCL (400 mg), RPV (30 mg) and ^{111}InEuCF (20 mg) were dissolved in DCM, methanol and chloroform (oil phase), respectively. Fresh lipid mixtures were prepared by dissolution of PC (50 mg), mPEG$_{2000}$-DSPE (25 mg) and DOPE (25 mg) in 5 mL of chloroform by bath sonication. The ^{111}InEuCF-RPV primary emulsion was prepared by mixing EuCF, PCL and RPV solutions with stirring for 6-8 h at 140 × g at room temperature. The secondary emulsion and shell layers for core nanoparticles were prepared by making a thin film of lipids (PC, PEG$_{2000}$-DSPE and DOPE) in a round bottom flask through rotary evaporation (Büchi Rotavapor R-II, New Castle, DE, USA) of chloroform followed by overnight vacuum-drying. The primary emulsion of ^{111}InEuCF-RPV was then transferred into 30 mL of freshly prepared 1% (w/v) PVA and mixed by probe sonication (Cole-Parmer, Vernon Hills, IL, USA) at 20% amplitude for 10 min in an ice bath. The PVA served as a surfactant in this emulsification step. The core nanoparticles were then transferred into the flask containing the lipid film. The flask was steadily rotated with the core nanoparticles in a bath sonicator followed by probe sonication at 20% amplitude for 10 min in an ice bath. Evaporation of DCM was carried out under pressure at 35°C followed by overnight stirring. The nanoparticles were purified by centrifugation of the suspension at 55 × g for 10 min, followed by centrifugation of the supernatant at 35,131 × g for 30 min at 10°C (Sorvall, Lynx-4000 super speed

centrifuge, Thermo Fisher Scientific, Waltham, MA, USA). The pellet was washed twice with PBS, resuspended in PBS and stored at 4°C. Non-radiolabeled InEuCF probes were synthesized by similar methods except that stable $^{113}InCl_3$ was the source of indium.

2.2.5 Production of Ultra-Small Intrinsically Radiolabeled ^{177}LuEuCF Nanoparticles

Particle size is known to play a key role in biodistribution, however the effect is still not completely understood [229, 230]. To test the effect of construct size on drug biodistribution ultra-small (~5 nm) ^{177}lutetium-radiolabeled EuCF nanocrystals (^{177}LuEuCF) were prepared. Lipid coated ^{177}LuEuCF nanocrystals were synthesized with a reaction time of 45 min. ^{177}LuEuCF nanocrystals encapsulations were accomplished using a spectrum of lipid film composition ratios. Ultra-small ^{177}LuEuCF nanocrystals were coated with lipid by dehydration processes. The lipid film was prepared from solutions of PC (25 mg) and DSPE-PEG_{2000} (12.5 mg) in chloroform followed by rotary evaporation. ^{177}LuEuCF nanocrystals were dispersed in chloroform by sonication for 30 min and then transferred into 2% Tween 80 (3 mL) solution to make oil in water (o/w) emulsion. This emulsion was allowed to stir for one hour at room temperature to ensure complete removal of chloroform, then transferred into the round bottom flask containing the lipid film and stirred for an additional five hours. Finally, lipid coated ultra-small ^{177}LuEuCF nanocrystals were purified by centrifugation at 35,136-x g (18,000 rpm) for 30 min and re-suspended in PBS.

2.2.6 Particle Characterizations

The structural and crystallinity characteristics of particles were examined by powder X-ray diffraction (XRD), hydrodynamic size distribution, polydispersity index (PDI) and transmission electron microscopy (TEM) [196]. Powder X-ray diffraction (XRD) analysis was carried out in the 2θ range of 2–70° using a PANalytical Empyrean

diffractometer (PANalytical, Inc., Westborough, MA, USA) with Cu-Kα radiation (1.5418 Å) at 40 kV and 45 mA. A mask of 20 mm and divergence slit of 1/32° were used on the incident beam path. A thin layer of the powdered nanoparticle was placed on a zero-background silicon plate and continuously spun at a rate of 22.5°/s. The solid state PIXcel3D detector (PANalytical, Inc.) was scanned at a rate of 0.053°/s. The PIXcel3D was equipped with a beam monochromator to improve the signal-to-noise ratio. Stability of the EuCF-DTG nanoparticle suspension was assessed over three weeks by measuring hydrodynamic diameter and nanoparticle size distribution in saline on a Malvern Zetasizer Nano-Series instrument (Malvern Instruments Ltd., Malvern, UK) at 4 °C. Nanoparticle morphology and structure were analyzed by transmission electron microscopy (TEM). Nanoparticle suspensions were dried on a copper grid at room temperature and bright field images were taken with exposure times of 2 s using the Tecnai G2 Spirit TWIN electron microscope (FEI, Houston, TX, USA) operating at 80 kV. Images were acquired with an AMT digital imaging system. RPV content of EuCF-RPV was determined by reversed-phase ultra-performance liquid chromatography (UPLC) using a Waters ACQUITY UPLC H-Class System with TUV detector and Empower 3 software (Waters, Milford, MA, USA) as described previously [179]. Metal quantitation was performed by inductively coupled plasma mass spectrometry (ICP-MS) at the University of Nebraska-Lincoln's Spectroscopy and Biophysics Core Facility, using an Agilent 7500cx ICP-MS (Santa Clara, CA, USA) coupled with a 96-well plate autosampler Model SC/DX4 from Elemental Scientific, Inc. (Omaha, NE, USA), operating in GasMix mode (3.5 mL H2 and 1.5 mL He per min). Other conditions were: plasma power, 1500 W, carrier Gas flow, 1 L per min., Makeup Gas glow, 0.15 L per min., sample depth, 8 mm. Concentrations were calculated against an external calibration curve and 50 µg/L of Ga was used as internal standard (IS) throughout (71Ga isotope).

2.2.7 Radiolabeled Particle Stability

The *in vitro* stability of ^{111}InEuCF-PCL particles was tested in PBS and rat plasma solutions. ^{111}InEuCF-PCL particles, 1.48 MBq (40 µCi), were incubated in 1.5 mL of phosphate buffered saline (PBS) or rat plasma at 4°C and 37°C for 3 days. At 0, 24, 48 and 72 hours, the samples were centrifuged at 21,255-x g (14,000 rpm) for 30 min at 10°C and supernatants were collected. The radioactivity of the supernatant and pellet (particles) was measured by gamma counter to determine the percent stability. The percent stability was calculated using the equation (Radiolabeling stability (%) = radioactivity in pellet / total radioactivity X 100).

2.2.8 Isolation and Culture of Monocyte-Derived-Macrophages (MDM)

Human peripheral blood monocytes were obtained by leukapheresis from hepatitis B and HIV-1/2 seronegative donors, and were purified by counter-current centrifugal elutriation [196]. Cells were cultured in Dulbecco's modified Eagle's medium (DMEM; Invitrogen, Grand Island, NY, USA) with 10% heat-inactivated pooled human serum (Innovative Biologics, Herndon, MA, USA), 1000 U/mL macrophage colony stimulating factor, 1% glutamine, 50 µg/mL gentamicin, and 10 µg/mL ciprofloxacin for 7 days to promote monocyte macrophage differentiation [231].

2.2.9 Properties of Particles in vitro: Cell Vitality, Uptake and Retention in MDMs

Cell vitality evaluation of native RPV, EuCF-RPV, ^{111}InEuCF-RPV and NRPV was performed using the 3-(4,5-dimethylthiazol-2-yl)-2,5 diphenyltetrazolium bromide (MTT) assay[232]. In brief, 10^5 human monocytes per well were seeded on a flat-bottomed 96-well polystyrene coated plate and incubated for seven days at 37°C in a 5% CO_2 incubator

for differentiation into MDM as stated in section 2.2.8. Serial dilutions of EuCF-RPV, ^{111}InEuCF-RPV and NRPV particles (0.2-200 μM based on RPV concentration or 1.987X10^{-3} to 8.14 MBq) in media were added to the cells in triplicate. Native RPV was dissolved in dimethyl sulfoxide (DMSO) and diluted in media (0.1% v/v) for MDM treatment control. After treatment, the media was removed and 100 μL of MTT solution (0.5 mg/mL) was added to each well. Plates were incubated at 37°C for 45 minutes. The MTT solution was removed after incubation and 100 μL of sterile DMSO was added to each well to dissolve formazan crystals. The plates were read immediately in a SpectraMax® M3 Multi-Mode Microplate Reader (Molecular Devices, LLC, Sunnyvale, CA, USA) at absorbance of 490 nm. Wells with DMSO but without cells were used as blanks. Untreated MDM and cells treated with EuCF-RPV and NRPV for 8 hours were evaluated by the MTT assay to assess cell vitality.

MDM uptake and retention of EuCF-RPV and NPRV particles were determined according to published reports with noted modifications [179, 233]. MDM were plated in 12 well plates at a density of 1.5 × 10^6 cells/well with half media exchanges every other day. After seven days, 6.25 μM, 12.5 μM and 25 μM concentrations of EuCF-RPV and NPRV particles were added to the cells and incubated for 2, 4, 8 and 12 hours to evaluate particle uptake. Cell particle retention was determined by treating MDM with 25 μM EuCF-RPV or NRPV for 8 hours followed by washing the cells and adding fresh medium without particles. Cell samples were collected on days 1, 3, 5, 7, 11, 12 and 15 following treatment. At each time point, the media was removed, cells were washed three times with PBS then counted and harvested following centrifugation at 21,255 x g (14,000 rpm) for 10 min. Cell pellets were stored at -80°C for metal analysis. The cell pellet was digested with fresh diluted nitric acid. Iron and cobalt concentrations were determined by ICP-MS and reported as iron or cobalt concentration per million cells as previously described [179]. For RPV analysis 100 μL of methanol was added to the cell pellet followed by sonication for 2

min. The mixture was then centrifuged at 21,255-x g (14,000 rpm) for 10 min and the supernatant was collected. RPV concentration in the supernatant was determined by UPLC with UV/Vis absorption as previously described [234].

2.2.10 Transmission Electron and Atomic Force Microscopy (TEM and AFM)

The uptake of EuCF-RPV and NPRV particles in MDMs along with associated cell surface topological changes were visualized by transmission electron microscopy (TEM) and atomic force microscopy (AFM). For TEM analysis MDMs (1.5 x 106 cells/mL) were incubated for 8 h with EuCF-RPV and NRPV particles (RPV content: 25 μM). For TEM, MDM were fixed in a solution of 2% glutaraldehyde and 2% paraformaldehyde in 0.1 M Sorenson's phosphate buffer (pH 6.2) for 24 h at 4°C. Samples were washed three times with PBS. During processing samples were postfixed in a 1% aqueous solution of osmium tetroxide for 30 minutes. Subsequently, samples were dehydrated in a graded ethanol and propylene oxide used as a transition solvent between the ethanol and araldite resin. Samples were allowed to sit overnight in a 50:50 propylene oxide:resin solution until all the propylene oxide had evaporated then they were incubated in fresh resin for 2 h at room temperature before embedding. Polymerization took place at 65°C for 24 h. The staining procedure was 10 minutes in 2% (w/v) uranyl acetate, washed 3 times in distilled water, 10 minutes in Reynolds Lead Citrate, and washed 3 times in distilled water. Thin sections (100nm) made with Leica UC6 Ultracut ultramicrotome were placed on 200 mesh copper grids, and examined on the Tecnai G2 Spirit TWIN (FEI) operating at 80kV. Images were acquired digitally with an AMT imaging system.

For AFM Cells were cultured on glass coverslips in 12 well plates at a density of 1.5 X 10^6 cells/ well and incubated for seven days at 37°C and 5% CO_2 to differentiate into MDM as described previously. MDM were treated with EuCF-RPV and NRPV particles

(25 μM based on RPV) for 8 hours. After particle incubation, cells were fixed with ice-cold 4% paraformaldehyde (PFA) in PBS at room temperature for 30 min. Coverslips with fixed cells were removed from wells and mounted on a slide for AFM analysis. Images were acquired in air using an MFP-3D^{TM} system (Asylum Research, Santa Barbara, CA, USA) operating in tapping mode. AFM probes MSNL-F with a nominal spring constant ~0.6 N/m were used for imaging. Image processing was performed using Femtoscan software (Advanced Technologies Center, Moscow, Russia).

2.2.11 Immunocytochemistry (ICC) and Flow Cytometry Assessments

Subcellular localization of particles taken up by MDM was accomplished via immunocytochemistry using fluorescent secondary antibodies as previously described with some modifications [235, 236]. Briefly, after EuCF-RPV and NRPV-CF$^{®}$633 particle treatment of MDM, cells were washed with PBS and fixed with ice cold 4% PFA at room temperature for 30 min and rinsed three times with PBS. MDM were then treated with 0.5% v/v Triton-X-100 for 15 min to permeabilize the cells and again washed with PBS. A mixture of 5 % w/v bovine serum albumin (BSA) in PBS and 0.1% v/v Triton-X-100 was used as a blocking solution for 1 hour and 50 mM NH_4Cl was used as quenching solution for 15 min and washed once with 0.1% Triton-X-100 in PBS. MDM were next treated with primary antibodies against either lysosomal-associated membrane protein 1 (LAMP-1; Novus Biologicals, Littleton, CO, USA) for lysosome identification, Rab 5 and Rab 7 for late endosomes, or Rab 11 and Rab 14 (Santa Cruz Biotechnology, Dallas, TX, USA) for recycling endosomes. Primary antibodies were diluted 1:25 (v/v) antibody:blocking solution and incubated overnight with shaking at 4°C as previously described [179]. MDM were then treated with secondary antibody in blocking solution (1:50) (AlexaFluor- 488 and 594 for NRPV-CF$^{®}$633 and EuCF-RPV, respectively; Thermo-Fischer Scientific,

Waltham, MA, USA) for 2 hours at room temperature. MDM nuclei were stained using ProLong Gold AntiFade reagent with DAPI (4′,6-diamidino-2-phenylindole; Thermo-Fischer Scientific, Waltham, MA, USA). Cells were imaged using a 63 X oil objective on a LSM 710 confocal microscope (Carl Zeiss Microimaging, Inc., Dublin, CA, USA). Zeiss LSM 710 Image browser AIM software version 4.2 was used to determine the number of pixels and the mean intensity of each channel.

NRPV uptake at select drug concentrations was analyzed and validated by flow cytometry [237, 238]. Briefly, 5 x 10^6 MDM were cultured in suspension in 50 mL Teflon flasks containing 20 mL of cell culture media. After 7 days of culture, cells were treated with NRPV-CF®633 at 25 μM and 50 μM RPV or vehicle control for 8 hours. After 8 hours, cells were centrifuged 976 x g (3,000 rpm) for 10 minutes at 4°C following which treatment media was removed. Cells were re-suspended in cold PBS and centrifuged again at the same conditions. After washing, cells were again re-suspended in PBS at a concentration of 1.0 x10^6 cells/mL. Before flow analysis, cells were incubated with the viability dye, propidium iodide (PI), for 30 minutes. Analysis was completed with a BD LSR II Flow Cytometer (BD Biosciences, Franklin Lakes, NJ, USA). Cells were gated according to viability and only live cells were selected for analysis of NRPV-CF®633 uptake. Unlabeled cells were used to calculate the background fluorescence and MDM without any treatment served as a negative control in every measurement. The percentage of cells that internalized NRPV-CF®633 was determined using BD FACSDiva 8.0.1 software (BD biosciences, Franklin Lakes, NJ USA).

2.2.12 Particle T_2 Relaxivity Measurements

T_2 relaxivity measurements of EuCF-RPV particles were determined in two sets of samples over a concentration range of 3.58 to 35.81 μM iron. EuCF-RPV particle

suspensions were prepared in PBS. A 1.5% (w/v) agar gel was prepared by heating agar powder dissolved in PBS at 70°C for 30 min. In 250 µL eppendorf tubes, 100 µL of EuCF-RPV particle suspensions were mixed with 100 µL of the 1.5% (w/v) agar solution and solidify in an ice bath. The second set of samples were prepared with EuCF-RPV particle loaded MDM. In order to measure the T_2 relaxivity in MDM, cells were seeded onto 100 mm culture plates at a concentration of 1 x 10^6 cells/mL. MDM were incubated with EuCF-RPV particles in media (5 µg/mL based on iron) for 8 hours. After treatment, the media was removed and cells were washed three times with PBS. Cells were collected by centrifugation at 976 x g (3,000 RPM) for 10 min at 4°C and re-suspended at various cell concentrations in PBS containing 1.5% (w/v) agar in 250 µL eppendorf tubes. T_2 relaxtivity was measured using a 7T/16 cm Bruker PharmaScan scanner (Bruker; Ettlingen, Germany) with set parameters described previously [196]. Relaxivity in MDM was used to generate a standard curve correlating cellular iron content to T_2 relaxation time to be used for *in vivo* quantitation of tissue iron concentration by MRI.

2.2.13 Measurements of Particle Antiretroviral Activities

Antiretroviral activities of EuCF-RPV, NRPV and native RPV were evaluated by measures of reverse transcriptase (RT) activity and HIV-1p24 staining according to previously described protocols with modifications [153]. In brief, MDM were treated with 6.25 µM, 12.5 µM, or 25 µM (RPV content) native RPV, NRPV or EuCF-RPV particles for 8 hours. MDM were then cultured in fresh medium without particles. At days 1 and 5 post-treatment, MDM were challenged with HIV-1_{ADA} for 16 hours at a multiplicity of infection (MOI) of 0.1 infectious virions per cell. MDM were cultivated for 10 days after infection. Culture supernatants were collected and analyzed for progeny virion production by RT activity assay [239]. At the same time, cells were washed with PBS and fixed in 4% PFA

for 15 min for HIV-p24 staining [151]. Images were analyzed using a Nikon TE300 microscope with a 20X magnification objective.

2.3 Results

2.3.1 Synthesis and Physical Characterizations of Multimodal Theranostic Nanoparticles

EuCF particles were prepared by solvothermal techniques using cobalt acetylacetonate; iron (III), acetylacetonate, and europium (III) nitrate hydrate in the presence of oleic acid and oleylamine. To create SPECT/CT capable nanoparticles with a highly stable radiolabel, radioactive indium chloride ($^{111}InCl_3$) or lutetium chloride ($^{177}LuCl_3$) was slowly added into the reaction mixture. Benzyl alcohol served as solvent and protective ligand, while 1,2-hexadecanediol was used as a reducing agent [240]. A schematic of this synthesis is shown in **Figure 2.1A.** The stability of the radiolabeled ^{111}InEuCF-PCL particles was assessed in PBS and rat plasma at 4°C and 37°C and was found to be >97.4 ± 0.26% after 24 hours. Plasma stability studies confirmed that the radioactive isotope remained particle bound over 3 days (**Table 2.1**). For physical characterizations, non-radioactive InEuCF nanoparticles were used. Preparation of NRPV was accomplished using high-pressure

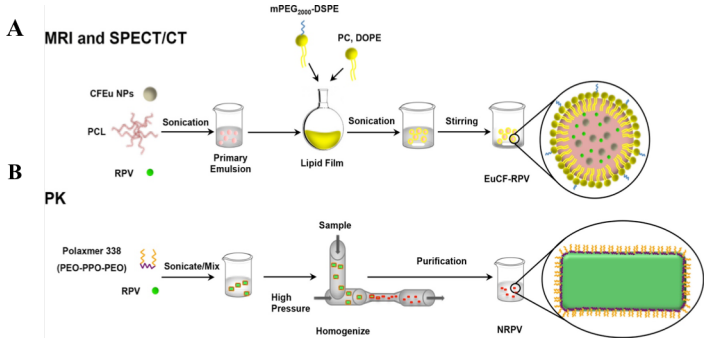

Figure 2.1 Synthesis of Multimodal Theranostic Nanoparticles and NRPV. A schematic illustration of the design of multimodal EuCF-RPV core-shell nanoparticles as well as a schematic illustrating the production of NRPV is presented in **(A)** and **(B)**, respectively.

Table 2.1 Radiolabeling stability in vitro.

Time points (h)	^{111}In labeling efficiency (%)			
	4°C		37°C	
	PBS	Plasma	PBS	Plasma
0	100 ± 0.00	100 ± 0.00	100 ± 0.00	100 ± 0.00
24	97.6 ± 0.09	89.3 ± 0.64	97.4 ± 0.26	89.2 ± 0.63
48	97.2 ± 0.06	89.6 ± 0.77	97.7 ± 0.19	89.5 ± 0.97
72	97.1 ± 0.94	87.6 ± 1.27	97.3 ± 0.46	82.5 ± 0.60

homogenization of RPV in the presence of polaxamer 338 [204, 241]. A schematic of this process is shown in **Figure 2.1B.** RPV drug loading into the EuCF-RPV was determined to be ~ 5.5% (w/w). The hydrodynamic size of monodispersed NRPV, EuCF-RPV, and ^{111}InEuCF is shown in **Figure 2.2A.** RPV nanocrystals had an average hydrodynamic size of 260 nm, which was similar to that of the EuCF-RPV and ^{111}InEuCF-RPV particles that measured 220 nm. As expected, intrinsic doping of ^{111}Indium had no effect on particle hydrodynamic size. Additionally, EuCF-RPV and ^{111}InEuCF-RPV particle sizes remained constant in a variety of different media. As shown in **Figure 2.2D,** The PDI of all particles was ~0.2. The size and PDI of NRPV were stable in water for four weeks at both 4ºC and 25ºC. Additionally, the size and PDI of ^{111}InEuCF-RPV and EuCF-RPV particles were evaluated daily over a week with incubation in a variety of solutions including, distilled water, 150 mM NaCl in water, distilled water adjusted to a pH of 3, 5, 7, 9 and 11**,** PBS containing 2% BSA, and MDM cell media. Size and PDI of both particles in all solutions were unchanged after a week indicating that these particles are stable and thus suitable for further studies.

In addition, the crystalline properties of nanoformulations could also influence particle stability and the *in vivo* drug pharmacokinetics and biodistribution parameters [151, 242]. Undesirable *in vivo* burst release PK patterns and ultimately rapid clearance from tissues and plasma depend on variables that include type of drug, surfactants, process and duration of making nanoformulations [243]. These changes vary depending

on the type of drug, surfactant used, pressure and time to make the nanoformulations. Therefore, before and after particle size reduction, XRD analysis was conducted to assess whether the initial crystalline state was preserved. **Figure 2.2B** shows the results of each of the XRD patterns of RPV, NRPV, CF, EuCF and InEuCF. The powder X-ray diffraction study of NRPV showed significant shifts in the main peaks, compared with coarse RPV. RPV showed characteristic diffraction peaks at 12.42°, 13.93°, 17.57°, 20.0°, 25.68°, 27.87° and 32.70° at 2θ positions. Whereas NRPV showed characteristic diffraction peaks at 31.80°, 45.5° and 56.62° at 2θ positions. This shift from lower 2θ angles to higher 2θ

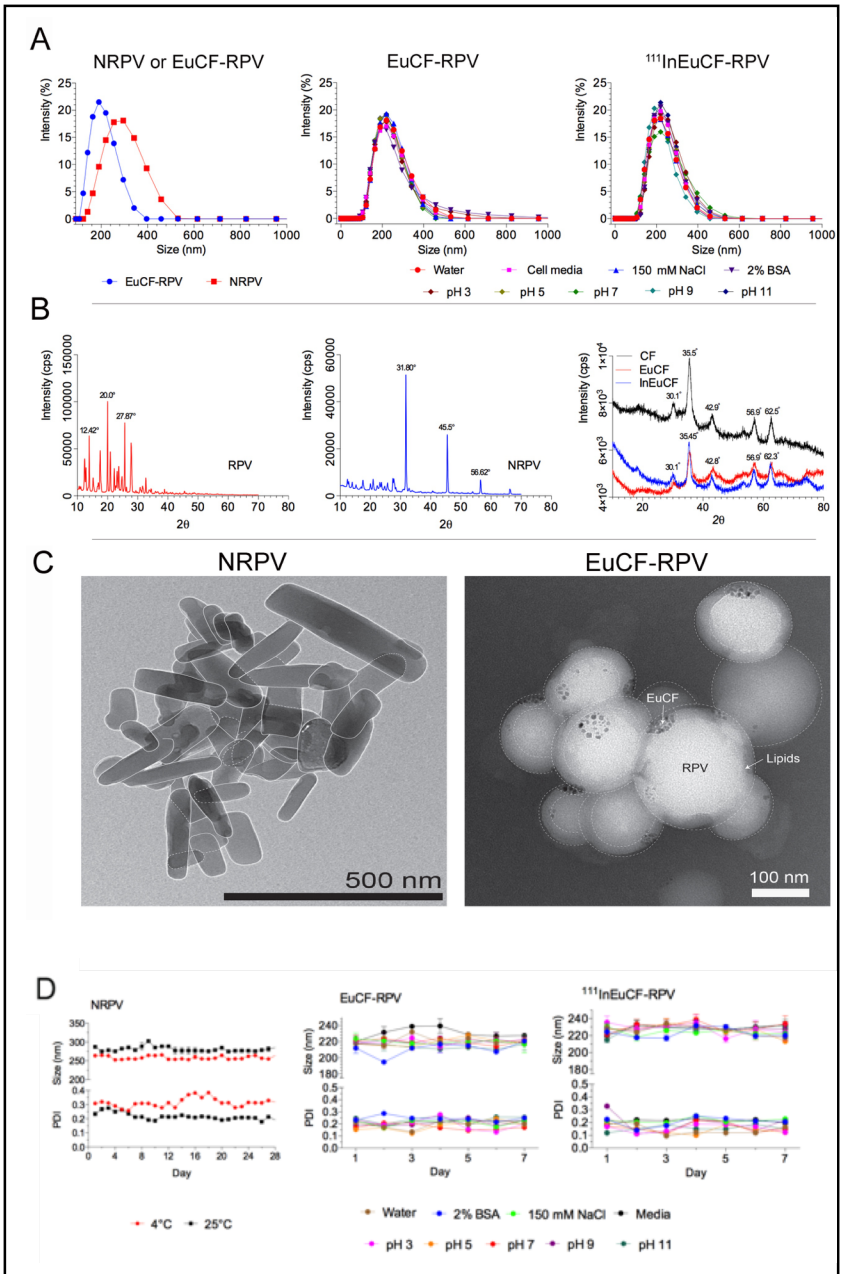

Figure 2.2 Characterization of particles. (A) Hydrodynamic size distribution of NRPV, EuCF-RPV and 111EuCF-RPV particles. **(B)** XRD pattern of RPV, NRPV, CF, EuCF and InEuCF particles. **(C)** TEM image of NRPV and EuCF-RPV. **(D)** Stability of particles' hydrodynamic size distribution measurements of NRPV in PBS (average particle sizes of ~260 nm), and 111InEuCF-RPV and EuCF-RPV in various conditions

angles can be attributed to the formation of a different molecular structure from the more amorphous parent RPV. From these values, it is clear that NPRV is crystalline in nature after high-pressure homogenization. In the XRD pattern of CF, EuCF and InEuCF shown values that closely matched that of our own previously published reports reflecting the inverse spinel to the spinel ferrite structure [196]. We observed, from the XRD results, that intrinsically doping indium or europium into the cobalt ferrite lattice produced no significant structural changes to the crystalline lattice of atomic planes.

TEM images of NRPV and EuCF-RPV particles are presented in **Figure 2.2C**. NRPV crystals have a well-defined rod like morphology while EuCF-RPV particles are spherical and multiple components can be visualized. The black punctate structures in the TEM image of EuCF-RPV represent electron dense EuCF nanocrystals embedded in the less electron dense PCL core (white on image), which also contains RPV. A faint, almost translucent ring around each particle in the TEM image represents a “shell” of lipids that surrounds the EuCF-RPV particles.

2.3.2 In vitro Evaluations of Theranostic Nanoparticles

Macrophages are the effector cells of the innate immune system that have a large capacity to phagocytose bacteria, dead cells, debris, tumor cells, and foreign material [244]. Recent studies demonstrated that macrophages differentiate from hematopoietic stem cell-derived monocytes and embryonic yolk sac macrophages. The former mainly gives rise to “wandering” macrophages which circulate through the body until cytotoxic signaling draws them to sites of inflammation, while the latter mainly gives rise to tissue resident macrophages [245]. Tissue resident macrophages exist in all tissues, including tissue reservoirs of HIV that have proven restrictive to ARV medications. These include the nervous, pulmonary, cardiovascular, gut and renal organs [246]. Additionally,

macrophages are known cellular reservoirs of HIV which herald viral spread to neighboring $CD4^+$ T cells, the principal host cell of the virus [214]. Because of these cells ability to readily phagocytose and store a large amount of particles of nanometer size, their circulation through the body, ability to penetrate and take up long-term residence in tissue reservoirs of HIV, and their status as an HIV cellular reservoir, make these cells an attractive depot to target for our theranostic nanoparticles. Success in the area would see macrophages used as Trojan horse carriers of theranostic nanoparticles.

In order to study the interactions between our theranostic nanoparticles and macrophages, the uptake, retention, subcellular localization, as well as cytotoxicity of nanoparticles were determined *in vitro* in monocyte-derived macrophages. We first determined the effects of EuCF-RPV particle administration on MDM cell vitality. MDM were treated with native non-formulated RPV, NRPV or EuCF-RPV particles at concentrations ranging from 0.2 μM to 200 μM (based on RPV concentration) for 12 hours before cell vitality was measured by MTT assay. As shown in **Figure 2.3A,** native RPV, NRPV and EuCF-RPV particles had little effect on cell vitality up to 50 μM. At the highest concentration tested, 200 μM, NRPV and EuCF-RPV less effected cell vitality than native RPV (82.9%, 56.9% and 37.9%, respectively). Replicate MDMs were treated with ^{111}InEuCF-RPV particles to assess the radioisotope's effect on cell vitality. ^{111}InEuCF-RPV treated cells demonstrated a ~80% cell viability at 8 h at the highest concentration of 8.14 MBq (220 μCi) **(Figure 2.3B)**.

We then examined the uptake kinetics of NRPV and EuCF-RPV in MDM. **Figure 2.3C** shows the RPV concentrations in MDMs treated with various concentrations of NRPV (6.25 μM, 12.5 μM, and 25 μM). At 2, 4, 8, and 12 hours post treatment the media containing RPV was removed, cells were washed with PBS, centrifuged, collected into 1mL PBS and counted. RPV concentration per 10^6 cells was determined by UPLC-with

UV/Vis detection at 285 nm [234]. Maximal uptake at all concentrations occurred at 8 hours post treatment (12.1 μg/10^6 cells at 25 μM) and this value remained stable until 12 hours. We then investigated retention time of NRPV by MDM. After treating with 25 μM NRPV for 8 hours, excess NRPV was removed and replaced with normal cell media. Initially, MDM contained approximately 7.5 μg RPV/ 10^6 cells 24 hour post-treatment (**Figure 2.3D)**. By day 5, the amount of NRPV in cells decreased to 3.2 μg RPV/10^6 cells. NRPV was slowly released between day 5 and day 15 with approximately 0.9 μg RPV/ 10^6 cells remaining at 15 days post treatment.

Next, we evaluated the uptake and retention of EuCF-RPV particles in MDM. For uptake experiments; cells were treated at 25 μM RPV equivalents for up to 12 hours. At various times treatment was removed and cells were washed and collected for drug and metals analyses by UPLC-UV/Vis and ICP-MS. As shown in **Figure 2.3E,** the amount of RPV taken up at 8 hours was similar to that of NRPV (**Figure 2.3C)** (14 μg/10^6 cells and 12.1 μg/10^6 cells, respectively). It is possible that particles break down in the macrophage, releasing some components of the particle and not others. We therefore also examined the uptake and retention of the metal components of the nanoparticles. We measured iron and cobalt levels in these cells and found that at 8 hours cells contained 9.5 μg iron /10^6 cells and 2.9 μg cobalt /10^6 cells. Retention of EuCF-RPV particles in MDM was examined for 15 days. After treating MDM with EuCF-RPV particles for 8 hours at a concentration of 25 μM RPV, treatment media was removed and replaced with fresh media. After 24 hours post treatment, cells retained 9.6 μg/10^6 cells of RPV, 3.6 μg of iron /10^6 cells and 1.0 μg cobalt /10^6 cells. After 7 days the cells had released most particles, retaining 2.0 μg/10^6 cells RPV, 0.7 μg iron /10^6 cells and 0.2 μg cobalt /10^6 cells. Release of particles slowed by day 15 when RPV, iron and cobalt was retained in cells and measured at 0.8 μg, 0.4

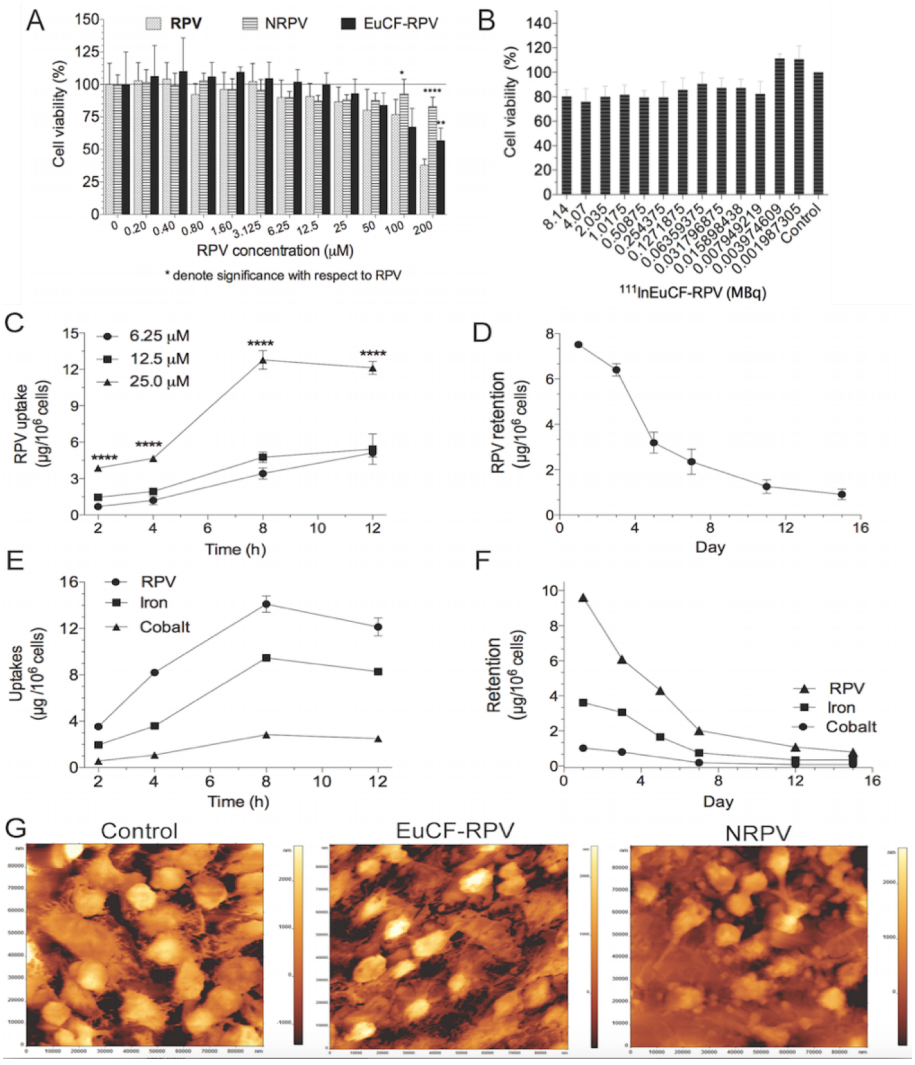

Figure 2.3 In vitro assessments in human monocyte-derived macrophages. (A) MTT cell viability assay of MDMs treated with non-radioactive particles for 12 hours. **(B)** MTT cell viability assay of MDM cells treated with ^{111}InEuCF-RPV particles for 12 hours. **(C)** Uptake of NRPV particles was determined in MDM. NRPV and EuCF-RPV particles were added to MDM at 6.25, 12.5 and 25.0 μM RPV. Stars denote significant differences compared to 12.5 μM RPV (****P < 0.0001) **(D)** 6 Retention of NRPV added to MDM at 25μM RPV for 8h. **(E)** Uptake of EuCF-RPV particles was performed at 25μM RPV. RPV, Iron, and Cobalt concentration (μg/10 cells) were determined after 2, 4, 8 and 12 h of treatment. **(F)** Retention of EuCF-RPV particles over 15 days. MDMs were treated with 25 μM (by RPV) of EuCF-RPV particles for 8 h before treatment was removed. Cells were analyzed for RPV, iron and cobalt concentration (μg/106 cells) at 1, 3, 5, 7, 12, 15 days post treatment removal. **(G)** atomic force microscopy

μg and 0.1 μg/10^6 cells, respectively (**Figure 2.3F**). **Figure 2.3G** shows atomic force microscopy topological images of cells treated with vehicle control, EuCF-RPV, or NRPV.

Interestingly, even though these cells uptake a large number of particles the surface topography of the cells remained unchanged.

In order to evaluate the magnetic sensitivity of our particles and to provide a standard curve by which to estimate iron concentration from MR imaging data, the T_2 relaxivity (r_2) of EuCF-RPV particles was determined for particles suspended in PBS (**Figure 2.4A)** as well as for particles loaded within MDM **(Figure 2.4B)** by using a 7T MRI. The T_2 relaxation rates (R_2) showed a linear correlation (R^2= 0.98) with increasing iron

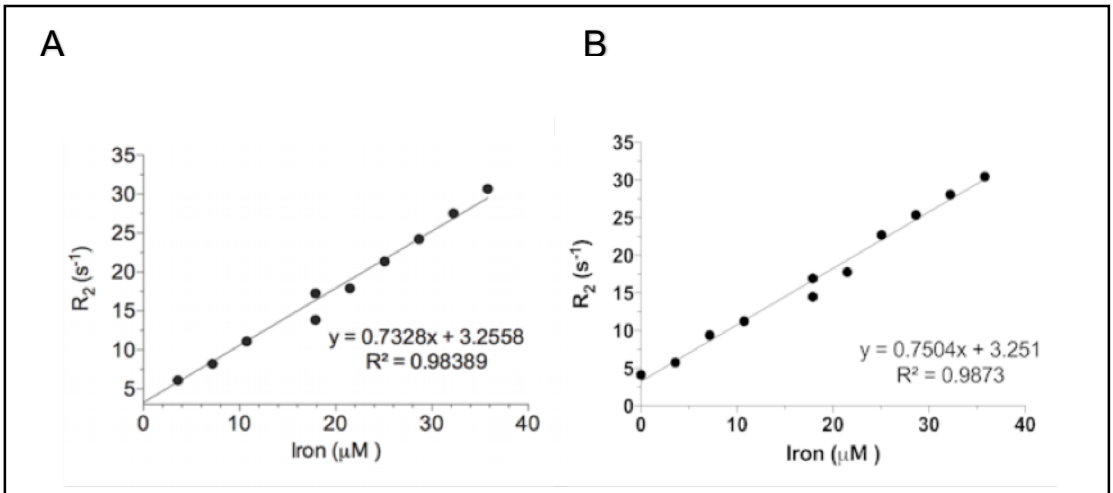

Figure 2.4 T_2 Relaxivity Phantoms in PBS and MDMs. (A) Relaxivity phantoms in PBS. EuCF-PCL particles were suspended in agar at variant concentrations of iron. T_2 relaxation rates (R_2) increased linearly with increasing iron concentration (R^2=0.9873). **(B)** MRI signal enhancement effects of EuCF-RPV particles were determined by calculating particle relaxivity ($\mu M^{-1}s^{-1}$) in human monocyte-derived macrophages (MDM) at various concentrations of iron. (R^2 = 0.98389).

concentration in MDM. Using the slope of this correlation we found that EuCF-RPV particles have an intracellular relaxivity of r_2 = 750.4$\mu M^{-1}s^{-1}$.

2.3.3 Subcellular Particle Localization Studies

We next determined the intracellular fate of NRPV or EuCF-RPV particles in MDM. This was accomplished through qualitative assessments of particle subcellular localization performed by confocal microscopy and TEM. Flow cytometric (FACS) analysis was

performed for quantitative measurements. In order to visualize NRPV by confocal microcopy and for flow cytometry, we synthesized CF®633 labeled poloxamer 407 (P407) as per our previous report [247]. This CF®633-P407 was used for coating during NRPV formulation to create NRPV-CF®633. Cells were treated with 25 μM NRPV-CF®633 or EuCF-RPV particles at a concentration equivalent to 25 μM RPV for 8 hours. At this time the treatment was removed, the cells were washed with PBS, and then fixed in 4% PFA before immunostaining with markers for early endosomes (Rab5), late endosomes (Rab7), recycling endosomal compartments (Rab11 and 14), and lysosomes (LAMP-1). **Figure 2.5A** shows that the majority of NRPV localizes in the late and recycling endosomal compartments enriched in Rab7, 11, and 14. To a lesser degree NRPV can be found in early endosomal compartments enriched in Rab5, and little co-localization with LAMP-1 was detected. Together, these data suggest the retention of NRPV in macrophage endosomal compartments with minimal lysosomal degradation. Similar results were found in cells treated with EuCF-RPV (**Figure 2.5B**) with the exception that there was greater co-localization with Rab5 and 7. Interestingly, EuCF-RPV particles also showed no co-localization with LAMP-1, suggesting that these particles are also retained within macrophage endosomal compartments without significant lysosomal degradation. We used TEM to further confirm the intracellular fate of NRPV and EuCF-RPV particles in greater detail. MDM were treated at 25 μM RPV equivalents of EuCF-RPV or NRPV crystals for 8 hours before removal and cells were fixed for TEM analysis. Large accumulations of EuCF-RPV or NRPV are observed in intracellular subcompartments within the cytoplasm of MDM (**Figure 2.5C)**. Selected intracellular depots of EuCF-RPV and NRPV are outlined in dotted lines in column (i) and then shown at a higher resolution in columns (ii) and (iii). The EuCF nanocrystals are clearly visible as dark spots near the edge of the crystals. Further, the uptake potential of MDM was confirmed by quantitative measurements of NRPV by FCM analysis. The viability dye, propidium iodide was mixed

with treated cells prior to analysis so that only viable cells were analyzed for NRPV

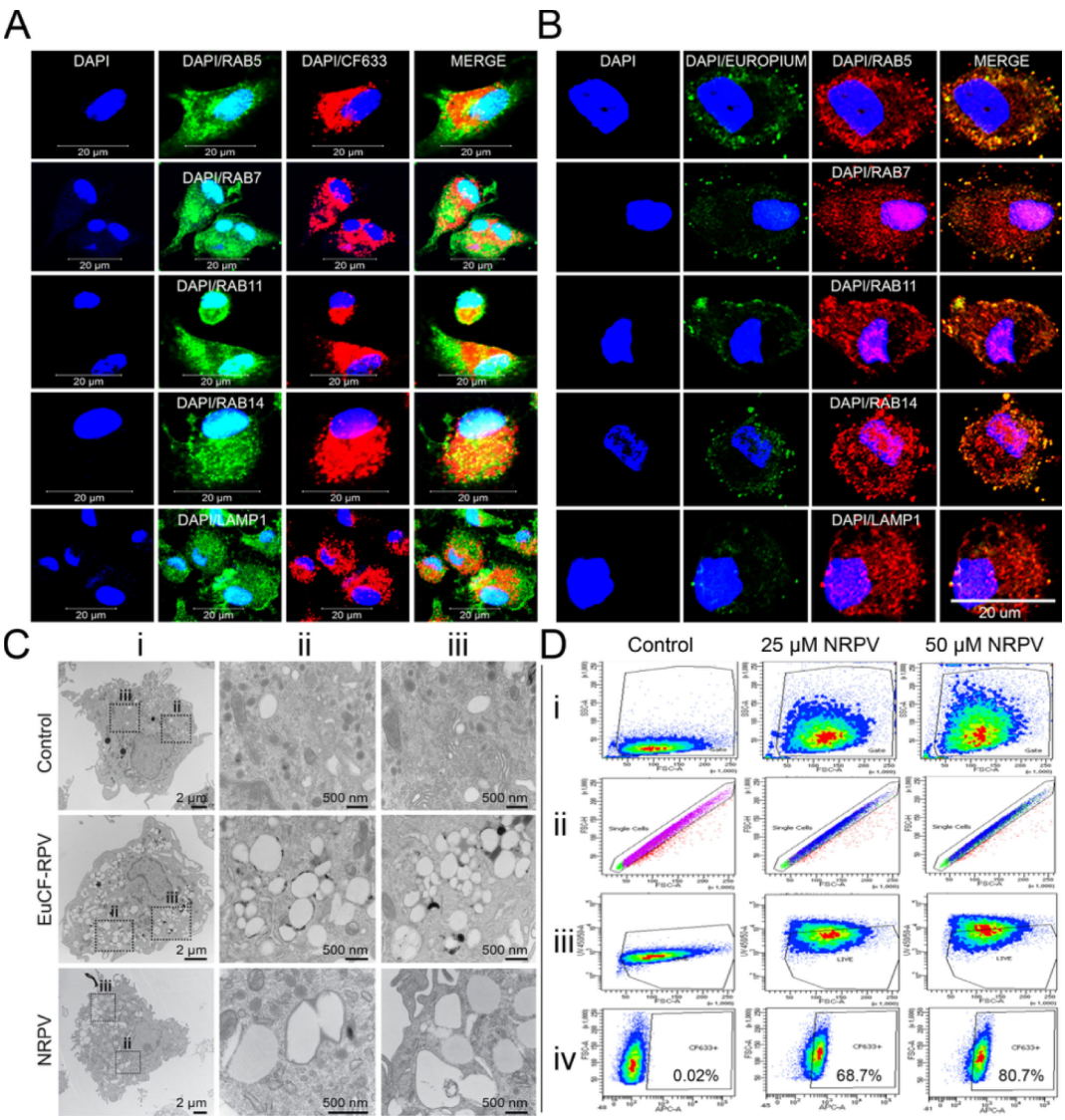

Figure 2.5 Immunocytochemistry, transmission electron microscopy and flow cytometry. Representative images of MDMs treated with Alexa-Fluor 488 secondary antibody against Rab5, Rab7, Rab11, Rab14, or LAMP-1 primaries (green) with **(A)** NRPV-CF®633 (red) or **(B)** EuCF-RPV (green) Nuclei are blue (DAPI). **(C)** TEM ultrastructural evaluation of macrophage particle uptake and subcellular distribution. Areas of interest are bordered with black dotted lines and are presented in corresponding high-resolution images (ii–iii) **(D)** Flow cytometry results for control MDM (left panel) and MDM exposed to NRPV particles (right panels) are shown. **(i)** Population of cells analyzed by scattering analysis plot of control MDM and NRPV treated MDM. **(ii)** Single cell gate, **(iii)** Live/dead MDM gated using propidium and **(iv)** CF®633-NRPV uptake in MDM.

content. As shown in **Figure 2.5D**, we observed that treatment with 25 µM RPV approximately 68.7% of MDM take up NRPV-CF®633, while at 50 µM approximately

80.7% of MDM take up NRPV-CF®633. Overall these results demonstrate that MDM can uptake large amounts of NRPV.

2.3.4 Antiretroviral Activity Measurements

The antiretroviral properties of EuCF-RPV were assessed and compared to native RPV and NRPV in MDM challenged with HIV-1_{ADA}, a prototypical macrophage-tropic strain of HIV [231]. Cells were treated with 6.25 μM, 12.5 μM or 25 μM equivalents of native RPV, NRPV, or EuCF-RPV for 8 hours and removed from cultures. At 1 and 5 days post treatment, cells were challenged with HIV-1_{ADA} for 16 hours at a MOI of 0.1. Cells were maintained for 10 days post infection, at which time progeny HIV virion production was determined by assaying RT activity in the cell culture media. Remaining cells were fixed in 4% PFA and immunostained for HIV-1 p24 antigen expression. At the lowest concentration (6.25 μM) NRPV and EuCF-RPV showed a significant reduction in RT activity at day 1 compared to native RPV, which provided only a small degree of protection **(Figure 2.6A)**. At 5 days post-infection, native RPV and NRPV provided virtually no protection, but EuCF-RPV provided a slight but significant reduction in RT activity compared to positive control. For cells treated with 12.5 μM RPV equivalents, native RPV, NRPV and EuCF-RPV provided significant reduction in RT activity compared to positive control at day 1. By day 5, native RPV provided no protection, yet RT was significantly decreased for NRPV and EuCF-RPV with EuCF-RPV showing the least RT activity. At the highest concentration tested, 25 μM, treatments with all 3 modalities provided significant

protection at days 1 and 5. However, by day 5 protections with NRPV and EuCF-RPV was greater than native RPV alone. These results were confirmed by the p24 immunostaining, which shows less p24 staining in cells treated with NRPV or EuCF-RPV particles compared to native RPV (**Figure 2.6B)**.

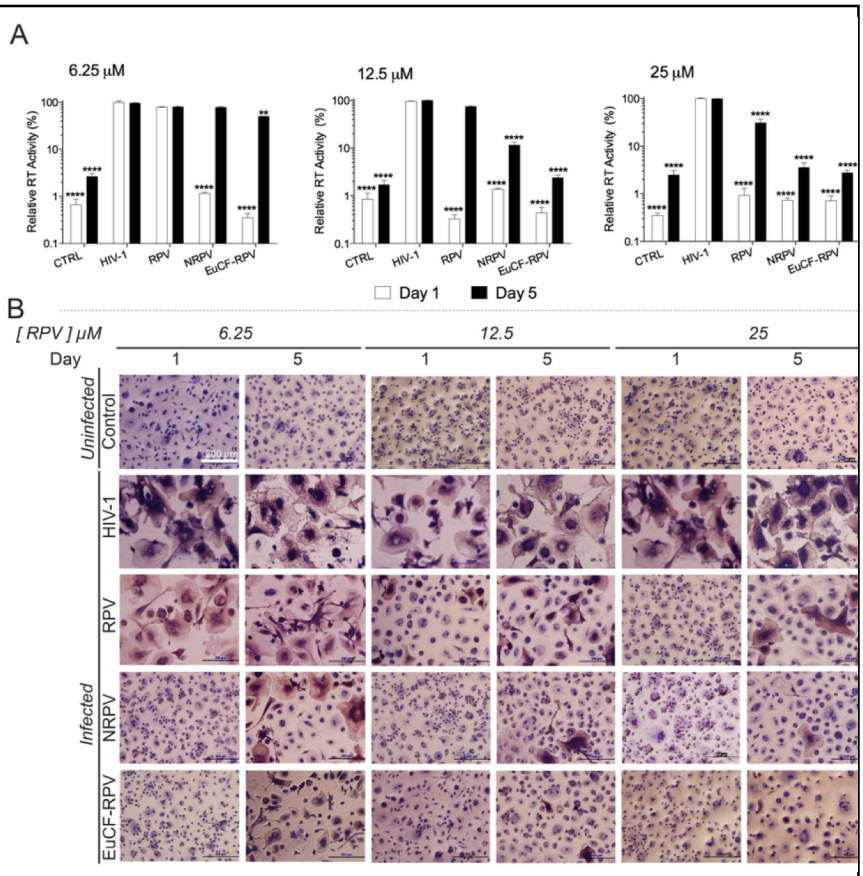

Figure 2.6 Antiretroviral assessments in human monocyte-derived macrophages. **(A)** Progeny HIV virion production was determined by HIV reverse transcriptase (RT) Statistical differences were determined using two-way ANOVA among groups; we used Bonferroni's post hoc test to correct for multiple comparisons. **p < 0.01; ***p < 0.001; ****p < 0.0001. **(B)** HIV p24 staining (brown) counterstained with hematoxylin (blue)

2.4 Discussion

The potential of LASER ART in the prevention, treatment and eradication of HIV/AIDS is of the highest significance [151]. This is linked, in part, to improvements of drug penetration into target organs, reduced systemic toxicities, simplified regimens, reduced pill burdens, and enabling the availability of drug to larger numbers of patients [155]. However, to realize the full potential of LASER ART, formulations in development

must be appropriately screened based upon drug biodistribution and ease of drug penetration into tissue viral reservoirs. While computerized simulations were developed due to the inherent complexity of particle drug parameters this has not proven beneficial [248, 249]. This is based on broad differences in the drug properties, the size, shape and charge of the composed particle, the prodrug lipophilicity, composition and hydrophobicity, the drug loading, encasement and decorations and the inherent tissue and cell physicochemical properties [250, 251]. While others and we have developed such schemes the needs to track particle distribution at the cellular and tissue level to predict drug particle efficacy knows no substitutions from direct measurements [179, 252]. Therefore, there is a clear need to develop such direct screening platforms. To overcome this obstacle, we demonstrated that the biodistribution of ARV loaded theranostic particles by SPECT/CT and MRI imaging modalities effectively correlates with LASER ART drug cell and tissue biodistribution. Our newly crafted, intrinsically radiolabeled multimodal theranostic particles provide a platform to expedite the development of efficient and effective long-acting ART. However, we acknowledge the inherent limitations of the system. Indeed, studies are now being implemented that will address the remaining hurdle including matching the inherent properties (size, shape and surface charge) of the theranostic particles with those particles that would be scaled up for human use [179, 253]. *Second*, as of yet the success of screening theranostic particles decorated with ligands that serve to facilitate optimal drug entry into the most relevant tissue viral reservoirs such as lymphoid tissues and the brain remains unproven [254, 255]. The *third* rests in the use of subcellular drug localizations to maximally restrict targeted components of the viral replication cycle [236]. *Fourth* is the predictive value of not simply measuring drug depots in macrophages but also assessing ARV entry and distribution into the more pathobiologically relevant viral target, the CD4+ effector memory T cell [256]. All must be

taken into account and careful consideration of particle design is required with concomitant evaluations of its predictive value.

In efforts to meet such needs, we have taken a “next step” in our research activities to build upon an already successful theranostics platform that is based upon a “core-shell” system composed of europium-doped, cobalt-ferrite nanocrystals (EuCF), encased in a PCL core, and encapsulated within a lipid shell [179]. The EuCF nanocrystals have a number of properties that can meet the requirements of assessing of LASER ART activities. Notably, the particles sizes are similar to LASER ART and possess strong superparamagnetic properties. This allows their efficient use as a T_2-weighted MRI contrast agents [257]. As MRI tests are broadly available in medical practice and commonly used in medical imaging it certainly offers the needed spatial and temporal resolution and tissue contrast to permit adequate determination of EuCF-drug particle distribution in tissues [258].

However, MRI lacks sensitivity for determining precise drug particle concentrations in tissue [259]. Indeed, imaging alternatives to MRI could improve visualization of particles at low concentrations [260]. Moreover, no single imaging modality is currently available that offers both highly sensitive detection and excellent spatial resolution [261]. This inspired our use of nuclear medicine imaging modalities (SPECT/CT), which provides the highest degree of sensitivity [261, 262]. Additionally, radioactive imaging provides the ability to accurately quantify the concentration of particles in tissue noninvasively [262]. Therefore, combining MRI and SPECT/CT takes advantage of the strengths of both, enabling a clearer evaluation of any of our developed long-acting ARVs.

The stability of the radiolabel is critical for accurate determinations of particle distribution by SPECT/CT as the particle locale is assessed indirectly via a radionucleotide signal [263]. If the radiolabeling strategy can be carefully designed to create a highly stable radiolabel, both its sensitivity and specificity can be optimized. To meet such a challenge,

we intrinsically doped the radioisotope directly into the EuCF nanocrystal lattice. This is different from more common radiolabeling strategies as it does not involve the use of exogenous chelators in forming stable complexes [263, 264]. There are a number of considerations in generating an optimal labeling strategy [188]. *First*, the coordination chemistry of radioisotopes varies significantly. Choosing the right chelator for any specific isotope is challenging, as there are none that can bind multiple radioisotopes [265]. *Second*, incorporation of chelators can alter the hydrodynamic size and surface chemistry, which will alter biodistribution and obscure the true pharmacological behavior of the particles [189, 190]. This fact may be enhanced as the radiolabel could become unbound from particle leading to false positive results [189, 190, 266]. Chelator free labeling forgoes the need for chelating moieties and therefore the native pharmacological behavior of the particle is maintained. *Third*, to optimize labeling the number of chelating moieties conjugated to the particle's surface should not impose any limitations. As intrinsic doping places radioisotopes directly into the lattice sites of the particle's metallic core, abundant labeling sites are available which results in high yields with enhanced stability [191]. *Fourth*, with chelator-free labeling, the surface of the particle can be easily modified with targeting ligands, therapeutic agents, or other imaging agents because no surface functional groups are required for the radiolabel [192]. *Last*, chelator-free labeling is simple, fast, and effective allowing for radiolabeling with a broader spectrum of isotopes, including ^{72}As and ^{69}Ge, both of which have proven extremely challenging to radiolabel via chelator chemistry [267, 268]. Thus, in the current report we intrinsically doped ^{111}In into the core structure of the EuCF nanocrystals. To facilitate the production of the particle, we simply added the radioisotope precursor $^{111}InCl_3$ during the synthesis of the EuCF nanocrystal core. This simple method embeds the radioisotope into the crystal lattice of the core resulting in an intrinsically radioactive particle whose radiolabel was > 97% stable and able to accurately measure particle accumulation at targeted sites.

Any consideration of predictive modeling of the diversity of LASER ART physiochemical properties, excipients, size, shape, charge, encasements and complex pharmacological behaviors (for example, drug subcellular, cellular and tissue distribution, hydrolysis and antiretroviral activities) must include accurate predictive modeling [179, 269-271]. These assessments must include subcellular, cellular and tissue drug distribution studies [179, 253, 270]. Moreover, before any animal injection, the drug particle properties such as uptake, retention, subcellular location, toxicities, and antiretroviral activity were investigated in macrophages and served as confirmation of the current data sets [151, 272]. Dynamic light scattering showed that the hydrodynamic size of the EuCF-RPV particles was similar to that of NRPV. This was confirmed by TEM imaging of both particles. Additionally, encapsulated drug retained potent antiretroviral activities as evidenced by RT and HIV-1p24 activity and staining, respectively. Importantly, the intrinsic fluorescence of Eu allowed for visualization of particle uptake along with subcellular identification of EuCF particles within endosomal compartments identical to those where active viral replication occurs which was consistent with our previous reports [179, 235, 273, 274].

Overall, ^{111}InEuCF-RPV “multimodal imaging theranostic nanoprobes” were made to facilitate the development of targeted LASER ART. The lipid-encapsulated, intrinsically radiolabeled ^{111}InEuCF nanoparticles can fulfill this role by providing a flexible platform with the highest degree of spatial accuracy and sensitivity for the design of diagnostic and therapeutic applications

CHAPTER 3
In vivo Biodistribution of Theranostic Nanoparticles.

3.1 Introduction

To realize the potential of long acting viral reservoir penetrating drugs, pharmacokinetic and pharmacodynamic profile assessment must be performed to minimize on and off-target effects. Because of the greatly extended half-lives of newly emerging LASER ART nanoformulations. Current PK and PD experimental assessments often take weeks to months to perform, and with multiple innovative strategies coming to the forefront of development, such timeframes have proven too tedious and time consuming. Another limitation of current PK and PD analysis is that for tissue drug levels to be determined, the animal must be sacrificed. Therefore, a screening platform that could be used to assess current and predict future drug biodistribution, in living animals, would be of great value in assessing new treatments. While mathematical descriptions of long-acting nanoformulated drug distribution have been developed, these cannot reflect the diversity of chemical alterations and physical characteristics now required for LASER ART nanoformulations [224]. To overcome these technical and biologic challenges, multimodal decorated nanoparticles were produced where hydrophobic ARVs and bioimaging agents were encased in a single nanoformulation. Highly stable europium cobalt-ferrite (EuCF) nanocrystals, intrinsically radiolabeled with ^{111}indium were loaded with the ARV drug, rilpivirine (RPV), creating an all-in-one “multimodal imaging theranostic nanoparticle”.

The newly minted drug particles facilitated real-time non-invasive detection of drug and antiretroviral drug biodistribution and screening by both MRI and SPECT/CT imaging modalities. Combining spatial specificity of MRI with the quantitative sensitivity of SPECT/CT allowed for precise assessments of drug distribution and drug concentration in real time. These findings forge a significant improvement over first generation EuCF-PCL particles [179] by extending ARV encapsulations and bioimaging capabilities to

assess drug biodistribution. *In* vivo MRI and SPECT/CT imaging and quantification of ^{111}InEuCF-RPV particle distribution over a week provided strong correlations with tissue RPV levels up to one month post intravenous injection. Validation of this predictive potential is provided by ultra-performance liquid chromatography tandem mass spectrometry (UPLC-MS/MS) and inductively coupled plasma mass spectrometry (ICP-MS) made possible by the metals encased in the particles. TEM analysis of reservoir tissues showed accumulation of theranostic particles in tissue resident macrophages. Histological evaluations of various tissues after treatment with particles show no significant deviations from tissue derived from untreated animals. This provides evidence that particles are non-toxic. The data demonstrate, for the first time, that theranostics ARV particles can provide a platform to facilitate clinically effective LASER ART development.

3.2 Materials and Methods

3.2.1 Animals

Male Balb/cJ (6-7 weeks old) were purchased from Jackson Laboratories (Bar Harbor, Maine, USA). Animals were housed in the University of Nebraska Medical Center (UNMC) laboratory animal facility according to the Association for Assessment and Accreditation of Laboratory Animal Care guidance. All protocols related to animal experiments were approved by the UNMC Institutional Animal Care and Use Committee and met the requirements and ethical guidelines set forth by the National Institutes of Health in handling laboratory animals for research

3.2.2 Tissue Biodistribution of Multimodal Theranostic Nanoparticle

For multimodal imaging and biodistribution studies; ^{111}InEuCF-PCL/RPV, ultra-small lipid coated ^{177}LuEuCF and NRPV particles were injected intravenously into mice at variant concentrations of drug or radioisotope (**Table 3.1**). As shown, male Balb/cJ mice (6-7 weeks old) were divided into eight groups (n= 10 to 15 mice per group) and intravenously injected with various doses of theranostic and/or NRPV particles. The first group (G1) received NRPV particles at 45 mg RPV/kg. The second group (G2) received NRPV particles at a lower dose of 5 mg RPV/kg. The third group (G3) received EuCF-PCL particles (2mg/kg iron) only. The fourth group (G4) was administered EuCF-RPV particles (2 mg/kg iron). The fifth (G5) and sixth (G6) groups received two sequential injections, first EuCF-PCL particles (2 mg/kg iron) and then NRPV particles (45 mg RPV/kg for G5 and 5 mgRPV/kg for G6, respectively). The seventh group (G7) underwent SPECT/CT imaging after receiving^{111}InEuCF-PCL particles ~ 22.2 MBq (600 µCi) and the final group (G8) was treated with ultra-small lipid coated ^{177}LuEuCF particles ~ 74 MBq (2000 µCi) to assess the effect of particle size on biodistribution. For plasma drug quantitation, 100 µL whole blood was collected by cheek puncture into lithium heparin coated tubes at 1, 3, 5, 7, 14, 21, and 28 days post injection. For tissue drug and metal biodistribution analysis, five animals from each group were euthanized at

Table 3.1 Treatment groups for correlative biodistribution experiment.

Groups	Formulations	Multimodal test					
		MRI		SEPCT/CT		Radioactivity	UPLC-MS/MS
		Dose (mg/kg)		Time			
		RPV	Iron	Days	Hours	Days	Days
G1	NRPV	45	--	--	--	--	1,2,3,5,7,1,14,21,28
G2	NRPV	5	--	--	--	--	1,2,3,5,7,1,14,21,28
G3	EuCF-PCL	2	2	--	--	--	2, 5
G4	EuCF-PRV	2	2	2, 5	--	--	2, 5
G5	EuCF-PCL + NRPV	45	2	2, 5	--	--	--
G6	EuCF-PCL + NRPV	5	2	--	--	--	--
G7	^{111}InEuCF-PCL	600 uCi	--	--	4, 12, 24, 48, 120	2, 5	--
G8	^{177}LuEuCF	2000 uCi	--	--	6, 24, 48, 120	1, 2, 5	--

2, 5 and 28 days post treatment and eight tissues were dissected (liver, spleen, lung, gut, brain, axillary and popliteal lymph nodes and kidneys).

3.2.3 UPLC-MS/MS Analysis of RPV in Plasma and Tissues

For analysis of RPV in plasma, to 25 µl of plasma, 10 µL of internal standard (IS) solution (250 ng/mL indinavir and 500 ng/ml lopinavir; final concentration 25 ng/ml indinavir, 50 ng/ml lopinavir) was added along with 1 ml of ice-cold Optima-grade acetonitrile. Samples were then vortexed and centrifuged at 17,000 g for 10 min at 4°C. Supernatants were evaporated using a Thermo Scientific Savant Speed Vacuum (Waltham, MA, USA) and reconstituted in 100 µL 50% (v/v) optima-grade methanol in optima-grade water. Standard curves were prepared in blank rat plasma in the range of 0.2–2000 ng/mL RPV with 10 µL of IS added. For tissue analyses, 100 mg of tissue was homogenized in 4 volumes of 90% (v/v) Optima-grade methanol in Optima-grade water using a Qiagen Tissue Lyzer II (Valencia, CA, USA). To 100 µL of tissue homogenate, 80 µL of 100% Optima-grade methanol, 10 µL of 50% Optima-grade methanol (v/v) in MS-grade water, and 10 µL IS was added. Standard curve samples were prepared using equivalent tissue matrix dilutions, to which were added 80 µL of Optima-grade methanol, 10 µL of 50% Optima-grade methanol (v/v) in Optima-grade water spiked with standard drug concentrations and 10 µL of IS. Chromatographic separation of 10 µL of plasma or tissue samples was achieved with an ACQUITY UPLC-BEH Shield RP18 column (1.7 µm, 2.1 mm x 100 mm) using a 7-min gradient of mobile phase A (7.5 mM ammonium bicarbonate in Optima-grade water adjusted to pH 7 using acetic acid) and mobile phase B (100% Optima-grade methanol) at a flow rate of 0.25 mL/min. The initial mobile phase composition of 70% B was held for 4.75 min and was increased to 95% B in 0.25 min then held constant for 0.75 min. Mobile phase B was reset to 70% in 0.25 min and the column was equilibrated for 1.0 min before the next injection. RPV was detected at a cone voltage

of 92 volts and collision energy of 56 volts. Multiple reaction monitoring (MRM) transitions used for rilpivirine, indinavir and lopinavir were 367.032 > 127.859, 614.14 > 97.023, and 629.177 > 155.031 m/z, respectively. Spectra were analyzed and quantified by MassLynx software version 4.1 using the ratio of analyte peak area to IS peak area. Tissue cobalt was analyzed by ICP-MS as described previously [275].

3.2.4 MRI Analysis of the Biodistribution of Theranostic Nanoparticles in Mice

EuCF-RPV (G4) and EuCF-PCL biodistribution studies were performed with co-injected NPRV particles (G5). These experiments were performed using male Balb/cJ mice (6-7 weeks old, n = 10). MRI scanned mice immediately prior to intravenous injection of particles to provide a baseline scan for comparisons. MR images were acquired 2 and 5 days after treatment using a 7T/16 cm Bruker PharmaScan and a home-built RF coil for signal transmitting and receiving. T_2 mapping was used to determine the biodistribution of EuCF-RPV particles as previously described [276] with the following modified scanning parameters. For T_2 mapping, a CPMG phase cycled 3-dimensional multi-echo sequence data acquired with 24 echoes (echo times TE_n = n x 2.638 ms; n = 1, 2, 3... up to 24), 400 ms repetition time, 120 × 144 × 58 acquisition matrix, 40 × 40× 22 mm field of view (FOV), one average, for a total acquisition time of 56 min. After post scans, mice were anesthetized with isoflurane, sacrificed via cardiac puncture, and perfused with sterile PBS. Organs were then collected for drug and metals content analysis (liver, spleen, kidney, lung, GALT, and brain). Additionally, mice were bled via facial vein puncture after the day 2 and 5 post-scans. Blood was collected into lithium heparin coated tubes and centrifuged at 2,000 x g for 10 min to collect plasma for drug and cobalt analysis by UPLC-MS/MS and ICP-MS, respectively

3.2.5 Theranostic Nanoparticle Biodistribution by SPECT/CT

In vivo biodistribution of ^{111}InEuCF-PCL particles was determined in male Balb/cJ mice (6-7 weeks old, n= 10, G7) via SPECT/CT. On day 0 all mice received a single intravenous injection of ~22.2 MBq (600 μCi) of ^{111}InEuCF-PCL particles. Image acquisition was performed at 4, 12, 24, 48, and 120 hours post injection by a hybrid single photon emission computed tomography system and x-ray computed tomography (SPECT/CT) (Flex Triumph, TriFoil Imaging, Northridge, CA, USA) fitted with a five pinhole (1.0 mm per pinhole) collimator. First CT images were acquired using 360 projections over 360° with an x-ray tube current of 140 mA and voltage of 75 kilovoltage peak (kVp) at a magnification of 2.0 (field of view = 59.2 mm^2). Immediately after, SPECT/CT image acquisition was performed with the following parameters; 64 projections at 10 seconds per projection over 360° using a radius of rotation (ROR) of 48 mm (field of view= 59 mm^2). Co-registration of anatomical CT images and functional SPECT was performed by 3D visualization and analysis software, VivoQuant 3.5 (Invicro Boston, MA, USA). Regions of interest (ROIs) were drawn over various organs and the radioactivity and organ volume were determined to calculate gamma counts per cubic millimeter (mm^3). After days 2 and 5 scans, mice were sacrificed and various organs including the heart, lung, liver, pancreas, stomach, spleen, small intestine, large intestine, kidneys, bladder, lymph node, muscle, bone, brain, injection site (tail), remaining carcass and blood were collected, weighed, and analyzed *ex vivo* for radioactivity using gamma scintillation spectrometry. Additionally, animals were individually caged so that excreted signal could be measured from the bedding. Signal measured was back calculated to the time of injection to account for radioactive decay of ^{111}In ($t_{1/2}$ = 67.2 h). Signal from each organ was divided by the sum of total counts from all sources and then divided again by the weight of the organ to obtain

percent-injected dose per gram of tissue (% ID/g). For the ultra-small (~ 5 nm) particle biodistribution study, 15 male Balb/cJ mice (6-7 weeks old) were intravenously injected with ~ 74 MBq (2,000 μCi) of lipid-coated ^{177}LuEuCF particles (G8). Mice were then scanned by SPECT/CT using the same parameters as previously described for the ^{111}InEuCF-PCL particles at 6, 24, 48, and 120 hours post injection. After scanning at 24, 48, and 120 hours, 5 mice were sacrificed and organs were collected for *ex vivo* gamma counting in the same manner as for ^{111}InEuCF-PCL particles except that the half-life of ^{177}Lu ($t_{1/2}$ = 6.64 days) was used for back calculating radioactivity.

3.2.6 Theranostic Nanoparticles for Prediction of Long-Term Rilpivirine Biodistribution

For multimodal imaging, non-invasive MRI and SPECT/CT were performed to assess theranostic particle biodistribution. As shown in **Figure 3.1** First, MRI was performed on mice receiving EuCF-RPV (G4) and EuCF-PCL plus NRPV (G5) at 2 and 5 days post injection. These images were quantified for approximate iron concentration using phantom relaxivity data acquired in MDM. SPECT/CT imaging was performed on mice that received ~22.2 MBq (600 μCi) of ^{111}InEuCF-PCL (G7) and ~ 74 MBq (2000 μCi) of ultra-small lipid coated ^{177}LuEuCF (G8) particles. For *ex vivo* tests, gamma scintillation spectrometry

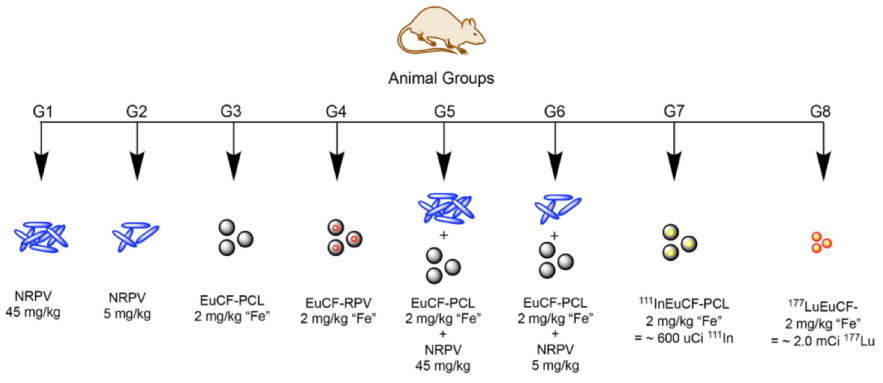

Figure 3.1 Schematic diagram of treatment groups used in the in vivo pharmacokinetic/bio-distribution correlation study. Figure display groups injected with EuCF-RPV, EuCF-PCL and/or NRPV, ^{111}InEuCF-PCL or ^{177}LuEuCF particles in Balb/cJ mice.

was performed on tissues recovered from mice injected with ^{111}InEuCF-PCL (G7) and ultra-small ^{177}LuEuCF (G8) particles. The degree of correlation between the following data sets was determined; RPV concentration in tissues as determined by UPLC-MS/MS, iron concentration by MRI, radioactivity by SPECT/CT, *ex vivo* gamma scintillation spectrometry, and cobalt concentration determined by ICP-MS. To assess *in vivo* toxicity of the injected particles, the mice were sacrificed at 28 days, and liver, spleen and kidney were collected and fixed in 10% neutral buffered formalin for histological analysis. To determine the real time drug biodistribution prediction capabilities of the particles, the results from advanced molecular imaging techniques were correlated with drug and metal quantitative results from independent groups. For the first set of comparisons, RPV concentration (ng/mL), iron concentration (ng/mL), cobalt concentration (μg/mL), SPECT/CT signal (counts/mm^3), or gamma counts (% ID/g) were each averaged across all groups by tissue (liver, spleen, lymph node) and Pearson's correlation coefficients for each 2 parameter comparison (for example: RPV in liver vs. SPECT/CT signal in liver) were determined. For the second set of comparisons, each group was considered separately. For each group, these data were averaged by tissue and day of sacrifice. The tissue per day averages were then compared to the same tissue per day averages from every group and Pearson's correlation coefficients were calculated for each comparison. Statistical differences were determined using a two-way ANOVA among groups followed by Bonferroni multiple comparison test. P values ≤ 0.05 were considered significant.

3.2.7 Autoradiography

Liver, lungs and spleen were excised at 1, 2 and 5 days post injection from mice treated with ^{111}InEuCF-PCL or ^{177}LuEuCF particles. Collected tissues were washed with deionized water and immediately embedded into optimal cutting temperature (O.C.T)

compound (Fischer HealthCare, Waltham, MA, USA). Cryostat sections (10 μm) of tissue samples were prepared and exposed to a phosphor screen for 5 days in the dark (Leica CM1850, Leica Biosystems Inc, Buffalo Grove, IL, USA). The phosphor screen was subsequently imaged by a Typhoon FLA 9500 variable mode imager (GE Lifesciences, Pittsburg, PA, USA) at 25 μm resolution.

3.2.8 Tissue Localization and Toxicity

Particle distribution within the spleen and liver from mice treated with EuCF-PCL (G3) and NRPV (G5) was evaluated via TEM. For TEM examination, tissue samples were fixed in TEM buffer at room temperature. Tissue processing and sectioning were performed as previously described [276]. *In vivo* toxicity of the EuCF-RPV particles was determined by histological examination. For histological examination, 5 μm sections of paraffin-embedded tissues were fixed to glass slides and stained with hematoxylin and eosin and a TUNEL assay was performed as per as per manufacturer's instructions. Images were captured with a Nuance EX multispectral imaging system affixed to a Nikon Eclipse E800 microscope (Nikon Instruments, Melville, NY, USA) using a 20× objective. Histopathological assessment was conducted in accordance with the guidelines of the Society of Toxicologic Pathology.

3.2.9 Statistical Analyses

For all studies, data were analyzed using GraphPad Prism 7.0 software (GraphPad, La Jolla, CA, USA) or Statistica v9 (Statsoft, Inc., Tulsa, OK, USA) and are presented as the mean ± standard error of the mean (SEM). For comparisons of two groups, Student's "t" test (two-tailed) was used. Experiments with multiple time points were analyzed using two-way ANOVA, to assess treatment versus control groups over multiple

time points and Bonferroni's post hoc tests for multiple comparisons.

3.3 Results

3.3.1 Real Time in vivo Biodistribution Tests in Mice

3.3.1.1 MRI Modality

The goal of these studies is to use multimodal theranostics for non-invasive real time tracking of drug biodistribution in animals by using MRI and SPECT/CT imaging. **Figure 3.2A** depicts the experimental timeline for the MRI and SPECT/CT studies. MRI pre-scans were taken before injection of EuCF-RPV (G4) or EuCF-PCL plus NRPV (G5) to establish a baseline signal and representative pre-scans are shown in **Figure 3.2B**. MRI was chosen as the first modality because of its superior spatial resolution, which provides the most accurate information about the localization of these particles in soft tissues [259]. Post-injection MR images were acquired 2 and 5 days after particle intravenous administration **(Figure 3.2B).** After 2 days post-administration mice were scanned again and the resulting images were analyzed for the presence of particles. T_2 signals were decreased in both liver (outlined in red) and spleen (outlined in green), which visually confirms the presence of supraparamagnetic particles. A similar decrease in T_2 was observed 5 days post-injection signifying the retention of particles in those organs over time.

3.3.1.2 Nuclear Imaging Modality

Taking advantage of increased sensitivity over MRI, SPECT/CT imaging was also performed. By combining MRI and SPECT/CT modalities the distribution of particles can be accurately determined with a high degree of spatial resolution and sensitivity. To make the EuCF-PCL particles suitable for SPECT/CT imaging, Indium-111 (^{111}In) was

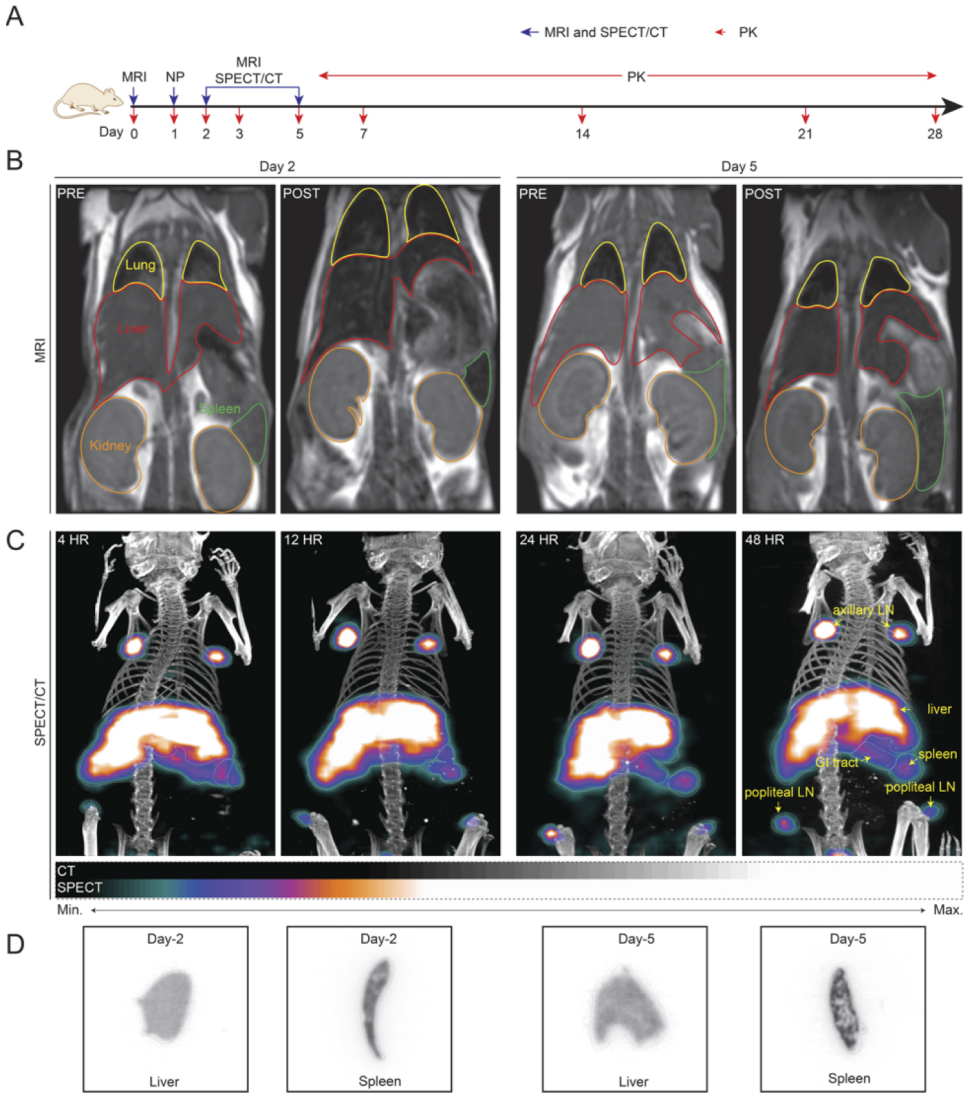

Figure 3.2 Multimodal theranostics tests. (A) Time line of the experimental procedure in mice is shown (NP: nanoparticles). **(B)** Representative pre-scan and post-scan T_2 maps of mice 2 and 5 days after intravenous injection administration of EuCF-RPV (2 mg iron/kg) particles (G5) (yellow: lung; red: liver; green: spleen; orange: kidney). **(C)** Two-dimensional image representations of three-dimensional SPECT/CT scan of mice treated intravenously with ~22.2 MBq (600 μCi) of ^{111}InEuCF-PCL particles. **(D)** Autoradiographic images of liver and spleen sections from mice sacrificed 2 and 5 days post injection with ^{111}InEuCF-PCL particles.

intrinsically labeled directly into the EuCF nanocrystal lattice (^{111}InEuCF-PCL). For the SPECT/CT experiment, 10 mice were injected at a dose corresponding to ~ 22.2 MBq (600 μCi) and subsequently scanned at 4, 12, 24, 48, and 120 hours (5 days) post injection. In mice scanned 4 hours post-injection, the majority of particles localized to the

liver, spleen, and axillary lymph nodes, with modest accumulation in the popliteal lymph nodes (**Figure 3.2C**). By 12 hours post-administration, the popliteal lymph nodes were clearly visible and persisted until day 5. Particles continued to accumulate in the spleen, liver, and lymph nodes until 48 hours post-injection. Intense labeling can be seen in the upper thoracic region which most likely represent axillary lymph nodes. Axillary lymph nodes were dissected out and radioactivity was confirmed by gamma scintillation, *ex vivo.* By 5 days post-injection, particle concentrations had decreased in the liver and lymph nodes. However, particle accumulation in the spleen slightly increased by day 5 compared to day 2, but did not rise to significance. After the 2 day and 5 day SPECT/CT scans, mice were sacrificed so that the livers and spleens could be excised, flash frozen and fixed for autoradiographic imaging. Autoradiography analysis of liver and spleen tissues visually confirmed the slight decrease in liver signal between 2 and 5 days as well as the increase in spleen signal over the same time period (**Figure 3.2D)**. Location of particles in the spleen appears diffuse on day 2, but the signal coalesces into discrete areas by day 5. This most likely represents a transfer of particle from the red pulp of the spleen into the marginal zones and white pulp, which are the primary locations of splenic macrophages [277].

The biodistribution of particles was dependent on surface chemistry, size, and shape [229]. To this end we prepared, ultra-small, lipid-coated lutetium (^{177}Lu) intrinsically radiolabeled EuCF nanocrystals (^{177}LuEuCF) with an average size of ~ 5 nm for SPECT/CT to investigate differential biodistribution by modulating the size of the particles. Mice underwent SPECT/CT scanning at 6, 24, 48 and 120 hours (5 days) post-intravenous administration of ~ 74 MBq (~2000 µCi) of lipid-coated ^{177}LuEuCF particles (**Figure 3.3A)**. At each time point, representative images of SPECT/CT scans were acquired of the torso and of the thoracic cavity at lower radius of rotation (higher magnification). The images show preferential early distribution of these particles into the lungs at 6 hours post-

administration with a small amount in the liver and spleen. At 24 hours accumulation in the lungs peaked and was beginning in the spleen and liver. By 48 hours, the signal in the lung began to decrease, indicating a clearance of particle from lung tissue. At the same time, accumulation in the liver was clearly visible as well as in the spleen. Interestingly this trend continued to day 5 with more accumulation in the liver and a sharp decrease in lung signal (**Figure 3.3B)**. Signal in the spleen remained relatively constant between days 2 and 5. These observations were supported by 3D quantitation of the SPECT/CT signal (counts per mm^3) (**Figure 3.3C)**. For additional verification of these results, mice were sacrificed after 24, 48, and 120 hour scans and various organs were collected which included, but not limited to, lung, liver, and spleen. All organs were weighed and the radioactivity measured to calculate the percent-injected dose per gram (%ID/g) for each tissue. As shown in **Figure 3.3D,** 176 %ID/g of the particle accumulated in the lungs, 38 %ID/g had accumulated in the liver and 34.5

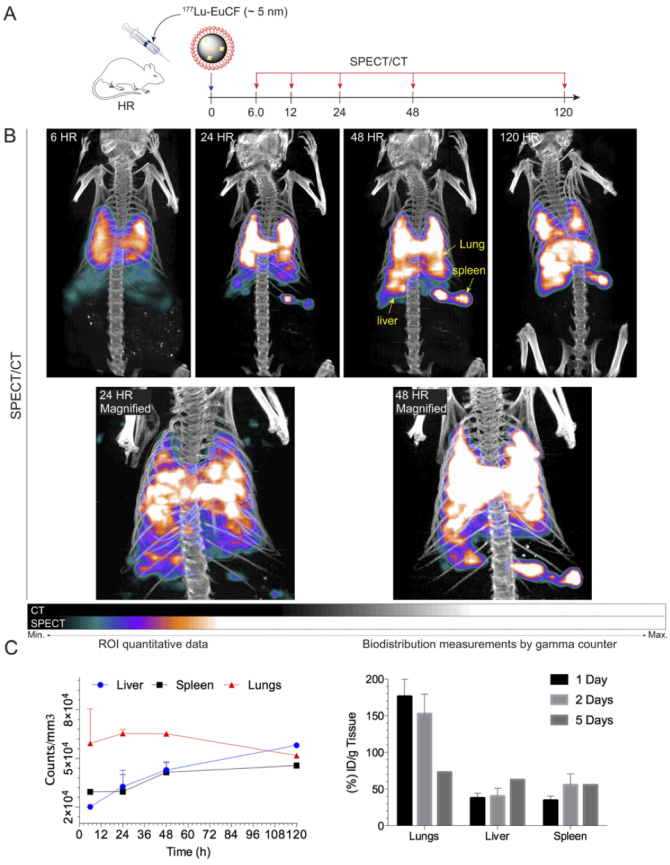

Figure 3.3 Effect of ultra-small particle size on theranostic particle biodistribution determined by SPECT/CT. In vivo biodistribution of ultra-small lipid coated ^{177}LuEuCF particles (~74 MBq) was assessed in mice by SPECT/CT. **(A)** Experimental timeline for ^{177}LuEuCF particles biodistribution study. **(B)** Representative images of 3D SPECT/CT acquisitions **(C)** Left: 3D quantification of SPECT signal using VivoQuant software displayed in counts/mm3. Right: Ex vivo radioactivity biodistribution by gamma counting.

%ID/g was found in the spleen by 24 hours. At 48 hours the amount of particles in the lung had dropped to 153 %ID/g while particle accumulation in the liver and spleen had increased to 40 and 55 %ID/g, respectively. By day 5 more than half of particles had cleared from the lung leaving 73% ID/g. However, signal continued to increase in the liver (63% ID/g) and held steady in the spleen (56% ID/g). This *ex vivo* radioactivity was verified by autoradiographic evaluation of the liver, spleens and lungs from these mice sacrificed 1 and 2 days post injection as shown in **Figure 3.4.**. Additionally, we could not detect ultra-small particles in any lymph nodes however, the most striking feature of these images is the increase in signal seen in the spleen from 24 hours to 48 hours. Overall, we conclude that intravenously injected particles must be of appropriate size in order to effectively penetrate into lymph nodes. These results confirm the biodistribution pattern we observed by SPECT/CT

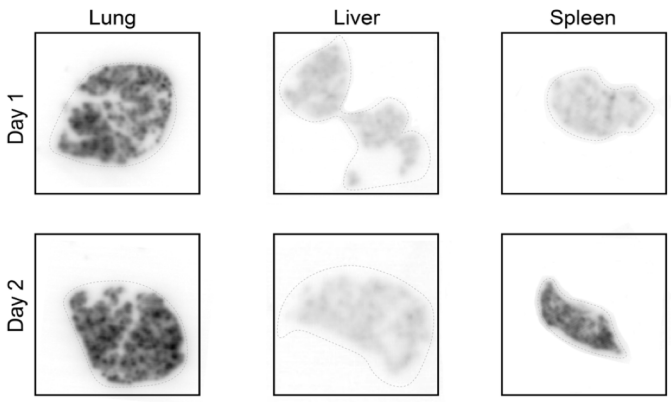

Figure 3.4 Ex vivo autoradiography. Autoradiographic images of lung, liver and spleen sections from mice sacrificed 1 and 2 days post injection with ultra-small ^{177}LuEuCF particles. Most notable is the strong increase in signal in the spleen between days 1 and 2.

3.3.2 Predictive Capabilities of Theranostic Nanoparticles for Rilpivirine Biodistribution

Long-term prediction of disease progression, drug biodistribution and dose optimizations for long-acting HIV medications is difficult, laborious and time consuming

using conventional pharmacokinetics and biodistribution assessments [151, 153]. Therefore, a theranostic imaging platform would be advantageous to build a data library that can be used to predict drug biodistribution in patients with more precision than traditional pharmacokinetics analysis without invasive isolation of tissues samples [179, 196]. We hypothesized that imaging data acquired from our multimodal theranostic imaging platform would correlate with drug concentration and provide information about the long-term biodistribution of long-acting antiretroviral medications. In order to test this hypothesis, we examined the pharmacokinetic and biodistribution profiles of eight different treatment groups, each group containing 10 to 15 Balb/cJ mice over the course of one month. All treatments were administered via intravenous injection to healthy Balb/cJ mice. As shown in **Figure 3.1** and **Table 3.1** two groups received only NRPV at a high (45 mg/kg) (G1) or low (5 mg/kg) dose (G2). The third group was administered EuCF-PCL particles (2 mg/kg iron) (G3) and the fourth was injected with EuCF-PRV particles (2 mg/kg iron) (G4). Groups 5 and 6 received a dual injection of EuCF-PCL particles (2 mg/kg iron) and NRPV at 45 mg/kg (G5) or 5 mg/kg (G6). In each group five mice were sacrificed at days 2, 5 and 28. At the time of sacrifice, organs were excised and analyzed by UPLC-MS/MS and ICP-MS for drug and metal content, respectively. Plasma was also collected from mice at days 1, 2, 3, 5, 7, 14, 21, and 28 and analyzed for drug and/or metal content to build a complete biodistribution profile for each treatment group. We then compared this month of pharmacokinetic and biodistribution results to the bioimaging data obtained within the first five days post injection from MRI scans of G4 and G5. Lastly, ^{111}InEuCF-PCL or lipid coated ^{177}LuEuCF particles were given intravenously to groups 7 (G7) and group 8 (G8), respectively, for SPECT/CT analysis. We then used these data sets for correlation analyses comparing drug versus metals content or signal quantified through imaging to estimate the ability of our multimodal particles to rapidly assess and predict long term biodistribution of long-acting antiretroviral medications.

By MRI analysis, EuCF-RPV particles (G4) showed similar biodistribution as EuCF-PCL particles injected alongside NRPV (G5) on day 2 and day 5 post injections **(Figure 3.5A)**. The amount of iron present in the liver and spleen at 2 and 5 days was quantified using phantom relaxivity standard curves generated from EuCF-RPV particles in MDM at varying concentrations of particles (by iron) as shown in **Figure 2.2H and Figure 2.2I.** In both groups iron concentrations decreased between days 2 and 5 in the liver. This decrease was not significant for EuCF-RPV (2.4 to 2.1 ng/mL) but was significant for EuCF-PCL plus NRPV (1.9 ng/mL to 1.1 ng/mL). In contrast, there was a slight increase in iron concentration in the spleen over the same time in both groups. Iron levels in the spleen increased from 1.0 to 1.6 ng/mL for EuCF-RPV and from 1.0 to 1.4 ng/mL for EuCF-PCL plus NRPV. G7 mice were administered ^{111}InEuCF-PCL particles and assessed by SPECT/CT at 4, 12, 24, 48, and 120 hours post-injection. Acquired images were reconstructed to 3-D renditions, regions of interest (ROI)

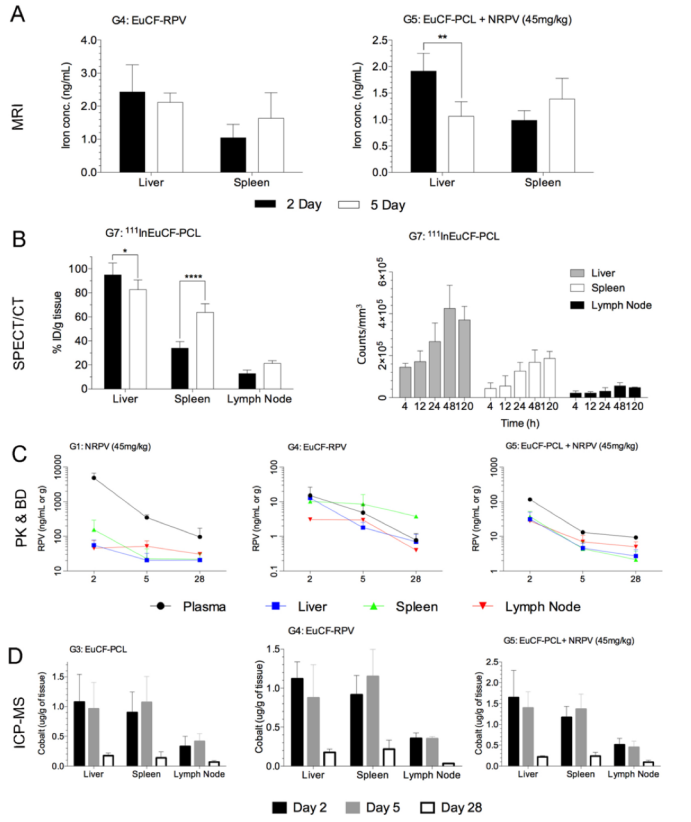

Figure 3.5 Biodistribution and pharmacokinetic analyses. (A) Quantification of iron content in liver and spleen by MRI. **(B)** Left: %ID/g radioactivity in liver, spleen, and lymph nodes from mice treated with 111InEuCF-PCL. Right: Quantification of SPECT/CT signal by 3D **(C)** RPV drug levels in plasma, liver, spleen, and lymph nodes from days 2, 5, and 28 as determined by UPLC-MS/MS. **(D)** Cobalt content from groups (G3, G4, and G5) treated with EuCF-PCL/RPV and NRPV particles in liver, spleen, and lymph node from days 2, 5, and 28 as determined by ICP-MS. *p < 0.05, **p < 0.01, ****P < 0.0001.

were electronically drawn to encompass organs, and relative activity counts per cubic millimeter for each tissue were determined. Activity in liver, spleen, and lymph nodes (axillary and popliteal) increased until 48 hours post injection with the majority of particles localizing in the liver (**Figure 3.5B)**. By five days post injection, activity in liver and lymph nodes decreased slightly while splenic activity increased. The SPECT/CT results were confirmed by determining tissue drug levels in mice after scans on days 2 and 5. All organs were removed and particle biodistribution measured by gamma scintillation spectrometry. The results are presented in **Figure 3.5B** as % ID/g. There was a significant accumulation of particles in the Liver (73.5% ID/g), Spleen (41.1% ID/g), and axillary or popliteal lymph nodes (13.5% ID/g). Interestingly, at 5 days post injection there was a large increase in distribution of these particles to the spleen (63.3% ID/g) with modest clearance from the liver and small increases in the lymph nodes by day 5 (62.6% ID/g and 18.0% ID/g, respectively).

In all animal groups that received NRPV or EuCF-RPV particles, drug levels were measured in plasma collected on days 1, 2, 3, 5, 7, 14, 21, and 28 after treatment. Tissues were collected from mice on days 2, 5, and 28 for UPLC-MS/MS determination of drug levels. Drug levels in plasma and tissues for the EuCF-RPV treatment group were lower than those found in groups treated with NRPV at 45 mg/kg or EuCF-PCL particles with a co-injection of NRPV at 45 mg/kg (**Figure 3.5C**). The values observed were similar to values obtained from groups treated with the lower concentration of NRPV (5 mg/kg) (**Figure 3.6).**

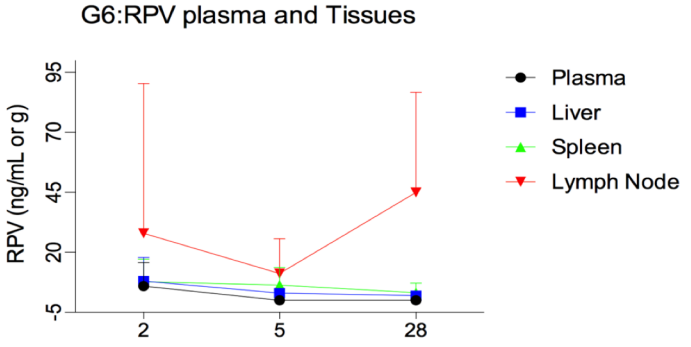

Figure 3.6 Pharmacokinetics and biodistribution of the co-injected EuCF-PCL (2 mg/kg iron) and NRPV (5 mg/kg RPV) particles (G6)

In groups that received theranostic particles, (G3, G4, G5, and G6) mice were sacrificed on days 2, 5, and 28, and their organs were removed and analyzed by ICP-MS for cobalt concentration. Cobalt content was fairly consistent across groups in the various tissues at each time point in groups G3, G4, and G5 (**Figure 3.5D)**. Liver cobalt content on day 2 was similar for groups treated with EuCF-PCL particles (G3), EuCF-RPV particles (G4), or dual injection of EuCF-PCL and NRPV (G5) (1.08, 1.12, and 1.64 μg/g, respectively). The same was observed for spleen (0.90, 0.92, 1.17 μg/g) and lymph nodes (0.33, 0.35, and 0.51 μg/g). By day 5, cobalt content in the liver had dropped similarly in each group (10.3%, 21.8%, and 16.0%, respectively), but cobalt content in the spleen had increased (18.8%, 25.5% and 16.8%). Cobalt concentration in the lymph nodes remained consistent or increased slightly from day 2 to day 5 in all groups. After 28 days post injection of particles, the liver, spleen, and lymph nodes still retained a small amount of particles, but the majority had been cleared from tissues as evidenced by the much lower cobalt concentrations. However, the percentage of particles cleared was similar between groups for each tissue. For liver, cobalt concentrations decreased by 81.9%, 84.3%, and 86.5% from day 5 to day 28 for groups 3, 4, and 5, respectively. In the spleen, cobalt concentration dropped by 87.0%, 81.0%, and 82.6%. Lymph nodes also showed a significant decrease from day 5 to day 28 of 83.8%, 90.5%, and 79.6%.

3.3.3 Biodistribution Confirmations

We assessed the various result parameters (**Figure 3.7A)** by correlation analysis across groups to test the estimated predictive value for long-term biodistribution. Pearson's correlation coefficients for two parameter comparisons were averaged for RPV concentrations, cobalt concentrations, and SPECT/CT radioactivity measures in liver, spleen, and lymph nodes. Means of absolute "r" values with $p \leq 0.05$ were displayed in each cell and used to generate a heat map of relative strength of correlation (**Figure 3.7B**). Across all groups the strongest correlation (highest r value) was between cobalt concentration and RPV concentration in lymph node (r=0.93). Similarly, an absolute "r" value of 0.81 was obtained for between SPECT/CT signal in the lymph node and cobalt concentration in the lymph nodes. In the spleen, RPV concentration correlated with cobalt concentration with r = 0.54. For the liver, RPV concentration correlated with cobalt

concentration and gave an “r” value of 0.65. Also in the liver, SPECT/CT radioactivity and cobalt concentration correlated with an “r” value of 0.66. Lower Pearson correlation coefficients were recorded in liver than spleen and lymph nodes. However, such differences likely reflect tissue processing as whole lymph nodes and spleens were used for analysis while subregions of liver were analyzed. We also determined correlations between groups, tissues and test measures. Mean %ID/g from *ex vivo* gamma counts of ^{111}InEuCF-PCL (G7) in liver, spleen, and lymph node on days 2 and 5 exhibited a strong correlation with SPECT activity (r = 0.93) (**Figure 3.7C),** which validated the accuracy of our SPECT/CT quantification. Also the mean cobalt levels in

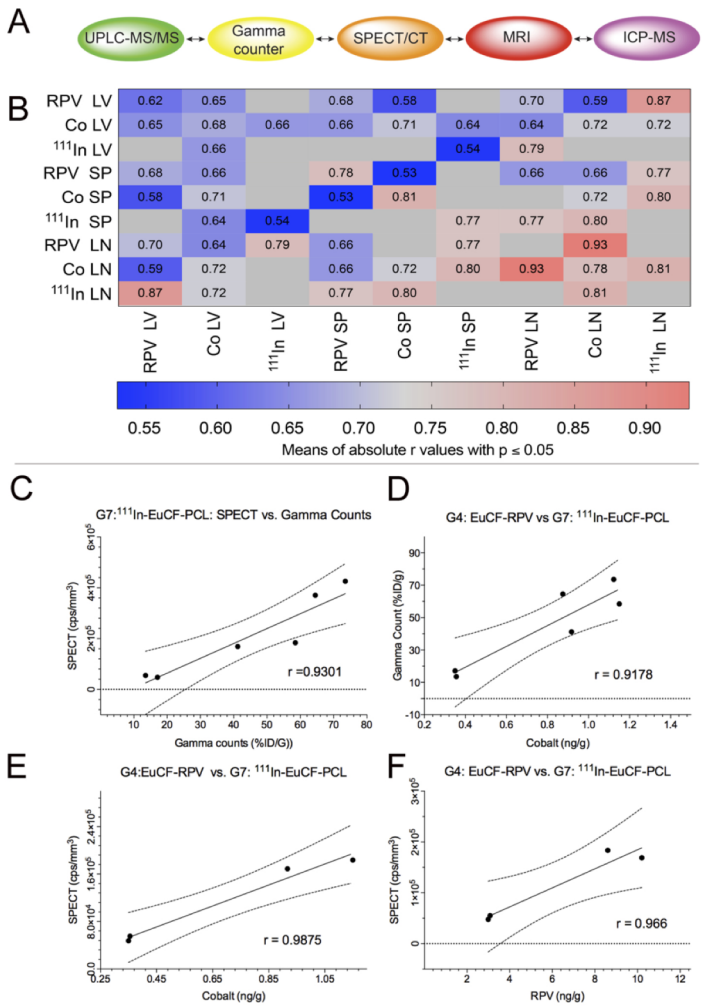

Figure 3.7 Coordination and correlation of metadata analysis. (A) Schematic showing parameters used for correlation analysis. **(B)** Correlation matrix. For each tissue (liver, spleen, lymph nodes) RPV, cobalt, or radioactivity (by SPECT/CT) content was summed across groups and then compared to each other. Shown are average correlation coefficients across treatment groups for correlations with a p-value ≤ 0.05. Pearson's correlation from days 2 and 5 between **(C)** ex vivo radioactivity (%ID/g) and in vivo SPECT/CT signal from liver, spleen, and lymph nodes; **(D)** cobalt content and ex vivo radio- activity (%ID/g) from liver, spleen and lymph nodes; **(E)** cobalt content and in vivo SPECT/CT signal quantitation in spleen and lymph nodes;**(F)** between in vivo drug content and SPECT/CT signal in spleen and lymph nodes;

liver, spleen, and lymph nodes from EuCF-RPV (G4) treated mice were strongly correlated to mean gamma scintillation counts from ^{111}InEuCF-PCL (G7) treated mice (r = 0.92) (**Figure 3.7D),** indicating that the amount of radioactivity in these samples positively correlates with cobalt concentration. We found that in spleen and lymph nodes on days 2 and 5 post-administration, mean cobalt concentrations in EuCF-RPV (G4) were strongly correlated with SPECT/CT radioactivity (r = 0.99) (**Figure 3.7E**)**.** Finally, for days 2 and 5 post-administration = in spleen and lymph nodes from mice treated with EuCF-RPV (G4), mean RPV concentrations were strongly with radioactivity measured by SPECT/CT signal (r = 0.96) (**Figure 3.7F**). These data, taken together, show that the amount of antiretroviral accumulation into reticuloendothelial organs can be estimated accurately using imaging data obtained from a multimodal theranostic platform.

3.3.4 Particle Trafficking in Mouse Tissue Macrophages

To determine cellular distribution of particles in tissues, following the MRI and SEPCT/CT scan animas was euthanized for collection of tissues. Tissues were fixed in TEM buffer, embedded in resin, and TEM analysis [179]. Representative TEM images of liver and spleen show macrophages in liver and spleen tissues from

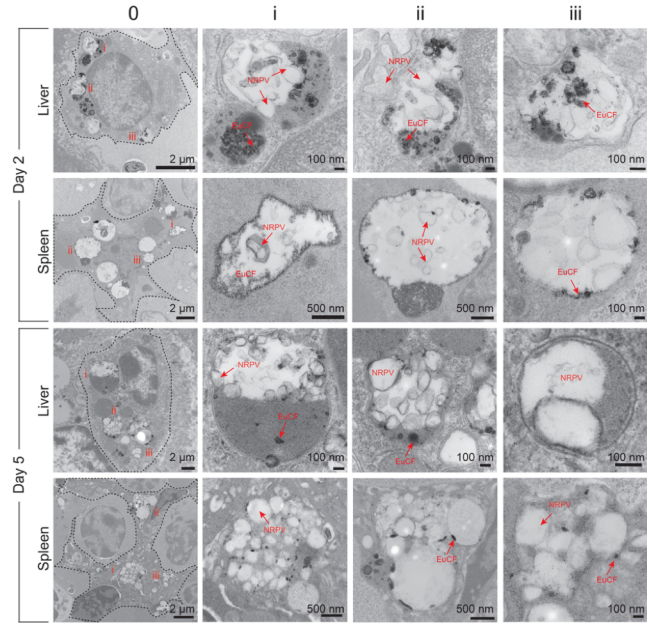

Figure 3.8 TEM of liver and spleen tissue sections. Column (0) shows representative images of tissue sections containing macrophages loaded with particles. **Columns (i-iii)** display magnified images of selected sections

day 2 and day 5 and are denoted by red roman numerals i, ii, and iii. (**Figure 3.8, column 0)** and are magnified (**columns I, ii, and iii, respectively**)**.** Moreover, large accumulations of light-colored NRPV crystals can be found alongside dark clusters of EuCF nanocrystals. Histological analyses showed normal tissue structure in particle-treated mice, thus ruling out the possibility of particle-associated pathological events at the microscopic level (**Figure 3.9)**. Together these data confirm that particles administered intravenously to mice were indeed sequestered by macrophages (TEM) in target organs without readily discernible evidence of pathology.

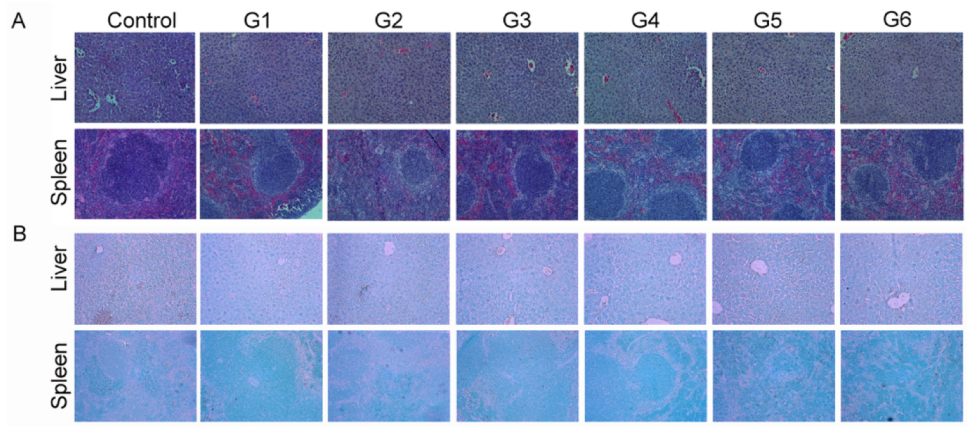

Figure 3.9 Histological assessments of tissues treated with particles. (A) Hematoxylin and eosin (H&E) staining of liver and spleen sections in treated mice. Livers and spleens from each treatment group (non-radioactive treatment groups) were excised at 28 days post injections. **(B)** TUNEL stains of liver and spleen sections of the same mice.

3.4 Discussion

Synthesized theranostic nanoparticles contain individual functional components that improve their diagnostic and therapeutic potential. *First*, the CF component enhances MRI signal sensitivity and specificity measures [196]. The images show excellent T2 relaxivity. As such, they can be readily used for ARV biodistribution studies. High relaxivity results in enhanced sensitivity for ferrite quantification. *Second*, the nanoparticle's unique spinel structure permits the incorporation, in a formed lattice, of rare earth elements. This includes, but is not limited to, neodymium, In^{3+}, Eu^{3+} and gadolinium [196]. *Third*, Eu^{3+} provides magnetic and fluorescence capabilities. *Fourth*, intrinsic doping of ^{111}In imparted SPECT/CT imaging capabilities, *Fifth* translational potential is realized through the nanoparticle's biocompatibility [196]. This is facilitated through the outer "soft" lipid layer of the ^{111}InEuCF-RPV nanoparticles [226, 278]. *Sixth*, the formed ^{111}InEuCF-RPV nanoparticles are highly stable and as such can be made for systemic use. *Seventh*, the ^{111}InEuCF-RPV nanoparticles are hydrophilic with a narrow size distribution. Each contains a "hard" inner matrix of an organic-inorganic hybrid of EuCF and PCL, which enables the nanoparticles to be loaded with hydrophobic ARVs and have limited to no toxicities. *Eighth*, the nanoparticles unique physicochemical properties facilitate entry into cells. Indeed, the core is made up of ^{111}InEuCF, PCL and RPV, while the outer lipid layers are formed with PC, DSPE-PEG2000 and DOPE. The lipid surrounding the ^{111}InEuCF-RPV core serves to facilitate rapid uptake by macrophages and as such effectively distribute drug into tissue viral reservoirs. *Ninth,* the nanoparticle's size and shape are comparable to that of LASER ART being developed for clinical use [153, 219].

In the present study we compared the pharmacokinetics and biodistribution of metal and drug to imaging data acquired from MRI and SPECT/CT modalities from plasma, liver, spleen and lymph nodes of NRPV, ^{111}InEuCF-PCL, and EuCF-RPV treated

Balb/cJ mice. The addition of the SPECT/CT modality to our already sensitive MRI particles was a significant improvement as it allowed for the visualization and quantification of particle accumulation in the axillary and popliteal lymph nodes which were not visible via MR imaging. Importantly, the SPECT/CT imaging data acquired within the first week after ^{111}InEuCF-PCL particle administration showed a very high Pearson's correlation with the coordinate tissue cobalt and RPV levels found in lymph nodes and spleens of mice treated with EuCF-RPV particles ($r = 0.9875$ and 0.966, respectively). The results demonstrated the potential of this platform to accurately screen the biodistribution of long-acting formulations in the reticuloendothelial system. However, several of the correlations made had moderate Pearson's correlation coefficients but were not statistically significant. The limitation, in part, reflects the particle biodistribution based on size. Indeed, our own ultra-small ^{177}LuEuCF particles localized primarily to the lung before a liver and spleen signal could be visualized. We believe this system can be accurately developed to closely match and improve upon the performance of our current and future LASER ART formulations. The creation of particles with increased aspect ratios is an area of active research and rod shaped particles may be advantageous for a cell and tissue based drug delivery system [279].

In addition to serving as a screening tool, these particles can facilitate drug penetrance into reservoir sites by a "Trojan horse" mechanism by creating drug depots [214]. The ability to deliver therapeutics to the exact subcellular site of HIV infection provides opportunities for disease prevention and treatment. Further optimization opens the possibility of combining multiple ARVs into a single particle, encapsulating CRISPR Cas9 for excision of integrated HIV DNA from tissue sites of latent infection [280] or delivering latency reversal agents like toll-like receptor (TLR) 7 agonists which were shown to be capable of reducing viral reservoirs in simian immunodeficiency virus-infected rhesus

macaques [281], while simultaneously imaging the real time ARV particle biodistribution and therapeutic efficacy.

In conclusion, the multimodal particles provide the basis for a flexible platform to rapidly assess tissue and cell drug biodistribution of long-acting ARVs by SPECT/CT and MRI in real time. Currently, plasma drug levels remain the gold standard for pharmacokinetics analysis, which is cumbersome for long-acting formulations. Importantly, the biocompatibility of these particles was confirmed and when loaded with ARVs they maintain therapeutic efficacy. Thus, these theranostic particles can accelerate the discovery of LASER ART and optimize therapeutic use profiles for an infected human viral host.

CHAPTER 4
Summary and Conclusion, Limitations, and Future Directions

4.1 Summary and conclusions

The successful development of combination antiretroviral therapy for the treatment of HIV-1 undoubtedly changed the course of human history, as millions of infected people can now anticipate a prolonged lifespan instead of a certain and painful death. However, the persistence of virus and the continued strain of the pandemic on global healthcare has resulted in HIV-1 research to develop novel strategies to improve upon current antiretroviral therapy. Improvements in pharmacodynamic and pharmacokinetic profiles have shown remarkable promise in increasing drug adherence, reducing secondary toxicities, and preventing new infections. Our laboratory has shown that the enhancement of the hydrophobicity of current ARVs via nanocrystals encased in biodegradable polymers allows for the establishment of drug depots within monocyte-macrophages, significantly prolonging drug half-life. But experimentation of such nanoformulations within animal models has proved cumbersome, with biodistribution measurements extending weeks or even months proving particularly tedious.

This study assessed the use of our theranostic nanoparticle platform and its ability to accumulate within monocyte-macrophages as well as reticuloendothelial tissues. Theranostic nanotechnology has allowed the rapid screening of drug tissue biodistribution and pharmacokinetics which allows for pharmacodynamic improvements. Our theranostic nanoparticle platform was developed with careful consideration of components that allowed assessment of particle presence as well as component concentration within cells and tissues in vitro, in vivo, and ex vivo. Encasement of hydrophobic ARVs and imaging contrast

agents within a single nanoformulation produced theranostic nanoparticles with a multitude of modalities, allowing for validations of the multiple measurements performed. Incorporation of Eu^{3+} into the nanoparticles allowed for confirmation of particle presence within cells and tissues via fluorescence confocal imaging. Cobalt ferrite provided a highly sensitive paramagnetic material necessary for T_2 contrast which allowed us to take advantage of the great spatial resolution provided by MRI. Intrinsic doping of the radioisotope, ^{111}inidum gave us the ability to accurately determine the concentration of particles *in vivo* by SPECT/CT imaging. SPECT/CT imaging is known for having greater sensitivity than MRI, but less spatial resolution. By combining both imaging modalities, we were able to create both a highly sensitive and specific probe. Altogether, our theranostic nanoparticle platform allowed for real time assessment of ARV biodistribution and activity that would otherwise not be possible with traditional plasma post-mortem tissue concentration analysis. If fully realized, these particles could be used pre-clinically to screen new drug candidates early in development. As a first step drug biodistribution and pharmacokinetic analysis, these particles would provide information about whether a therapy is reaching disease sites at a therapeutic concentration. This could speed drug development, bringing more effective medications to patients.

Upon synthesis, ^{111}InEuCF-RPV nanoparticles showed remarkably consistent size, magnetism, fluorescence, and proper ARV drug loading as well as drug release in PBS. Administration of InEuCF-RPV to *in vitro* macrophage cultures resulted in consistent cellular uptake of nanoparticles, showing

significantly higher uptake than NRPV. Uptake of InEuCF-RPV nanoparticles did not affect cellular viability in these studies. Furthermore, confocal microscopy of *in vitro* macrophages displayed InEuCF-RPV nanoparticles localizing within subcellular components, with a high proportion of nanoparticles residing within recycling endosomes. Perhaps most importantly, InEuCF-RPV nanoparticles exhibited antiretroviral activity (similar to NRPV) upon administration to HIV-1 infected in vitro cellular cultures, confirming the therapeutic effects of our theranostic nanoparticle platform. Real time *in vivo* MR and SPECT/CT imaging of mice administered ^{111}InEuCF-RPV nanoparticles via IV injection confirmed nanoparticle presence within reticuloendothelial tissues, including liver, spleen and axillary and inguinal lymph nodes up to 5 days post administration. Quantification of iron concentrations within liver and spleen was performed by MRI T_2 mapping. Post-mortem tissue concentrations of cobalt and RPV were measured by ICP-MS and UPLC- MS/MS, respectively. RPV and cobalt levels following injection of nanoparticles showed coordinate tissue and plasma drug and cobalt levels. Furthermore, quantification of SPECT/CT imaging data from the first 5 days post injection proved predictive of drug and cobalt concentrations up to 28 days post injection. Post-mortem tissue confocal microscopy confirmed the presence of InEuCF-RPV nanoparticle within recycling endosomal compartments in macrophages, mirroring results found in *in vitro* confocal microscopy studies.

Overall, such data suggests that the amount of drug that accumulates in tissues can be estimated in real time by *in vivo* MRI and SPECT/CT by using the known signal-to-drug ratio of ^{111}InEuCF-RPV nanoparticles. This imaging data can

then be used to predict drug pharmacokinetics and biodistribution up to 28 days post administration of particles which can greatly help and speed up the production and optimization of novel long-acting nanoformulations.

4.2 Limitations

A major limitation of our ^{111}InEuCF-RPV theranostic nanoparticle platform was that of drug loading. Indeed, the ability to load adequate amounts of drug into a nanoscale system while still containing the necessary contrast agents and fluorescent components is particularly challenging. ^{111}InEuCF-RPV nanoparticles exhibited a drug loading percentage of ~5.5% weight/weight; while such concentrations were adequate to exhibit antiretroviral activity *in vitro*, it is unlikely that such drug levels would have much of a therapeutic effect on HIV-1 replication *in vivo*. While this platform provided a good proof-of-concept that theranostic ARVs can predict future biodistribution, several of the correlations made had moderate Pearson's correlation coefficients, but were not statistically significant. The limitation, in part, reflects the particle biodistribution based on size. Indeed, our own ultra-small ^{177}LuEuCF particles localized primarily to the lung before a liver and spleen signal could be visualized. We believe this system can be accurately developed to closely match and improve upon the performance of our current and future LASER ART formulations. The creation of particles with increased aspect ratios is an area of active research and rod shaped particles may be advantageous for a cell and tissue based drug delivery system.

4.3 Future Directions

Potential future applications of HIV-1 theranostic technology are exciting and are rapidly expanding. Advancements in the fields of chemistry, molecular biology and engineering have facilitated the design, development, and implementation of numerous sophisticated theranostic nanosystems for a variety of diseases [282]. Additionally, theranostics is being applied to explore variability in therapeutic responses in patients adhering to different medications, vaccines, and lifestyles [283]. Despite its potential to drive the evolution of precise diagnostic and drug delivery agents at the molecular level, theranostic medicine is still in its infancy and optimal systems are yet to be developed. Further exploration of cellular dynamics, disease pathogenesis, biomaterials, genetic engineering, and the *in vivo* behavior of nanomaterials has the potential to uncover solutions to challenges drug delivery systems currently face.

In addition to the delivery of therapeutics, nanosystems are often employed for screening the biodistribution of long-acting nanoformulated drugs [179, 284]. This is of particular importance as the half-lives of each of the few existing long-acting drugs measure in weeks or even months and so would require extensive and cumbersome traditional pharmacokinetic testing [216, 220-223, 285]. In an effort to overcome this technical and biologic challenge, multimodal decorated nanoparticles have been produced in which hydrophobic ARVs and bioimaging agents are encased within a single nanoformulation. The bioimaging agents allow

for visualization by SPECT, PET, fluorescence, photoacoustic, MR imaging, or a combination thereof. This enables a sensitive, rapid and non-invasive measurement of drug location and concentration in the body. If realized, this would be a significant improvement over traditional biodistribution and pharmacokinetic assays that require animal sacrifice and end point organ removal.

Successful establishment of a theranostic nanoparticle platform would allow more advanced drug delivery and targeting schemes for HIV-1 eradication to be evaluated more efficiently. Experimentation that traditionally took months or years could be performed within weeks, allowing more time and resources to be put towards innovative nano-technological developments. Additionally, further refinement of theranostic nanoparticles is a tangible possibility for the future. Recently, we have begun experimenting with nanoparticles with increased aspect ratios, such as bismuth sulfur nanorods that have the same shape and size as nanoformulated ARVs. These particles have proven to provide better predictive power in terms of future BD and PK of nanoformulated drugs than older ARV nanoformulations, presumably due to their shape and surface characteristics more closely matching that of the delivered drugs.

Alterations in nanoparticle components and size could lead to specific targeting of other HIV-1 reservoirs, such as the brain or lymphoid systems. Many researchers are currently using a variety of targeting techniques to reach cells and tissues of interest. In the case of HIV infection, strategies that actively target therapeutics to anatomical and cellular reservoirs of latent infection could facilitate the eradication of HIV within a patient entirely. CD4 receptor-targeted

nanoparticles are designed to deliver therapeutics to T cells through surface functionalization with targeting molecules such as monoclonal antibodies (mAb), peptides, or aptamers and have been used in various diagnostic, therapeutic, and vaccine applications [286-293]. CD4+ T cells are the major target for HIV infection, and resting memory CD4+ T cells are considered the primary reservoir of latent HIV-1 provirus that is ineradicable by current anti-HIV therapy. Targeted delivery of antiretroviral drugs and latency-reversing agents to these CD4+ T cells may improve drug efficacy and minimize toxicity and off-target effects [294-296]. Although, conventional antibodies have been used to target nanoparticles, limitations such as immunogenicity and nonspecific uptake by the reticuloendothelial system may reduce effectiveness [297, 298].

An interesting and novel solution to these limitations would be use replication incompetent HIV envelope as a nanocarrier of therapeutics. From a biotechnological point of view, viruses are nature's own targeted delivery nanoparticles perfected by evolution and could bring improved solubility, pharmacokinetics, biodistribution, and designed specificity when compared with small molecule drugs. Viruses, structurally can be defined as a capsid, which is a shell of proteins and lipids that encloses genetic material needed to produce progeny virus in target cells transcriptional and translational machinery. Virus-like nanoparticles, however are produced from DNA plasmids containing only genes for the capsid proteins and lack genes for replication enzymes as integrase, reverse transcriptase, or polymerases. The result is a nanoparticle that targets the same cells and tissues as the original virus without creating an infection [299, 300].

Virus-like particles (VLPs), are rigid and firm structures that can be loaded with drug molecules in a confined nanosized spatial distribution [301]. These are well-defined protein based geometries at the atomic level with attractive self-assembly properties that are alterable by genetic manipulation. The capsid of viruses act as protein cages in which drugs can be loaded in a controlled manner and precisely delivered due to their ideal size for endocytosis.

In the context of a cure for HIV, it was recently reported that sequential treatment with LASER ART and CRISPR-Cas9 (targeted to the long terminal repeat region of the gag gene) demonstrated, for the first time, viral eradication in HIV infected, humanized mice [302]. Nested and digital-droplet PCR, as well as RNAscope tests were unable to detect virus in latent infectious viral reservoirs such as blood, lymphoid tissues, bone marrow and brain. In the study an adenovirus was used to deliver the CRISPR-Cas9 system, but such a delivery system has inherent limitations including target specificity and potential for immunogenicity. The ideal delivery vehicle for these treatments is yet to be realized, but in theory, an HIV-like nanoparticle, whose surface consists of HIV envelope glycoproteins (gp120 and gp41) present as trimers and whose core encases both LASER ART and CRISPR-Cas9 protein (with its associated RNA guide) would serve as the ideal HIV reservoir targeted therapy and could bring eradication of HIV to humans. Additionally, like other types of nanoparticles, VLPs can be designed for bioimaging techniques through incorporation of PET or SPECT radioisotopes, quantum dots, or MRI contrast agents to track particle

biodistribution and serve as confirmation of particle localization to anatomical and cellular targets.

In 1900, German Nobel laureate Paul Ehrlich envisioned a scientific concept he termed, “the magic bullet”. He envisioned that, just like a bullet fired from a gun to hit a specific target, there could be a way to specifically target invading microbes in the body without harming the body itself. Nanotechnology has the potential to bring magic bullet type cures to almost any disease and could usher in an era of personalized medicine where treatment and diagnosis are accomplished with single agents. The therapeutic index of drugs delivered via nanoparticles can be greatly enhanced as drug and imaging agents are brought directly to cells and tissues affected by disease. This allows for the sparing of healthy cells and reduced off-target toxicities. In the context of HIV, nanoparticles can increase the concentration of drug at anatomical sites that current orally administered drugs do not reach in therapeutic concentrations. The distribution of these platforms can be tracked non-invasively to ensure proper biodistribution of therapies. Overall, nanotechnology will continue to be a major driver of pharmacological advancements in healthcare in the foreseeable future.

REFERENCES

[1] G. Maartens, C. Celum, S.R. Lewin, HIV infection: epidemiology, pathogenesis, treatment, and prevention, Lancet 384(9939) (2014) 258-71.
[2] W.M. Bezabhe, L. Chalmers, L.R. Bereznicki, G.M. Peterson, M.A. Bimirew, D.M. Kassie, Barriers and facilitators of adherence to antiretroviral drug therapy and retention in care among adult HIV-positive patients: a qualitative study from Ethiopia, PLoS One 9(5) (2014) e97353.
[3] M. Fujita, [Study of molecular function of proteins in human immunodeficiency virus], Yakugaku Zasshi 133(10) (2013) 1103-11.
[4] C. Sprague, S.M. Brown, Local and Global HIV Aging Demographics and Research, Interdiscip Top Gerontol Geriatr 42 (2017) 1-10.
[5] P.A. Furman, J.A. Fyfe, M.H. St Clair, K. Weinhold, J.L. Rideout, G.A. Freeman, S.N. Lehrman, D.P. Bolognesi, S. Broder, H. Mitsuya, et al., Phosphorylation of 3'-azido-3'-deoxythymidine and selective interaction of the 5'-triphosphate with human immunodeficiency virus reverse transcriptase, Proc Natl Acad Sci U S A 83(21) (1986) 8333-7.
[6] M.H. St Clair, C.A. Richards, T. Spector, K.J. Weinhold, W.H. Miller, A.J. Langlois, P.A. Furman, 3'-Azido-3'-deoxythymidine triphosphate as an inhibitor and substrate of purified human immunodeficiency virus reverse transcriptase, Antimicrob Agents Chemother 31(12) (1987) 1972-7.
[7] R.B. Meeker, E. Asahchop, C. Power, The brain and HAART: collaborative and combative connections, Curr Opin HIV AIDS 9(6) (2014) 579-84.
[8] A.K. Pau, J.M. George, Antiretroviral therapy: current drugs, Infect Dis Clin North Am 28(3) (2014) 371-402.
[9] R.G. Lima, L. Moreira, J. Paes-Leme, V. Barreto-de-Souza, H.C. Castro-Faria-Neto, P.T. Bozza, D.C. Bou-Habib, Interaction of macrophages with apoptotic cells enhances HIV Type 1 replication through PGE2, PAF, and vitronectin receptor, AIDS Res Hum Retroviruses 22(8) (2006) 763-9.
[10] F. Porcheray, B. Samah, C. Leone, N. Dereuddre-Bosquet, G. Gras, Macrophage activation and human immunodeficiency virus infection: HIV replication directs macrophages towards a pro-inflammatory phenotype while previous activation modulates macrophage susceptibility to infection and viral production, Virology 349(1) (2006) 112-20.
[11] S.B. Lucas, A. Hounnou, C. Peacock, A. Beaumel, G. Djomand, J.M. N'Gbichi, K. Yeboue, M. Honde, M. Diomande, C. Giordano, et al., The mortality and pathology of HIV infection in a west African city, AIDS 7(12) (1993) 1569-79.
[12] E. Fanales-Belasio, M. Raimondo, B. Suligoi, S. Butto, HIV virology and pathogenetic mechanisms of infection: a brief overview, Ann Ist Super Sanita 46(1) (2010) 5-14.
[13] R.A. Weiss, P.R. Clapham, J.N. Weber, A.G. Dalgleish, L.A. Lasky, P.W. Berman, Variable and conserved neutralization antigens of human immunodeficiency virus, Nature 324(6097) (1986) 572-5.

[14] H.R. Gelderblom, M. Ozel, G. Pauli, Morphogenesis and morphology of HIV. Structure-function relations, Arch Virol 106(1-2) (1989) 1-13.
[15] M.S. Dahabieh, E. Battivelli, E. Verdin, Understanding HIV latency: the road to an HIV cure, Annu Rev Med 66 (2015) 407-21.
[16] D.R. Burton, R.A. Weiss, AIDS/HIV. A boost for HIV vaccine design, Science 329(5993) (2010) 770-3.
[17] A.B. Ward, I.A. Wilson, The HIV-1 envelope glycoprotein structure: nailing down a moving target, Immunol Rev 275(1) (2017) 21-32.
[18] E.O. Freed, HIV-1 replication, Somat Cell Mol Genet 26(1-6) (2001) 13-33.
[19] I. Frank, H. Stoiber, S. Godar, H. Stockinger, F. Steindl, H.W. Katinger, M.P. Dierich, Acquisition of host cell-surface-derived molecules by HIV-1, AIDS 10(14) (1996) 1611-20.
[20] A.G. Dalgleish, P.C. Beverley, P.R. Clapham, D.H. Crawford, M.F. Greaves, R.A. Weiss, The CD4 (T4) antigen is an essential component of the receptor for the AIDS retrovirus, Nature 312(5996) (1984) 763-7.
[21] D. Klatzmann, E. Champagne, S. Chamaret, J. Gruest, D. Guetard, T. Hercend, J.C. Gluckman, L. Montagnier, T-lymphocyte T4 molecule behaves as the receptor for human retrovirus LAV, Nature 312(5996) (1984) 767-8.
[22] L.B. Cohn, I.T. Silva, T.Y. Oliveira, R.A. Rosales, E.H. Parrish, G.H. Learn, B.H. Hahn, J.L. Czartoski, M.J. McElrath, C. Lehmann, F. Klein, M. Caskey, B.D. Walker, J.D. Siliciano, R.F. Siliciano, M. Jankovic, M.C. Nussenzweig, HIV-1 integration landscape during latent and active infection, Cell 160(3) (2015) 420-32.
[23] F. Maldarelli, X. Wu, L. Su, F.R. Simonetti, W. Shao, S. Hill, J. Spindler, A.L. Ferris, J.W. Mellors, M.F. Kearney, J.M. Coffin, S.H. Hughes, HIV latency. Specific HIV integration sites are linked to clonal expansion and persistence of infected cells, Science 345(6193) (2014) 179-83.
[24] C.M. Farnet, F.D. Bushman, HIV cDNA integration: molecular biology and inhibitor development, AIDS 10 Suppl A (1996) S3-11.
[25] K. Devadas, N.J. Hardegen, L.M. Wahl, I.K. Hewlett, K.A. Clouse, K.M. Yamada, S. Dhawan, Mechanisms for macrophage-mediated HIV-1 induction, J Immunol 173(11) (2004) 6735-44.
[26] B. Chen, Molecular Mechanism of HIV-1 Entry, Trends Microbiol 27(10) (2019) 878-891.
[27] A. Zhen, S.R. Krutzik, B.R. Levin, S. Kasparian, J.A. Zack, S.G. Kitchen, CD4 ligation on human blood monocytes triggers macrophage differentiation and enhances HIV infection, J Virol 88(17) (2014) 9934-46.
[28] R. Bosselut, CD4/CD8-lineage differentiation in the thymus: from nuclear effectors to membrane signals, Nat Rev Immunol 4(7) (2004) 529-40.
[29] D. Vremec, J. Pooley, H. Hochrein, L. Wu, K. Shortman, CD4 and CD8 expression by dendritic cell subtypes in mouse thymus and spleen, J Immunol 164(6) (2000) 2978-86.
[30] T.H. Rand, W.W. Cruikshank, D.M. Center, P.F. Weller, CD4-mediated stimulation of human eosinophils: lymphocyte chemoattractant factor and other CD4-binding ligands elicit eosinophil migration, J Exp Med 173(6) (1991) 1521-8.

[31] M.C. Miceli, J.R. Parnes, Role of CD4 and CD8 in T cell activation and differentiation, Adv Immunol 53 (1993) 59-122.
[32] N. Ray, R.W. Doms, HIV-1 coreceptors and their inhibitors, Curr Top Microbiol Immunol 303 (2006) 97-120.
[33] E.A. Berger, P.M. Murphy, J.M. Farber, Chemokine receptors as HIV-1 coreceptors: roles in viral entry, tropism, and disease, Annu Rev Immunol 17 (1999) 657-700.
[34] L. Cai, M. Gochin, K. Liu, Biochemistry and biophysics of HIV-1 gp41 - membrane interactions and implications for HIV-1 envelope protein mediated viral-cell fusion and fusion inhibitor design, Curr Top Med Chem 11(24) (2011) 2959-84.
[35] J.M. Coffin, H. Fan, The Discovery of Reverse Transcriptase, Annu Rev Virol 3(1) (2016) 29-51.
[36] R. Craigie, The molecular biology of HIV integrase, Future Virol 7(7) (2012) 679-686.
[37] R. Craigie, F.D. Bushman, HIV DNA integration, Cold Spring Harb Perspect Med 2(7) (2012) a006890.
[38] J. Vanhamel, A. Bruggemans, Z. Debyser, Establishment of latent HIV-1 reservoirs: what do we really know?, J Virus Erad 5(1) (2019) 3-9.
[39] A.P. Rice, The HIV-1 Tat Protein: Mechanism of Action and Target for HIV-1 Cure Strategies, Curr Pharm Des 23(28) (2017) 4098-4102.
[40] J. Karn, C.M. Stoltzfus, Transcriptional and posttranscriptional regulation of HIV-1 gene expression, Cold Spring Harb Perspect Med 2(2) (2012) a006916.
[41] C.A. Rosen, Tat and Rev: positive modulators of human immunodeficiency virus gene expression, Gene Expr 1(2) (1991) 85-90.
[42] K.T. Arrildt, S.B. Joseph, R. Swanstrom, The HIV-1 env protein: a coat of many colors, Curr HIV/AIDS Rep 9(1) (2012) 52-63.
[43] M. Hill, G. Tachedjian, J. Mak, The packaging and maturation of the HIV-1 Pol proteins, Curr HIV Res 3(1) (2005) 73-85.
[44] E.O. Freed, HIV-1 gag proteins: diverse functions in the virus life cycle, Virology 251(1) (1998) 1-15.
[45] H. Haim, I. Salas, J. Sodroski, Proteolytic processing of the human immunodeficiency virus envelope glycoprotein precursor decreases conformational flexibility, J Virol 87(3) (2013) 1884-9.
[46] W.I. Sundquist, H.G. Krausslich, HIV-1 assembly, budding, and maturation, Cold Spring Harb Perspect Med 2(7) (2012) a006924.
[47] J.H. Hurley, E. Boura, L.A. Carlson, B. Rozycki, Membrane budding, Cell 143(6) (2010) 875-87.
[48] J.M. Cuevas, R. Geller, R. Garijo, J. Lopez-Aldeguer, R. Sanjuan, Extremely High Mutation Rate of HIV-1 In Vivo, PLoS Biol 13(9) (2015) e1002251.
[49] S. Sierra, B. Kupfer, R. Kaiser, Basics of the virology of HIV-1 and its replication, J Clin Virol 34(4) (2005) 233-44.
[50] G.M. Shaw, E. Hunter, HIV transmission, Cold Spring Harb Perspect Med 2(11) (2012).

[51] D.W. Dickson, Multinucleated giant cells in acquired immunodeficiency syndrome encephalopathy. Origin from endogenous microglia?, Arch Pathol Lab Med 110(10) (1986) 967-8.
[52] L.R. Sharer, E.S. Cho, L.G. Epstein, Multinucleated giant cells and HTLV-III in AIDS encephalopathy, Hum Pathol 16(8) (1985) 760.
[53] H. Jiang, N. Xie, B. Cao, L. Tan, Y. Fan, F. Zhang, Z. Yao, L. Liu, S. Nie, Determinants of progression to AIDS and death following HIV diagnosis: a retrospective cohort study in Wuhan, China, PLoS One 8(12) (2013) e83078.
[54] A.S. Fauci, Multifactorial nature of human immunodeficiency virus disease: implications for therapy, Science 262(5136) (1993) 1011-8.
[55] T. Schacker, S. Little, E. Connick, K. Gebhard-Mitchell, Z.Q. Zhang, J. Krieger, J. Pryor, D. Havlir, J.K. Wong, D. Richman, L. Corey, A.T. Haase, Rapid accumulation of human immunodeficiency virus (HIV) in lymphatic tissue reservoirs during acute and early HIV infection: implications for timing of antiretroviral therapy, J Infect Dis 181(1) (2000) 354-7.
[56] G. Pantaleo, A.S. Fauci, Tracking HIV during disease progression, Curr Opin Immunol 6(4) (1994) 600-4.
[57] J.E. Schmitz, M.J. Kuroda, S. Santra, V.G. Sasseville, M.A. Simon, M.A. Lifton, P. Racz, K. Tenner-Racz, M. Dalesandro, B.J. Scallon, J. Ghrayeb, M.A. Forman, D.C. Montefiori, E.P. Rieber, N.L. Letvin, K.A. Reimann, Control of viremia in simian immunodeficiency virus infection by CD8+ lymphocytes, Science 283(5403) (1999) 857-60.
[58] A.T. Haase, Perils at mucosal front lines for HIV and SIV and their hosts, Nat Rev Immunol 5(10) (2005) 783-92.
[59] I. Pandrea, D.L. Sodora, G. Silvestri, C. Apetrei, Into the wild: simian immunodeficiency virus (SIV) infection in natural hosts, Trends Immunol 29(9) (2008) 419-28.
[60] D. Galati, M. Bocchino, New insights on the perturbations of T cell cycle during HIV infection, Curr Med Chem 14(18) (2007) 1920-4.
[61] R.I. Connor, H. Mohri, Y. Cao, D.D. Ho, Increased viral burden and cytopathicity correlate temporally with CD4+ T-lymphocyte decline and clinical progression in human immunodeficiency virus type 1-infected individuals, J Virol 67(4) (1993) 1772-7.
[62] C.M. Abreu, R.T. Veenhuis, C.R. Avalos, S. Graham, D.R. Parrilla, E.A. Ferreira, S.E. Queen, E.N. Shirk, B.T. Bullock, M. Li, K.A. Metcalf Pate, S.E. Beck, L.M. Mangus, J.L. Mankowski, F. Mac Gabhann, S.L. O'Connor, L. Gama, J.E. Clements, Myeloid and CD4 T Cells Comprise the Latent Reservoir in Antiretroviral Therapy-Suppressed SIVmac251-Infected Macaques, MBio 10(4) (2019).
[63] T.W. Chun, A.S. Fauci, HIV reservoirs: pathogenesis and obstacles to viral eradication and cure, AIDS 26(10) (2012) 1261-8.
[64] R.J. Pomerantz, Reservoirs of human immunodeficiency virus type 1: the main obstacles to viral eradication, Clin Infect Dis 34(1) (2002) 91-7.
[65] S. Castro-Gonzalez, M. Colomer-Lluch, R. Serra-Moreno, Barriers for HIV Cure: The Latent Reservoir, AIDS Res Hum Retroviruses 34(9) (2018) 739-759.

[66] M.C. Pitman, J.S.Y. Lau, J.H. McMahon, S.R. Lewin, Barriers and strategies to achieve a cure for HIV, Lancet HIV 5(6) (2018) e317-e328.
[67] J.M. Murray, J. Zaunders, S. Emery, D.A. Cooper, W.J. Hey-Nguyen, K.K. Koelsch, A.D. Kelleher, HIV dynamics linked to memory CD4+ T cell homeostasis, PLoS One 12(10) (2017) e0186101.
[68] A.D. Kashuba, J.R. Dyer, L.M. Kramer, R.H. Raasch, J.J. Eron, M.S. Cohen, Antiretroviral-drug concentrations in semen: implications for sexual transmission of human immunodeficiency virus type 1, Antimicrob Agents Chemother 43(8) (1999) 1817-26.
[69] P.L. Vernazza, Genital shedding of HIV-1 despite successful antiretroviral therapy, Lancet 358(9293) (2001) 1564.
[70] J.A. Politch, K.H. Mayer, D.J. Anderson, Depletion of CD4+ T cells in semen during HIV infection and their restoration following antiretroviral therapy, J Acquir Immune Defic Syndr 50(3) (2009) 283-9.
[71] M.L. Mzingwane, C.T. Tiemessen, Mechanisms of HIV persistence in HIV reservoirs, Rev Med Virol 27(2) (2017).
[72] L.J. Else, S. Taylor, D.J. Back, S.H. Khoo, Pharmacokinetics of antiretroviral drugs in anatomical sanctuary sites: the male and female genital tract, Antivir Ther 16(8) (2011) 1149-67.
[73] Z. Ahmed, T. Kawamura, S. Shimada, V. Piguet, The role of human dendritic cells in HIV-1 infection, J Invest Dermatol 135(5) (2015) 1225-1233.
[74] J. Hu, M.B. Gardner, C.J. Miller, Simian immunodeficiency virus rapidly penetrates the cervicovaginal mucosa after intravaginal inoculation and infects intraepithelial dendritic cells, J Virol 74(13) (2000) 6087-95.
[75] S.G. Turville, P.U. Cameron, A. Handley, G. Lin, S. Pohlmann, R.W. Doms, A.L. Cunningham, Diversity of receptors binding HIV on dendritic cell subsets, Nat Immunol 3(10) (2002) 975-83.
[76] T.B. Geijtenbeek, D.S. Kwon, R. Torensma, S.J. van Vliet, G.C. van Duijnhoven, J. Middel, I.L. Cornelissen, H.S. Nottet, V.N. KewalRamani, D.R. Littman, C.G. Figdor, Y. van Kooyk, DC-SIGN, a dendritic cell-specific HIV-1-binding protein that enhances trans-infection of T cells, Cell 100(5) (2000) 587-97.
[77] K. Barton, A. Winckelmann, S. Palmer, HIV-1 Reservoirs During Suppressive Therapy, Trends Microbiol 24(5) (2016) 345-355.
[78] M.K. Rothenberger, B.F. Keele, S.W. Wietgrefe, C.V. Fletcher, G.J. Beilman, J.G. Chipman, A. Khoruts, J.D. Estes, J. Anderson, S.P. Callisto, T.E. Schmidt, A. Thorkelson, C. Reilly, K. Perkey, T.G. Reimann, N.S. Utay, K. Nganou Makamdop, M. Stevenson, D.C. Douek, A.T. Haase, T.W. Schacker, Large number of rebounding/founder HIV variants emerge from multifocal infection in lymphatic tissues after treatment interruption, Proc Natl Acad Sci U S A 112(10) (2015) E1126-34.
[79] L.A. McNamara, J.A. Ganesh, K.L. Collins, Latent HIV-1 infection occurs in multiple subsets of hematopoietic progenitor cells and is reversed by NF-kappaB activation, J Virol 86(17) (2012) 9337-50.
[80] C.V. Fletcher, K. Staskus, S.W. Wietgrefe, M. Rothenberger, C. Reilly, J.G. Chipman, G.J. Beilman, A. Khoruts, A. Thorkelson, T.E. Schmidt, J. Anderson, K.

Perkey, M. Stevenson, A.S. Perelson, D.C. Douek, A.T. Haase, T.W. Schacker, Persistent HIV-1 replication is associated with lower antiretroviral drug concentrations in lymphatic tissues, Proc Natl Acad Sci U S A 111(6) (2014) 2307-12.
[81] A. Bandera, G. Ferrario, M. Saresella, I. Marventano, A. Soria, F. Zanini, F. Sabbatini, M. Airoldi, G. Marchetti, F. Franzetti, D. Trabattoni, M. Clerici, A. Gori, CD4+ T cell depletion, immune activation and increased production of regulatory T cells in the thymus of HIV-infected individuals, PLoS One 5(5) (2010) e10788.
[82] P.W. Denton, J.M. Long, S.W. Wietgrefe, C. Sykes, R.A. Spagnuolo, O.D. Snyder, K. Perkey, N.M. Archin, S.K. Choudhary, K. Yang, M.G. Hudgens, I. Pastan, A.T. Haase, A.D. Kashuba, E.A. Berger, D.M. Margolis, J.V. Garcia, Targeted cytotoxic therapy kills persisting HIV infected cells during ART, PLoS Pathog 10(1) (2014) e1003872.
[83] D. Brown, J.J. Mattapallil, Gastrointestinal tract and the mucosal macrophage reservoir in HIV infection, Clin Vaccine Immunol 21(11) (2014) 1469-73.
[84] A. Iwasaki, Mucosal dendritic cells, Annu Rev Immunol 25 (2007) 381-418.
[85] T.W. Chun, D.C. Nickle, J.S. Justement, J.H. Meyers, G. Roby, C.W. Hallahan, S. Kottilil, S. Moir, J.M. Mican, J.I. Mullins, D.J. Ward, J.A. Kovacs, P.J. Mannon, A.S. Fauci, Persistence of HIV in gut-associated lymphoid tissue despite long-term antiretroviral therapy, J Infect Dis 197(5) (2008) 714-20.
[86] A. Kok, L. Hocqueloux, H. Hocini, M. Carriere, L. Lefrou, A. Guguin, P. Tisserand, H. Bonnabau, V. Avettand-Fenoel, T. Prazuck, S. Katsahian, P. Gaulard, R. Thiebaut, Y. Levy, S. Hue, Early initiation of combined antiretroviral therapy preserves immune function in the gut of HIV-infected patients, Mucosal Immunol 8(1) (2015) 127-40.
[87] M. Guadalupe, E. Reay, S. Sankaran, T. Prindiville, J. Flamm, A. McNeil, S. Dandekar, Severe CD4+ T-cell depletion in gut lymphoid tissue during primary human immunodeficiency virus type 1 infection and substantial delay in restoration following highly active antiretroviral therapy, J Virol 77(21) (2003) 11708-17.
[88] M. Cavarelli, G. Scarlatti, HIV-1 infection: the role of the gastrointestinal tract, Am J Reprod Immunol 71(6) (2014) 537-42.
[89] C.K. Petito, B. Roberts, J.D. Cantando, A. Rabinstein, R. Duncan, Hippocampal injury and alterations in neuronal chemokine co-receptor expression in patients with AIDS, J Neuropathol Exp Neurol 60(4) (2001) 377-85.
[90] M. Kaul, G.A. Garden, S.A. Lipton, Pathways to neuronal injury and apoptosis in HIV-associated dementia, Nature 410(6831) (2001) 988-94.
[91] P.R. Clapham, A. McKnight, HIV-1 receptors and cell tropism, Br Med Bull 58 (2001) 43-59.
[92] Y. Liu, H. Liu, B.O. Kim, V.H. Gattone, J. Li, A. Nath, J. Blum, J.J. He, CD4-independent infection of astrocytes by human immunodeficiency virus type 1: requirement for the human mannose receptor, J Virol 78(8) (2004) 4120-33.
[93] V. Dahl, M. Gisslen, L. Hagberg, J. Peterson, W. Shao, S. Spudich, R.W. Price, S. Palmer, An example of genetically distinct HIV type 1 variants in

cerebrospinal fluid and plasma during suppressive therapy, J Infect Dis 209(10) (2014) 1618-22.
[94] M.M. Bednar, C.B. Sturdevant, L.A. Tompkins, K.T. Arrildt, E. Dukhovlinova, L.P. Kincer, R. Swanstrom, Compartmentalization, Viral Evolution, and Viral Latency of HIV in the CNS, Curr HIV/AIDS Rep 12(2) (2015) 262-71.
[95] A. Canestri, F.X. Lescure, S. Jaureguiberry, A. Moulignier, C. Amiel, A.G. Marcelin, G. Peytavin, R. Tubiana, G. Pialoux, C. Katlama, Discordance between cerebral spinal fluid and plasma HIV replication in patients with neurological symptoms who are receiving suppressive antiretroviral therapy, Clin Infect Dis 50(5) (2010) 773-8.
[96] B.M. Best, S.L. Letendre, P. Koopmans, S.S. Rossi, D.B. Clifford, A.C. Collier, B.B. Gelman, C.M. Marra, J.C. McArthur, J.A. McCutchan, S. Morgello, D.M. Simpson, E.V. Capparelli, R.J. Ellis, I. Grant, C.S. Group, Low cerebrospinal fluid concentrations of the nucleotide HIV reverse transcriptase inhibitor, tenofovir, J Acquir Immune Defic Syndr 59(4) (2012) 376-81.
[97] B.M. Best, S.L. Letendre, E. Brigid, D.B. Clifford, A.C. Collier, B.B. Gelman, J.C. McArthur, J.A. McCutchan, D.M. Simpson, R. Ellis, E.V. Capparelli, I. Grant, C. Group, Low atazanavir concentrations in cerebrospinal fluid, AIDS 23(1) (2009) 83-7.
[98] M. Smurzynski, K. Wu, S. Letendre, K. Robertson, R.J. Bosch, D.B. Clifford, S. Evans, A.C. Collier, M. Taylor, R. Ellis, Effects of central nervous system antiretroviral penetration on cognitive functioning in the ALLRT cohort, AIDS 25(3) (2011) 357-65.
[99] K. Patel, X. Ming, P.L. Williams, K.R. Robertson, J.M. Oleske, G.R. Seage, 3rd, A.C.T.C.S.T. International Maternal Pediatric Adolescent, Impact of HAART and CNS-penetrating antiretroviral regimens on HIV encephalopathy among perinatally infected children and adolescents, AIDS 23(14) (2009) 1893-901.
[100] N. Chomont, M. El-Far, P. Ancuta, L. Trautmann, F.A. Procopio, B. Yassine-Diab, G. Boucher, M.R. Boulassel, G. Ghattas, J.M. Brenchley, T.W. Schacker, B.J. Hill, D.C. Douek, J.P. Routy, E.K. Haddad, R.P. Sekaly, HIV reservoir size and persistence are driven by T cell survival and homeostatic proliferation, Nat Med 15(8) (2009) 893-900.
[101] T. Pierson, T.L. Hoffman, J. Blankson, D. Finzi, K. Chadwick, J.B. Margolick, C. Buck, J.D. Siliciano, R.W. Doms, R.F. Siliciano, Characterization of chemokine receptor utilization of viruses in the latent reservoir for human immunodeficiency virus type 1, J Virol 74(17) (2000) 7824-33.
[102] M. Arainga, B. Edagwa, R.L. Mosley, L.Y. Poluektova, S. Gorantla, H.E. Gendelman, A mature macrophage is a principal HIV-1 cellular reservoir in humanized mice after treatment with long acting antiretroviral therapy, Retrovirology 14(1) (2017) 17.
[103] S. Jorajuria, N. Dereuddre-Bosquet, F. Becher, S. Martin, F. Porcheray, A. Garrigues, A. Mabondzo, H. Benech, J. Grassi, S. Orlowski, D. Dormont, P. Clayette, ATP binding cassette multidrug transporters limit the anti-HIV activity of zidovudine and indinavir in infected human macrophages, Antivir Ther 9(4) (2004) 519-28.

[104] C. Gavegnano, R.F. Schinazi, Antiretroviral therapy in macrophages: implication for HIV eradication, Antivir Chem Chemother 20(2) (2009) 63-78.
[105] B.F. Keele, L. Tazi, S. Gartner, Y. Liu, T.B. Burgon, J.D. Estes, T.C. Thacker, K.A. Crandall, J.C. McArthur, G.F. Burton, Characterization of the follicular dendritic cell reservoir of human immunodeficiency virus type 1, J Virol 82(11) (2008) 5548-61.
[106] C.C. Carter, A. Onafuwa-Nuga, L.A. McNamara, J.t. Riddell, D. Bixby, M.R. Savona, K.L. Collins, HIV-1 infects multipotent progenitor cells causing cell death and establishing latent cellular reservoirs, Nat Med 16(4) (2010) 446-51.
[107] A. Alexaki, B. Wigdahl, HIV-1 infection of bone marrow hematopoietic progenitor cells and their role in trafficking and viral dissemination, PLoS Pathog 4(12) (2008) e1000215.
[108] N. Bannert, M. Farzan, D.S. Friend, H. Ochi, K.S. Price, J. Sodroski, J.A. Boyce, Human Mast cell progenitors can be infected by macrophagetropic human immunodeficiency virus type 1 and retain virus with maturation in vitro, J Virol 75(22) (2001) 10808-14.
[109] K.A. Thompson, C.L. Cherry, J.E. Bell, C.A. McLean, Brain cell reservoirs of latent virus in presymptomatic HIV-infected individuals, Am J Pathol 179(4) (2011) 1623-9.
[110] L.J. Lawson, V.H. Perry, S. Gordon, Turnover of resident microglia in the normal adult mouse brain, Neuroscience 48(2) (1992) 405-15.
[111] A. Nath, J.E. Clements, Eradication of HIV from the brain: reasons for pause, AIDS 25(5) (2011) 577-80.
[112] M.A. Fischl, R.M. Olson, S.E. Follansbee, J.P. Lalezari, D.H. Henry, P.T. Frame, S.C. Remick, M.P. Salgo, A.H. Lin, C. Nauss-Karol, J. Lieberman, W. Soo, Zalcitabine compared with zidovudine in patients with advanced HIV-1 infection who received previous zidovudine therapy, Ann Intern Med 118(10) (1993) 762-9.
[113] J.D. Lundgren, A.N. Phillips, C. Pedersen, N. Clumeck, J.M. Gatell, A.M. Johnson, B. Ledergerber, S. Vella, J.O. Nielsen, Comparison of long-term prognosis of patients with AIDS treated and not treated with zidovudine. AIDS in Europe Study Group, JAMA 271(14) (1994) 1088-92.
[114] S.M. Hammer, D.A. Katzenstein, M.D. Hughes, H. Gundacker, R.T. Schooley, R.H. Haubrich, W.K. Henry, M.M. Lederman, J.P. Phair, M. Niu, M.S. Hirsch, T.C. Merigan, A trial comparing nucleoside monotherapy with combination therapy in HIV-infected adults with CD4 cell counts from 200 to 500 per cubic millimeter. AIDS Clinical Trials Group Study 175 Study Team, N Engl J Med 335(15) (1996) 1081-90.
[115] S. Vella, B. Schwartlander, S.P. Sow, S.P. Eholie, R.L. Murphy, The history of antiretroviral therapy and of its implementation in resource-limited areas of the world, AIDS 26(10) (2012) 1231-41.
[116] G. Skowron, S.A. Bozzette, L. Lim, C.B. Pettinelli, H.H. Schaumburg, J. Arezzo, M.A. Fischl, W.G. Powderly, D.J. Gocke, D.D. Richman, J.C. Pottage, D. Antoniskis, G.F. McKinley, N.E. Hyslop, G. Ray, G. Simon, N. Reed, M.L. LoFaro, R.B. Uttamchandani, L.D. Gelb, S.J. Sperber, R.L. Murphy, J.M. Leedom, M.H. Grieco, J. Zachary, M.S. Hirsch, S.A. Spector, J. Bigley, W. Soo,

T.C. Merigan, Alternating and intermittent regimens of zidovudine and dideoxycytidine in patients with AIDS or AIDS-related complex, Ann Intern Med 118(5) (1993) 321-30.
[117] D.R. Kuritzkes, I. Marschner, V.A. Johnson, R. Bassett, J.J. Eron, M.A. Fischl, R.L. Murphy, K. Fife, J. Maenza, M.E. Rosandich, D. Bell, K. Wood, J.P. Sommadossi, C. Pettinelli, Lamivudine in combination with zidovudine, stavudine, or didanosine in patients with HIV-1 infection. A randomized, double-blind, placebo-controlled trial. National Institute of Allergy and Infectious Disease AIDS Clinical Trials Group Protocol 306 Investigators, AIDS 13(6) (1999) 685-94.
[118] D.W. Cameron, A.J. Japour, Y. Xu, A. Hsu, J. Mellors, C. Farthing, C. Cohen, D. Poretz, M. Markowitz, S. Follansbee, J.B. Angel, D. McMahon, D. Ho, V. Devanarayan, R. Rode, M. Salgo, D.J. Kempf, R. Granneman, J.M. Leonard, E. Sun, Ritonavir and saquinavir combination therapy for the treatment of HIV infection, AIDS 13(2) (1999) 213-24.
[119] J.S. Montaner, P. Reiss, D. Cooper, S. Vella, M. Harris, B. Conway, M.A. Wainberg, D. Smith, P. Robinson, D. Hall, M. Myers, J.M. Lange, A randomized, double-blind trial comparing combinations of nevirapine, didanosine, and zidovudine for HIV-infected patients: the INCAS Trial. Italy, The Netherlands, Canada and Australia Study, JAMA 279(12) (1998) 930-7.
[120] S.H. Michaels, R. Clark, P. Kissinger, Declining morbidity and mortality among patients with advanced human immunodeficiency virus infection, N Engl J Med 339(6) (1998) 405-6.
[121] M.A. Polis, I.A. Sidorov, C. Yoder, S. Jankelevich, J. Metcalf, B.U. Mueller, M.A. Dimitrov, P. Pizzo, R. Yarchoan, D.S. Dimitrov, Correlation between reduction in plasma HIV-1 RNA concentration 1 week after start of antiretroviral treatment and longer-term efficacy, Lancet 358(9295) (2001) 1760-5.
[122] A.D. Holec, S. Mandal, P.K. Prathipati, C.J. Destache, Nucleotide Reverse Transcriptase Inhibitors: A Thorough Review, Present Status and Future Perspective as HIV Therapeutics, Curr HIV Res 15(6) (2017) 411-421.
[123] T. Antoniou, L.Y. Park-Wyllie, A.L. Tseng, Tenofovir: a nucleotide analog for the management of human immunodeficiency virus infection, Pharmacotherapy 23(1) (2003) 29-43.
[124] H.B. Fung, E.A. Stone, F.J. Piacenti, Tenofovir disoproxil fumarate: a nucleotide reverse transcriptase inhibitor for the treatment of HIV infection, Clin Ther 24(10) (2002) 1515-48.
[125] P. Zhan, X. Chen, D. Li, Z. Fang, E. De Clercq, X. Liu, HIV-1 NNRTIs: structural diversity, pharmacophore similarity, and implications for drug design, Med Res Rev 33 Suppl 1 (2013) E1-72.
[126] M.P. de Bethune, Non-nucleoside reverse transcriptase inhibitors (NNRTIs), their discovery, development, and use in the treatment of HIV-1 infection: a review of the last 20 years (1989-2009), Antiviral Res 85(1) (2010) 75-90.
[127] P. Zhan, X. Liu, Z. Li, C. Pannecouque, E. De Clercq, Design strategies of novel NNRTIs to overcome drug resistance, Curr Med Chem 16(29) (2009) 3903-17.

[128] P. Dellamonica, G. Di Perri, R. Garraffo, NNRTIs: pharmacological data, Med Mal Infect 42(7) (2012) 287-95.
[129] E. De Clercq, Non-nucleoside reverse transcriptase inhibitors (NNRTIs): past, present, and future, Chem Biodivers 1(1) (2004) 44-64.
[130] A.M. Wensing, N.M. van Maarseveen, M. Nijhuis, Fifteen years of HIV Protease Inhibitors: raising the barrier to resistance, Antiviral Res 85(1) (2010) 59-74.
[131] S.A. Rabi, G.M. Laird, C.M. Durand, S. Laskey, L. Shan, J.R. Bailey, S. Chioma, R.D. Moore, R.F. Siliciano, Multi-step inhibition explains HIV-1 protease inhibitor pharmacodynamics and resistance, J Clin Invest 123(9) (2013) 3848-60.
[132] A.K. Ghosh, H.L. Osswald, G. Prato, Recent Progress in the Development of HIV-1 Protease Inhibitors for the Treatment of HIV/AIDS, J Med Chem 59(11) (2016) 5172-208.
[133] E. Lefebvre, C.A. Schiffer, Resilience to resistance of HIV-1 protease inhibitors: profile of darunavir, AIDS Rev 10(3) (2008) 131-42.
[134] D.R. Kuritzkes, HIV-1 entry inhibitors: an overview, Curr Opin HIV AIDS 4(2) (2009) 82-7.
[135] R.L. Bettiker, D.E. Koren, J.M. Jacobson, Ibalizumab, Curr Opin HIV AIDS 13(4) (2018) 354-358.
[136] C.T. Wild, D.C. Shugars, T.K. Greenwell, C.B. McDanal, T.J. Matthews, Peptides corresponding to a predictive alpha-helical domain of human immunodeficiency virus type 1 gp41 are potent inhibitors of virus infection, Proc Natl Acad Sci U S A 91(21) (1994) 9770-4.
[137] P. Dorr, M. Westby, S. Dobbs, P. Griffin, B. Irvine, M. Macartney, J. Mori, G. Rickett, C. Smith-Burchnell, C. Napier, R. Webster, D. Armour, D. Price, B. Stammen, A. Wood, M. Perros, Maraviroc (UK-427,857), a potent, orally bioavailable, and selective small-molecule inhibitor of chemokine receptor CCR5 with broad-spectrum anti-human immunodeficiency virus type 1 activity, Antimicrob Agents Chemother 49(11) (2005) 4721-32.
[138] S.A. Iacob, D.G. Iacob, Ibalizumab Targeting CD4 Receptors, An Emerging Molecule in HIV Therapy, Front Microbiol 8 (2017) 2323.
[139] B. Emu, J. Fessel, S. Schrader, P. Kumar, G. Richmond, S. Win, S. Weinheimer, C. Marsolais, S. Lewis, Phase 3 Study of Ibalizumab for Multidrug-Resistant HIV-1, N Engl J Med 379(7) (2018) 645-654.
[140] M. Chen, C. Shi, V. Kalia, S.B. Tencza, R.C. Montelaro, P. Gupta, HIV gp120 V(1)/V(2) and C(2)-V(3) domains glycoprotein compatibility is required for viral replication, Virus Res 79(1-2) (2001) 91-101.
[141] S. Nakane, A. Iwamoto, Z. Matsuda, The V4 and V5 Variable Loops of HIV-1 Envelope Glycoprotein Are Tolerant to Insertion of Green Fluorescent Protein and Are Useful Targets for Labeling, J Biol Chem 290(24) (2015) 15279-91.
[142] M.V. Beccari, B.T. Mogle, E.F. Sidman, K.A. Mastro, E. Asiago-Reddy, W.D. Kufel, Ibalizumab, a Novel Monoclonal Antibody for the Management of Multidrug-Resistant HIV-1 Infection, Antimicrob Agents Chemother 63(6) (2019).
[143] A. Markham, Ibalizumab: First Global Approval, Drugs 78(7) (2018) 781-785.

[144] I. Malet, V. Calvez, A.G. Marcelin, The future of integrase inhibitors of HIV-1, Curr Opin Virol 2(5) (2012) 580-7.
[145] M. Metifiot, C. Marchand, Y. Pommier, HIV integrase inhibitors: 20-year landmark and challenges, Adv Pharmacol 67 (2013) 75-105.
[146] W.G. Powderly, Integrase inhibitors in the treatment of HIV-1 infection, J Antimicrob Chemother 65(12) (2010) 2485-8.
[147] G. Di Perri, A. Calcagno, A. Trentalange, S. Bonora, The clinical pharmacology of integrase inhibitors, Expert Rev Clin Pharmacol 12(1) (2019) 31-44.
[148] F.J. Palella, Jr., R.K. Baker, A.C. Moorman, J.S. Chmiel, K.C. Wood, J.T. Brooks, S.D. Holmberg, H.I.V.O.S. Investigators, Mortality in the highly active antiretroviral therapy era: changing causes of death and disease in the HIV outpatient study, J Acquir Immune Defic Syndr 43(1) (2006) 27-34.
[149] J.R. Castillo-Mancilla, J.E. Haberer, Adherence Measurements in HIV: New Advancements in Pharmacologic Methods and Real-Time Monitoring, Curr HIV/AIDS Rep 15(1) (2018) 49-59.
[150] D.A. Margolis, J. Gonzalez-Garcia, H.J. Stellbrink, J.J. Eron, Y. Yazdanpanah, D. Podzamczer, T. Lutz, J.B. Angel, G.J. Richmond, B. Clotet, F. Gutierrez, L. Sloan, M.S. Clair, M. Murray, S.L. Ford, J. Mrus, P. Patel, H. Crauwels, S.K. Griffith, K.C. Sutton, D. Dorey, K.Y. Smith, P.E. Williams, W.R. Spreen, Long-acting intramuscular cabotegravir and rilpivirine in adults with HIV-1 infection (LATTE-2): 96-week results of a randomised, open-label, phase 2b, non-inferiority trial, Lancet 390(10101) (2017) 1499-1510.
[151] B. Sillman, A.N. Bade, P.K. Dash, B. Bhargavan, T. Kocher, S. Mathews, H. Su, G.D. Kanmogne, L.Y. Poluektova, S. Gorantla, J. McMillan, N. Gautam, Y. Alnouti, B. Edagwa, H.E. Gendelman, Creation of a long-acting nanoformulated dolutegravir, Nat Commun 9(1) (2018) 443.
[152] A.N. Nyaku, S.G. Kelly, B.O. Taiwo, Long-Acting Antiretrovirals: Where Are We now?, Curr HIV/AIDS Rep 14(2) (2017) 63-71.
[153] D. Guo, T. Zhou, M. Arainga, D. Palandri, N. Gautam, T. Bronich, Y. Alnouti, J. McMillan, B. Edagwa, H.E. Gendelman, Creation of a Long-Acting Nanoformulated 2',3'-Dideoxy-3'-Thiacytidine, J Acquir Immune Defic Syndr 74(3) (2017) e75-e83.
[154] B. Edagwa, J. McMillan, B. Sillman, H.E. Gendelman, Long-acting slow effective release antiretroviral therapy, Expert Opin Drug Deliv 14(11) (2017) 1281-1291.
[155] D.A. Margolis, J. Gonzalez-Garcia, H.-J. Stellbrink, J.J. Eron, Y. Yazdanpanah, D. Podzamczer, T. Lutz, J.B. Angel, G.J. Richmond, B. Clotet, F. Gutierrez, L. Sloan, M.S. Clair, M. Murray, S.L. Ford, J. Mrus, P. Patel, H. Crauwels, S.K. Griffith, K.C. Sutton, D. Dorey, K.Y. Smith, P.E. Williams, W.R. Spreen, Long-acting intramuscular cabotegravir and rilpivirine in adults with HIV-1 infection (LATTE-2): 96-week results of a randomised, open-label, phase 2b, non-inferiority trial, The Lancet 390(10101) (2017) 1499-1510.
[156] M. Markowitz, I. Frank, R.M. Grant, K.H. Mayer, R. Elion, D. Goldstein, C. Fisher, M.E. Sobieszczyk, J.E. Gallant, H. Van Tieu, W. Weinberg, D.A. Margolis, K.J. Hudson, B.S. Stancil, S.L. Ford, P. Patel, E. Gould, A.R. Rinehart, K.Y.

Smith, W.R. Spreen, Safety and tolerability of long-acting cabotegravir injections in HIV-uninfected men (ECLAIR): a multicentre, double-blind, randomised, placebo-controlled, phase 2a trial, Lancet HIV 4(8) (2017) e331-e340.
[157] M.A. Boyd, D.A. Cooper, Long-acting injectable ART: next revolution in HIV?, Lancet 390(10101) (2017) 1468-1470.
[158] H.E. Gendelman, J. McMillan, A.N. Bade, B. Edagwa, B.D. Kevadiya, The Promise of Long-Acting Antiretroviral Therapies: From Need to Manufacture, Trends Microbiol 27(7) (2019) 593-606.
[159] J. Rautio, N.A. Meanwell, L. Di, M.J. Hageman, The expanding role of prodrugs in contemporary drug design and development, Nat Rev Drug Discov 17(8) (2018) 559-587.
[160] K.M. Huttunen, J. Rautio, Prodrugs - an efficient way to breach delivery and targeting barriers, Curr Top Med Chem 11(18) (2011) 2265-87.
[161] J. Rautio, H. Kumpulainen, T. Heimbach, R. Oliyai, D. Oh, T. Jarvinen, J. Savolainen, Prodrugs: design and clinical applications, Nat Rev Drug Discov 7(3) (2008) 255-70.
[162] J. McMillan, A. Szlachetka, L. Slack, B. Sillman, B. Lamberty, B. Morsey, S. Callen, N. Gautam, Y. Alnouti, B. Edagwa, H.E. Gendelman, H.S. Fox, Pharmacokinetics of a Long-Acting Nanoformulated Dolutegravir Prodrug in Rhesus Macaques, Antimicrob Agents Chemother 62(1) (2018).
[163] J.C. Kraft, L.A. McConnachie, J. Koehn, L. Kinman, J. Sun, A.C. Collier, C. Collins, D.D. Shen, R.J.Y. Ho, Mechanism-based pharmacokinetic (MBPK) models describe the complex plasma kinetics of three antiretrovirals delivered by a long-acting anti-HIV drug combination nanoparticle formulation, J Control Release 275 (2018) 229-241.
[164] M.T. McKenna, J.A. Weis, V. Quaranta, T.E. Yankeelov, Leveraging Mathematical Modeling to Quantify Pharmacokinetic and Pharmacodynamic Pathways: Equivalent Dose Metric, Front Physiol 10 (2019) 616.
[165] C. Bon, P.L. Toutain, D. Concordet, R. Gehring, T. Martin-Jimenez, J. Smith, L. Pelligand, M. Martinez, T. Whittem, J.E. Riviere, J.P. Mochel, Mathematical modeling and simulation in animal health. Part III: Using nonlinear mixed-effects to characterize and quantify variability in drug pharmacokinetics, J Vet Pharmacol Ther 41(2) (2018) 171-183.
[166] Z. Lin, R. Gehring, J.P. Mochel, T. Lave, J.E. Riviere, Mathematical modeling and simulation in animal health - Part II: principles, methods, applications, and value of physiologically based pharmacokinetic modeling in veterinary medicine and food safety assessment, J Vet Pharmacol Ther 39(5) (2016) 421-38.
[167] J.E. Riviere, J. Gabrielsson, M. Fink, J. Mochel, Mathematical modeling and simulation in animal health. Part I: Moving beyond pharmacokinetics, J Vet Pharmacol Ther 39(3) (2016) 213-23.
[168] M. Durisova, L. Dedik, New mathematical methods in pharmacokinetic modeling, Basic Clin Pharmacol Toxicol 96(5) (2005) 335-42.
[169] R.K. Rajoli, D.J. Back, S. Rannard, C.L. Freel Meyers, C. Flexner, A. Owen, M. Siccardi, Physiologically Based Pharmacokinetic Modelling to Inform

Development of Intramuscular Long-Acting Nanoformulations for HIV, Clin Pharmacokinet 54(6) (2015) 639-50.
[170] A.G. Jackson, L.J. Else, P.M. Mesquita, D. Egan, D.J. Back, Z. Karolia, L. Ringner-Nackter, C.J. Higgs, B.C. Herold, B.G. Gazzard, M. Boffito, A compartmental pharmacokinetic evaluation of long-acting rilpivirine in HIV-negative volunteers for pre-exposure prophylaxis, Clin Pharmacol Ther 96(3) (2014) 314-23.
[171] M.A. Tegenge, R.J. Mitkus, A physiologically-based pharmacokinetic (PBPK) model of squalene-containing adjuvant in human vaccines, J Pharmacokinet Pharmacodyn 40(5) (2013) 545-56.
[172] P. Martin, M. Giardiello, T.O. McDonald, S.P. Rannard, A. Owen, Mediation of in vitro cytochrome p450 activity by common pharmaceutical excipients, Mol Pharm 10(7) (2013) 2739-48.
[173] R. Gurjar, C.Y.S. Chan, P. Curley, J. Sharp, J. Chiong, S. Rannard, M. Siccardi, A. Owen, Inhibitory Effects of Commonly Used Excipients on P-Glycoprotein in Vitro, Mol Pharm 15(11) (2018) 4835-4842.
[174] T.R. Buggins, P.A. Dickinson, G. Taylor, The effects of pharmaceutical excipients on drug disposition, Adv Drug Deliv Rev 59(15) (2007) 1482-503.
[175] M.H. Baumann, D. Zolkowska, I. Kim, K.B. Scheidweiler, R.B. Rothman, M.A. Huestis, Effects of dose and route of administration on pharmacokinetics of (+ or -)-3,4-methylenedioxymethamphetamine in the rat, Drug Metab Dispos 37(11) (2009) 2163-70.
[176] P.L. Toutain, A. Ferran, A. Bousquet-Melou, Species differences in pharmacokinetics and pharmacodynamics, Handb Exp Pharmacol (199) (2010) 19-48.
[177] O.P. Soldin, D.R. Mattison, Sex differences in pharmacokinetics and pharmacodynamics, Clin Pharmacokinet 48(3) (2009) 143-57.
[178] C. Tesseromatis, A. Alevizou, The role of the protein-binding on the mode of drug action as well the interactions with other drugs, Eur J Drug Metab Pharmacokinet 33(4) (2008) 225-30.
[179] B.D. Kevadiya, C. Woldstad, B.M. Ottemann, P. Dash, B.R. Sajja, B. Lamberty, B. Morsey, T. Kocher, R. Dutta, A.N. Bade, Y. Liu, S.E. Callen, H.S. Fox, S.N. Byrareddy, J.M. McMillan, T.K. Bronich, B.J. Edagwa, M.D. Boska, H.E. Gendelman, Multimodal Theranostic Nanoformulations Permit Magnetic Resonance Bioimaging of Antiretroviral Drug Particle Tissue-Cell Biodistribution, Theranostics 8(1) (2018) 256-276.
[180] T. Lammers, S. Aime, W.E. Hennink, G. Storm, F. Kiessling, Theranostic nanomedicine, Acc Chem Res 44(10) (2011) 1029-38.
[181] J.H. Scatliff, P.J. Morris, From Roentgen to magnetic resonance imaging: the history of medical imaging, N C Med J 75(2) (2014) 111-3.
[182] V.C. Pierre, M.J. Allen, P. Caravan, Contrast agents for MRI: 30+ years and where are we going?, J Biol Inorg Chem 19(2) (2014) 127-31.
[183] Y.D. Xiao, R. Paudel, J. Liu, C. Ma, Z.S. Zhang, S.K. Zhou, MRI contrast agents: Classification and application (Review), Int J Mol Med 38(5) (2016) 1319-1326.

[184] A. Neuwelt, N. Sidhu, C.A. Hu, G. Mlady, S.C. Eberhardt, L.O. Sillerud, Iron-based superparamagnetic nanoparticle contrast agents for MRI of infection and inflammation, AJR Am J Roentgenol 204(3) (2015) W302-13.
[185] B. Bybel, R.C. Brunken, F.P. DiFilippo, D.R. Neumann, G. Wu, M.D. Cerqueira, SPECT/CT imaging: clinical utility of an emerging technology, Radiographics 28(4) (2008) 1097-113.
[186] E.W. Price, C. Orvig, Matching chelators to radiometals for radiopharmaceuticals, Chemical Society Reviews 43(1) (2014) 260-290.
[187] P. Zanzonico, Principles of nuclear medicine imaging: planar, SPECT, PET, multi-modality, and autoradiography systems, Radiat Res 177(4) (2012) 349-64.
[188] G. Sun, J. Xu, A. Hagooly, R. Rossin, Z. Li, D.A. Moore, C.J. Hawker, M.J. Welch, K.L. Wooley, Strategies for Optimized Radiolabeling of Nanoparticles for in vivo PET Imaging, Advanced Materials 19(20) (2007) 3157-3162.
[189] W.G. Kreyling, A.M. Abdelmonem, Z. Ali, F. Alves, M. Geiser, N. Haberl, R. Hartmann, S. Hirn, D.J. de Aberasturi, K. Kantner, G. Khadem-Saba, J.M. Montenegro, J. Rejman, T. Rojo, I.R. de Larramendi, R. Ufartes, A. Wenk, W.J. Parak, In vivo integrity of polymer-coated gold nanoparticles, Nat Nanotechnol 10(7) (2015) 619-23.
[190] M.L. Schipper, G. Iyer, A.L. Koh, Z. Cheng, Y. Ebenstein, A. Aharoni, S. Keren, L.A. Bentolila, J. Li, J. Rao, X. Chen, U. Banin, A.M. Wu, R. Sinclair, S. Weiss, S.S. Gambhir, Particle size, surface coating, and PEGylation influence the biodistribution of quantum dots in living mice, Small 5(1) (2009) 126-34.
[191] S. Goel, F. Chen, E.B. Ehlerding, W. Cai, Intrinsically radiolabeled nanoparticles: an emerging paradigm, Small 10(19) (2014) 3825-30.
[192] F. Chen, P.A. Ellison, C.M. Lewis, H. Hong, Y. Zhang, S. Shi, R. Hernandez, M.E. Meyerand, T.E. Barnhart, W. Cai, Chelator-free synthesis of a dual-modality PET/MRI agent, Angew Chem Int Ed Engl 52(50) (2013) 13319-23.
[193] E. Aluicio-Sarduy, P.A. Ellison, T.E. Barnhart, W. Cai, R.J. Nickles, J.W. Engle, PET radiometals for antibody labeling, J Labelled Comp Radiopharm 61(9) (2018) 636-651.
[194] A.F.L. Schneider, C.P.R. Hackenberger, Fluorescent labelling in living cells, Curr Opin Biotechnol 48 (2017) 61-68.
[195] G. Liu, Advances in the theoretical understanding of photon upconversion in rare-earth activated nanophosphors, Chem Soc Rev 44(6) (2015) 1635-52.
[196] B.D. Kevadiya, A.N. Bade, C. Woldstad, B.J. Edagwa, J.M. McMillan, B.R. Sajja, M.D. Boska, H.E. Gendelman, Development of europium doped core-shell silica cobalt ferrite functionalized nanoparticles for magnetic resonance imaging, Acta Biomater 49 (2017) 507-520.
[197] D. Singh, J. McMillan, J. Hilaire, N. Gautam, D. Palandri, Y. Alnouti, H.E. Gendelman, B. Edagwa, Development and characterization of a long-acting nanoformulated abacavir prodrug, Nanomedicine (Lond) 11(15) (2016) 1913-27.
[198] D.Y. Lu, H.Y. Wu, N.S. Yarla, B. Xu, J. Ding, T.R. Lu, HAART in HIV/AIDS Treatments: Future Trends, Infect Disord Drug Targets 18(1) (2018) 15-22.
[199] M. Sharma, L.D. Saravolatz, Rilpivirine: a new non-nucleoside reverse transcriptase inhibitor, J Antimicrob Chemother 68(2) (2013) 250-6.

[200] F.F. Hong, J.W. Mellors, Impact of Antiretroviral Therapy on HIV-1 Persistence: The Case for Early Initiation, AIDS Rev 17(2) (2015) 71-82.
[201] C. Antiretroviral Therapy Cohort, Life expectancy of individuals on combination antiretroviral therapy in high-income countries: a collaborative analysis of 14 cohort studies, Lancet 372(9635) (2008) 293-9.
[202] P.R. Harrigan, R.S. Hogg, W.W. Dong, B. Yip, B. Wynhoven, J. Woodward, C.J. Brumme, Z.L. Brumme, T. Mo, C.S. Alexander, J.S. Montaner, Predictors of HIV drug-resistance mutations in a large antiretroviral-naive cohort initiating triple antiretroviral therapy, J Infect Dis 191(3) (2005) 339-47.
[203] D. Saylor, A.M. Dickens, N. Sacktor, N. Haughey, B. Slusher, M. Pletnikov, J.L. Mankowski, A. Brown, D.J. Volsky, J.C. McArthur, HIV-associated neurocognitive disorder--pathogenesis and prospects for treatment, Nat Rev Neurol 12(4) (2016) 234-48.
[204] B.J. Edagwa, T. Zhou, J.M. McMillan, X.M. Liu, H.E. Gendelman, Development of HIV reservoir targeted long acting nanoformulated antiretroviral therapies, Curr Med Chem 21(36) (2014) 4186-98.
[205] E.L. Ross, M.C. Weinstein, B.R. Schackman, P.E. Sax, A.D. Paltiel, R.P. Walensky, K.A. Freedberg, E. Losina, The clinical role and cost-effectiveness of long-acting antiretroviral therapy, Clin Infect Dis 60(7) (2015) 1102-10.
[206] J.K. Wong, S.A. Yukl, Tissue reservoirs of HIV, Curr Opin HIV AIDS 11(4) (2016) 362-70.
[207] K.N. Althoff, S.J. Gange, A critical epidemiological review of cardiovascular disease risk in HIV-infected adults: the importance of the HIV-uninfected comparison group, confounding, and competing risks, HIV Med 14(3) (2013) 191-2.
[208] C. Hadigan, S. Kattakuzhy, Diabetes mellitus type 2 and abnormal glucose metabolism in the setting of human immunodeficiency virus, Endocrinol Metab Clin North Am 43(3) (2014) 685-96.
[209] G.V. Escota, K. Mondy, T. Bush, L. Conley, J.T. Brooks, N. Onen, P. Patel, E.M. Kojic, K. Henry, J. Hammer, K.C. Wood, K.A. Lichtenstein, E.T. Overton, High Prevalence of Low Bone Mineral Density and Substantial Bone Loss over 4 Years Among HIV-Infected Persons in the Era of Modern Antiretroviral Therapy, AIDS Res Hum Retroviruses 32(1) (2016) 59-67.
[210] W.M. El-Sadr, C.M. Mullin, A. Carr, C. Gibert, C. Rappoport, F. Visnegarwala, C. Grunfeld, S.S. Raghavan, Effects of HIV disease on lipid, glucose and insulin levels: results from a large antiretroviral-naive cohort, HIV Med 6(2) (2005) 114-21.
[211] C. Eggers, G. Arendt, K. Hahn, I.W. Husstedt, M. Maschke, E. Neuen-Jacob, M. Obermann, T. Rosenkranz, E. Schielke, E. Straube, A.u.N.-I. German Association of Neuro, HIV-1-associated neurocognitive disorder: epidemiology, pathogenesis, diagnosis, and treatment, J Neurol 264(8) (2017) 1715-1727.
[212] S. Choudhary, Latent HIV-1 Infection of Resting CD4+ T cells: Testing Approaches to Overcome HIV Latency, 2014.
[213] C.D. Andrews, W. Heneine, Cabotegravir long-acting for HIV-1 prevention, Curr Opin HIV AIDS 10(4) (2015) 258-63.

[214] M. Araínga, B. Edagwa, R.L. Mosley, L.Y. Poluektova, S. Gorantla, H.E. Gendelman, A mature macrophage is a principal HIV-1 cellular reservoir in humanized mice after treatment with long acting antiretroviral therapy, Retrovirology 14(1) (2017) 17.
[215] R.J. Landovitz, R. Kofron, M. McCauley, The promise and pitfalls of long-acting injectable agents for HIV prevention, Curr Opin HIV AIDS 11(1) (2016) 122-8.
[216] D.A. Margolis, C.C. Brinson, G.H.R. Smith, J. de Vente, D.P. Hagins, J.J. Eron, S.K. Griffith, M.H.S. Clair, M.C. Stevens, P.E. Williams, S.L. Ford, B.S. Stancil, M.M. Bomar, K.J. Hudson, K.Y. Smith, W.R. Spreen, L.A.I.S. Team, Cabotegravir plus rilpivirine, once a day, after induction with cabotegravir plus nucleoside reverse transcriptase inhibitors in antiretroviral-naive adults with HIV-1 infection (LATTE): a randomised, phase 2b, dose-ranging trial, Lancet Infect Dis 15(10) (2015) 1145-1155.
[217] W.R. Spreen, D.A. Margolis, J.C. Pottage, Jr., Long-acting injectable antiretrovirals for HIV treatment and prevention, Curr Opin HIV AIDS 8(6) (2013) 565-71.
[218] A.H.F. Andersen, C.F. Riber, K. Zuwala, M. Tolstrup, F. Dagnæs-Hansen, P.W. Denton, A.N. Zelikin, Long-Acting, Potent Delivery of Combination Antiretroviral Therapy, ACS Macro Letters 7(5) (2018) 587-591.
[219] D.P. Gnanadhas, P.K. Dash, B. Sillman, A.N. Bade, Z. Lin, D.L. Palandri, N. Gautam, Y. Alnouti, H.A. Gelbard, J. McMillan, R.L. Mosley, B. Edagwa, H.E. Gendelman, S. Gorantla, Autophagy facilitates macrophage depots of sustained-release nanoformulated antiretroviral drugs, J Clin Invest 127(3) (2017) 857-873.
[220] W. Chen, G. Wang, B.C. Yung, G. Liu, Z. Qian, X. Chen, Long-Acting Release Formulation of Exendin-4 Based on Biomimetic Mineralization for Type 2 Diabetes Therapy, ACS Nano 11(5) (2017) 5062-5069.
[221] S.F. Chou, D. Carson, K.A. Woodrow, Current strategies for sustaining drug release from electrospun nanofibers, J Control Release 220(Pt B) (2015) 584-91.
[222] J. Radzio, W. Spreen, Y.L. Yueh, J. Mitchell, L. Jenkins, J.G. Garcia-Lerma, W. Heneine, The long-acting integrase inhibitor GSK744 protects macaques from repeated intravaginal SHIV challenge, Sci Transl Med 7(270) (2015) 270ra5.
[223] M.W. Tibbitt, J.E. Dahlman, R. Langer, Emerging Frontiers in Drug Delivery, J Am Chem Soc 138(3) (2016) 704-17.
[224] M. Siccardi, S. Rannard, A. Owen, The emerging role of physiologically based pharmacokinetic modelling in solid drug nanoparticle translation, Adv Drug Deliv Rev 131 (2018) 116-121.
[225] B. Mandal, N.K. Mittal, P. Balabathula, L.A. Thoma, G.C. Wood, Development and in vitro evaluation of core-shell type lipid-polymer hybrid nanoparticles for the delivery of erlotinib in non-small cell lung cancer, Eur J Pharm Sci 81 (2016) 162-71.
[226] S. Krishnamurthy, R. Vaiyapuri, L. Zhang, J.M. Chan, Lipid-coated polymeric nanoparticles for cancer drug delivery, Biomater Sci 3(7) (2015) 923-36.

[227] P. Puligujja, S.S. Balkundi, L.M. Kendrick, H.M. Baldridge, J.R. Hilaire, A.N. Bade, P.K. Dash, G. Zhang, L.Y. Poluektova, S. Gorantla, X.M. Liu, T. Ying, Y. Feng, Y. Wang, D.S. Dimitrov, J.M. McMillan, H.E. Gendelman, Pharmacodynamics of long-acting folic acid-receptor targeted ritonavir-boosted atazanavir nanoformulations, Biomaterials 41 (2015) 141-50.
[228] S. Sengupta, D. Eavarone, I. Capila, G. Zhao, N. Watson, T. Kiziltepe, R. Sasisekharan, Temporal targeting of tumour cells and neovasculature with a nanoscale delivery system, Nature 436(7050) (2005) 568-72.
[229] T.J. Merkel, K. Chen, S.W. Jones, A.A. Pandya, S. Tian, M.E. Napier, W.E. Zamboni, J.M. DeSimone, The effect of particle size on the biodistribution of low-modulus hydrogel PRINT particles, J Control Release 162(1) (2012) 37-44.
[230] S. Hirn, M. Semmler-Behnke, C. Schleh, A. Wenk, J. Lipka, M. Schaffler, S. Takenaka, W. Moller, G. Schmid, U. Simon, W.G. Kreyling, Particle size-dependent and surface charge-dependent biodistribution of gold nanoparticles after intravenous administration, Eur J Pharm Biopharm 77(3) (2011) 407-16.
[231] H.E. Gendelman, J.M. Orenstein, M.A. Martin, C. Ferrua, R. Mitra, T. Phipps, L.A. Wahl, H.C. Lane, A.S. Fauci, D.S. Burke, et al., Efficient isolation and propagation of human immunodeficiency virus on recombinant colony-stimulating factor 1-treated monocytes, J Exp Med 167(4) (1988) 1428-41.
[232] T. Mosmann, Rapid colorimetric assay for cellular growth and survival: application to proliferation and cytotoxicity assays, J Immunol Methods 65(1-2) (1983) 55-63.
[233] S.A. MacParland, K.M. Tsoi, B. Ouyang, X.Z. Ma, J. Manuel, A. Fawaz, M.A. Ostrowski, B.A. Alman, A. Zilman, W.C. Chan, I.D. McGilvray, Phenotype Determines Nanoparticle Uptake by Human Macrophages from Liver and Blood, ACS Nano 11(3) (2017) 2428-2443.
[234] S. Venkatesan, N. Kannappan, Simultaneous Spectrophotometric Method for Determination of Emtricitabine and Tenofovir Disoproxil Fumarate in Three-Component Tablet Formulation Containing Rilpivirine Hydrochloride, Int Sch Res Notices 2014 (2014) 541727.
[235] I. Kadiu, A. Nowacek, J. McMillan, H.E. Gendelman, Macrophage endocytic trafficking of antiretroviral nanoparticles, Nanomedicine (Lond) 6(6) (2011) 975-94.
[236] D. Guo, G. Zhang, T.A. Wysocki, B.J. Wysocki, H.A. Gelbard, X.M. Liu, J.M. McMillan, H.E. Gendelman, Endosomal trafficking of nanoformulated antiretroviral therapy facilitates drug particle carriage and HIV clearance, J Virol 88(17) (2014) 9504-13.
[237] S.A. MacParland, K.M. Tsoi, B. Ouyang, X.-Z. Ma, J. Manuel, A. Fawaz, M.A. Ostrowski, B.A. Alman, A. Zilman, W.C.W. Chan, I.D. McGilvray, Phenotype Determines Nanoparticle Uptake by Human Macrophages from Liver and Blood, ACS Nano 11(3) (2017) 2428-2443.
[238] R.M. Zucker, J.N. Ortenzio, W.K. Boyes, Characterization, detection, and counting of metal nanoparticles using flow cytometry, Cytometry A 89(2) (2016) 169-83.

[239] D.C. Kalter, H.E. Gendelman, M.S. Meltzer, Inhibition of human immunodeficiency virus infection in monocytes by monoclonal antibodies against leukocyte adhesion molecules, Immunol Lett 30(2) (1991) 219-27.
[240] Z. Xu, C. Shen, Y. Hou, H. Gao, S. Sun, Oleylamine as Both Reducing Agent and Stabilizer in a Facile Synthesis of Magnetite Nanoparticles, Chemistry of Materials 21(9) (2009) 1778-1780.
[241] M. Kovarova, O.D. Council, A.A. Date, J.M. Long, T. Nochi, M. Belshan, A. Shibata, H. Vincent, C.E. Baker, W.O. Thayer, G. Kraus, S. Lachaud-Durand, P. Williams, C.J. Destache, J.V. Garcia, Nanoformulations of Rilpivirine for Topical Pericoital and Systemic Coitus-Independent Administration Efficiently Prevent HIV Transmission, PLoS Pathog 11(8) (2015) e1005075.
[242] S. Md, M. Ali, S. Baboota, J.K. Sahni, A. Bhatnagar, J. Ali, Preparation, characterization, in vivo biodistribution and pharmacokinetic studies of donepezil-loaded PLGA nanoparticles for brain targeting, Drug Dev Ind Pharm 40(2) (2014) 278-87.
[243] D.D. Sun, P.I. Lee, Evolution of supersaturation of amorphous pharmaceuticals: the effect of rate of supersaturation generation, Mol Pharm 10(11) (2013) 4330-46.
[244] D. Hirayama, T. Iida, H. Nakase, The Phagocytic Function of Macrophage-Enforcing Innate Immunity and Tissue Homeostasis, Int J Mol Sci 19(1) (2017).
[245] R. van Furth, Z.A. Cohn, J.G. Hirsch, J.H. Humphrey, W.G. Spector, H.L. Langevoort, The mononuclear phagocyte system: a new classification of macrophages, monocytes, and their precursor cells, Bull World Health Organ 46(6) (1972) 845-52.
[246] J. Herskovitz, H.E. Gendelman, HIV and the Macrophage: From Cell Reservoirs to Drug Delivery to Viral Eradication, J Neuroimmune Pharmacol 14(1) (2019) 52-67.
[247] P. Puligujja, J. McMillan, L. Kendrick, T. Li, S. Balkundi, N. Smith, R.S. Veerubhotla, B.J. Edagwa, A.V. Kabanov, T. Bronich, H.E. Gendelman, X.M. Liu, Macrophage folate receptor-targeted antiretroviral therapy facilitates drug entry, retention, antiretroviral activities and biodistribution for reduction of human immunodeficiency virus infections, Nanomedicine 9(8) (2013) 1263-73.
[248] P.G. Jamkhande, M.H. Ghante, B.R. Ajgunde, Software based approaches for drug designing and development: A systematic review on commonly used software and its applications, Bulletin of Faculty of Pharmacy, Cairo University 55(2) (2017) 203-210.
[249] J.M. Pellock, S.T. Brittain, Use of computer simulations to test the concept of dose forgiveness in the era of extended-release (XR) drugs, Epilepsy Behav 55 (2016) 21-3.
[250] L. Miyamoto, M. Watanabe, C. Taoka, M. Kono, Y. Tomida, T. Matsushita, M. Kamiya, H. Hattori, K. Ishizawa, S. Abe, H. Nemoto, K. Tsuchiya, A novel prodrug strategy for extremely hydrophobic agents: conjugation to symmetrically branched glycerol trimer improves pharmacological and pharmacokinetic properties of fenofibrate, Mol Pharm 10(7) (2013) 2723-9.
[251] T. Zhou, H. Su, P. Dash, Z. Lin, B.L. Dyavar Shetty, T. Kocher, A. Szlachetka, B. Lamberty, H.S. Fox, L. Poluektova, S. Gorantla, J. McMillan, N.

Gautam, R.L. Mosley, Y. Alnouti, B. Edagwa, H.E. Gendelman, Creation of a nanoformulated cabotegravir prodrug with improved antiretroviral profiles, Biomaterials 151 (2018) 53-65.
[252] A. Hajitou, D.C. Lev, J.A. Hannay, B. Korchin, F.I. Staquicini, S. Soghomonyan, M.M. Alauddin, R.S. Benjamin, R.E. Pollock, J.G. Gelovani, R. Pasqualini, W. Arap, A preclinical model for predicting drug response in soft-tissue sarcoma with targeted AAVP molecular imaging, Proc Natl Acad Sci U S A 105(11) (2008) 4471-6.
[253] Y. Li, T.Y. Lin, Y. Luo, Q. Liu, W. Xiao, W. Guo, D. Lac, H. Zhang, C. Feng, S. Wachsmann-Hogiu, J.H. Walton, S.R. Cherry, D.J. Rowland, D. Kukis, C. Pan, K.S. Lam, A smart and versatile theranostic nanomedicine platform based on nanoporphyrin, Nat Commun 5 (2014) 4712.
[254] A.J. Clark, M.E. Davis, Increased brain uptake of targeted nanoparticles by adding an acid-cleavable linkage between transferrin and the nanoparticle core, Proc Natl Acad Sci U S A 112(40) (2015) 12486-91.
[255] I.J. de Vries, W.J. Lesterhuis, J.O. Barentsz, P. Verdijk, J.H. van Krieken, O.C. Boerman, W.J. Oyen, J.J. Bonenkamp, J.B. Boezeman, G.J. Adema, J.W. Bulte, T.W. Scheenen, C.J. Punt, A. Heerschap, C.G. Figdor, Magnetic resonance tracking of dendritic cells in melanoma patients for monitoring of cellular therapy, Nat Biotechnol 23(11) (2005) 1407-13.
[256] K. Allers, A. Puyskens, H.J. Epple, D. Schurmann, J. Hofmann, V. Moos, T. Schneider, The effect of timing of antiretroviral therapy on CD4+ T-cell reconstitution in the intestine of HIV-infected patients, Mucosal Immunol 9(1) (2016) 265-74.
[257] Z. Zhao, Z. Zhou, J. Bao, Z. Wang, J. Hu, X. Chi, K. Ni, R. Wang, X. Chen, Z. Chen, J. Gao, Octapod iron oxide nanoparticles as high-performance T(2) contrast agents for magnetic resonance imaging, Nat Commun 4 (2013) 2266.
[258] Y. Bao, J.A. Sherwood, Z. Sun, Magnetic iron oxide nanoparticles as T1 contrast agents for magnetic resonance imaging, Journal of Materials Chemistry C 6(6) (2018) 1280-1290.
[259] J. Estelrich, M.J. Sanchez-Martin, M.A. Busquets, Nanoparticles in magnetic resonance imaging: from simple to dual contrast agents, Int J Nanomedicine 10 (2015) 1727-41.
[260] J.S. Choi, J.C. Park, H. Nah, S. Woo, J. Oh, K.M. Kim, G.J. Cheon, Y. Chang, J. Yoo, J. Cheon, A hybrid nanoparticle probe for dual-modality positron emission tomography and magnetic resonance imaging, Angew Chem Int Ed Engl 47(33) (2008) 6259-62.
[261] X. Cui, D. Mathe, N. Kovacs, I. Horvath, M. Jauregui-Osoro, R. Torres Martin de Rosales, G.E. Mullen, W. Wong, Y. Yan, D. Kruger, A.N. Khlobystov, M. Gimenez-Lopez, M. Semjeni, K. Szigeti, D.S. Veres, H. Lu, I. Hernandez, W.P. Gillin, A. Protti, K.K. Petik, M.A. Green, P.J. Blower, Synthesis, Characterization, and Application of Core-Shell Co0.16Fe2.84O4@NaYF4(Yb, Er) and Fe3O4@NaYF4(Yb, Tm) Nanoparticle as Trimodal (MRI, PET/SPECT, and Optical) Imaging Agents, Bioconjug Chem 27(2) (2016) 319-28.
[262] L. Sandiford, A. Phinikaridou, A. Protti, L.K. Meszaros, X. Cui, Y. Yan, G. Frodsham, P.A. Williamson, N. Gaddum, R.M. Botnar, P.J. Blower, M.A. Green,

R.T. de Rosales, Bisphosphonate-anchored PEGylation and radiolabeling of superparamagnetic iron oxide: long-circulating nanoparticles for in vivo multimodal (T1 MRI-SPECT) imaging, ACS Nano 7(1) (2013) 500-12.
[263] L. Cheng, S. Shen, D. Jiang, Q. Jin, P.A. Ellison, E.B. Ehlerding, S. Goel, G. Song, P. Huang, T.E. Barnhart, Z. Liu, W. Cai, Chelator-Free Labeling of Metal Oxide Nanostructures with Zirconium-89 for Positron Emission Tomography Imaging, ACS Nano 11(12) (2017) 12193-12201.
[264] Y. Zhan, E.B. Ehlerding, S. Shi, S.A. Graves, S. Goel, J.W. Engle, J. Liang, W. Cai, Intrinsically Zirconium-89-Labeled Manganese Oxide Nanoparticles for In Vivo Dual-Modality Positron Emission Tomography and Magnetic Resonance Imaging, J Biomed Nanotechnol 14(5) (2018) 900-909.
[265] N. Jiménez-Mancilla, G. Ferro-Flores, C. Santos-Cuevas, B. Ocampo-García, M. Luna-Gutiérrez, E. Azorín-Vega, K. Isaac-Olivé, M. Camacho-López, E. Torres-García, Multifunctional targeted therapy system based on 99mTc/177Lu-labeled gold nanoparticles-Tat(49–57)-Lys3-bombesin internalized in nuclei of prostate cancer cells, Journal of Labelled Compounds and Radiopharmaceuticals 56(13) (2013) 663-671.
[266] M. Zhou, R. Zhang, M. Huang, W. Lu, S. Song, M.P. Melancon, M. Tian, D. Liang, C. Li, A chelator-free multifunctional [64Cu]CuS nanoparticle platform for simultaneous micro-PET/CT imaging and photothermal ablation therapy, J Am Chem Soc 132(43) (2010) 15351-8.
[267] R. Chakravarty, H.F. Valdovinos, F. Chen, C.M. Lewis, P.A. Ellison, H. Luo, M.E. Meyerand, R.J. Nickles, W. Cai, Intrinsically germanium-69-labeled iron oxide nanoparticles: synthesis and in-vivo dual-modality PET/MR imaging, Adv Mater 26(30) (2014) 5119-23.
[268] P.A. Ellison, F. Chen, S. Goel, T.E. Barnhart, R.J. Nickles, O.T. DeJesus, W. Cai, Intrinsic and Stable Conjugation of Thiolated Mesoporous Silica Nanoparticles with Radioarsenic, ACS Appl Mater Interfaces 9(8) (2017) 6772-6781.
[269] M.J. Gilkey, V. Krishnan, L. Scheetz, X. Jia, A.K. Rajasekaran, P.S. Dhurjati, Physiologically Based Pharmacokinetic Modeling of Fluorescently Labeled Block Copolymer Nanoparticles for Controlled Drug Delivery in Leukemia Therapy, CPT Pharmacometrics Syst Pharmacol 4(3) (2015) e00013.
[270] M.F. Taddio, L. Mu, C. Keller, R. Schibli, S.D. Kramer, Physiologically Based Pharmacokinetic Modelling with Dynamic PET Data to Study the In Vivo Effects of Transporter Inhibition on Hepatobiliary Clearance in Mice, Contrast Media Mol Imaging 2018 (2018) 5849047.
[271] I. Sorrell, R.J. Shipley, V. Hearnden, H.E. Colley, M.H. Thornhill, C. Murdoch, S.D. Webb, Combined mathematical modelling and experimentation to predict polymersome uptake by oral cancer cells, Nanomedicine 10(2) (2014) 339-48.
[272] J.V. Jokerst, T. Lobovkina, R.N. Zare, S.S. Gambhir, Nanoparticle PEGylation for imaging and therapy, Nanomedicine (Lond) 6(4) (2011) 715-28.
[273] M. Balasubramaniam, E.O. Freed, New insights into HIV assembly and trafficking, Physiology (Bethesda) 26(4) (2011) 236-51.

[274] A. Nowacek, I. Kadiu, J. McMillan, H.E. Gendelman, Methods for isolation and identification of nanoparticle-containing subcellular compartments, Methods Mol Biol 991 (2013) 47-55.
[275] H. Wu, G. Liu, X. Wang, J. Zhang, Y. Chen, J. Shi, H. Yang, H. Hu, S. Yang, Solvothermal synthesis of cobalt ferrite nanoparticles loaded on multiwalled carbon nanotubes for magnetic resonance imaging and drug delivery, Acta Biomater 7(9) (2011) 3496-504.
[276] G. Allaedini, S.M. Tasirin, P. Aminayi, Magnetic properties of cobalt ferrite synthesized by hydrothermal method, International Nano Letters 5(4) (2015) 183-186.
[277] H. Borges da Silva, R. Fonseca, R.M. Pereira, A. Cassado Ados, J.M. Alvarez, M.R. D'Imperio Lima, Splenic Macrophage Subsets and Their Function during Blood-Borne Infections, Front Immunol 6 (2015) 480.
[278] H.C. Huang, P.Y. Chang, K. Chang, C.Y. Chen, C.W. Lin, J.H. Chen, C.Y. Mou, Z.F. Chang, F.H. Chang, Formulation of novel lipid-coated magnetic nanoparticles as the probe for in vivo imaging, J Biomed Sci 16 (2009) 86.
[279] N. Doshi, S. Mitragotri, Macrophages Recognize Size and Shape of Their Targets, PLOS ONE 5(4) (2010) e10051.
[280] R. Kaminski, Y. Chen, T. Fischer, E. Tedaldi, A. Napoli, Y. Zhang, J. Karn, W. Hu, K. Khalili, Elimination of HIV-1 Genomes from Human T-lymphoid Cells by CRISPR/Cas9 Gene Editing, Sci Rep 6 (2016) 22555.
[281] A. Tsai, A. Irrinki, J. Kaur, T. Cihlar, G. Kukolj, D.D. Sloan, J.P. Murry, Toll-Like Receptor 7 Agonist GS-9620 Induces HIV Expression and HIV-Specific Immunity in Cells from HIV-Infected Individuals on Suppressive Antiretroviral Therapy, J Virol 91(8) (2017).
[282] T.Y. Hu, Multidisciplinary efforts driving translational theranostics, Theranostics 4(12) (2014) 1209-10.
[283] F.R. Vogenberg, C. Isaacson Barash, M. Pursel, Personalized medicine: part 1: evolution and development into theranostics, P T 35(10) (2010) 560-76.
[284] B.M. Ottemann, A.J. Helmink, W. Zhang, I. Mukadam, C. Woldstad, J.R. Hilaire, Y. Liu, J.M. McMillan, B.J. Edagwa, R.L. Mosley, J.C. Garrison, B.D. Kevadiya, H.E. Gendelman, Bioimaging predictors of rilpivirine biodistribution and antiretroviral activities, Biomaterials 185 (2018) 174-193.
[285] E.L. Schneider, J. Henise, R. Reid, G.W. Ashley, D.V. Santi, Subcutaneously Administered Self-Cleaving Hydrogel-Octreotide Conjugates Provide Very Long-Acting Octreotide, Bioconjug Chem 27(7) (2016) 1638-44.
[286] J. Du, Y.S. Zhang, D. Hobson, P. Hydbring, Nanoparticles for immune system targeting, Drug Discov Today 22(9) (2017) 1295-1301.
[287] J. Shi, P.W. Kantoff, R. Wooster, O.C. Farokhzad, Cancer nanomedicine: progress, challenges and opportunities, Nat Rev Cancer 17(1) (2017) 20-37.
[288] R. Savla, T. Minko, Nanoparticle design considerations for molecular imaging of apoptosis: Diagnostic, prognostic, and therapeutic value, Adv Drug Deliv Rev 113 (2017) 122-140.
[289] K.X. Tan, M.K. Danquah, A. Sidhu, L.S. Yon, C.M. Ongkudon, Aptamer-Mediated Polymeric Vehicles for Enhanced Cell-Targeted Drug Delivery, Curr Drug Targets 19(3) (2018) 248-258.

[290] V.H. Shargh, H. Hondermarck, M. Liang, Antibody-targeted biodegradable nanoparticles for cancer therapy, Nanomedicine (Lond) 11(1) (2016) 63-79.
[291] J. Look, N. Wilhelm, H. von Briesen, N. Noske, C. Gunther, K. Langer, E. Gorjup, Ligand-Modified Human Serum Albumin Nanoparticles for Enhanced Gene Delivery, Mol Pharm 12(9) (2015) 3202-13.
[292] L.D. Field, J.B. Delehanty, Y. Chen, I.L. Medintz, Peptides for specifically targeting nanoparticles to cellular organelles: quo vadis?, Acc Chem Res 48(5) (2015) 1380-90.
[293] L.N. Ramana, A.R. Anand, S. Sethuraman, U.M. Krishnan, Targeting strategies for delivery of anti-HIV drugs, J Control Release 192 (2014) 271-83.
[294] A.N. Endsley, R.J. Ho, Enhanced anti-HIV efficacy of indinavir after inclusion in CD4-targeted lipid nanoparticles, J Acquir Immune Defic Syndr 61(4) (2012) 417-24.
[295] M. Kovochich, M.D. Marsden, J.A. Zack, Activation of latent HIV using drug-loaded nanoparticles, PLoS One 6(4) (2011) e18270.
[296] S.S. Kim, D. Peer, P. Kumar, S. Subramanya, H. Wu, D. Asthana, K. Habiro, Y.G. Yang, N. Manjunath, M. Shimaoka, P. Shankar, RNAi-mediated CCR5 silencing by LFA-1-targeted nanoparticles prevents HIV infection in BLT mice, Mol Ther 18(2) (2010) 370-6.
[297] S. Nie, Understanding and overcoming major barriers in cancer nanomedicine, Nanomedicine (Lond) 5(4) (2010) 523-8.
[298] F.A. Harding, M.M. Stickler, J. Razo, R.B. DuBridge, The immunogenicity of humanized and fully human antibodies: residual immunogenicity resides in the CDR regions, MAbs 2(3) (2010) 256-65.
[299] M.J. Rohovie, M. Nagasawa, J.R. Swartz, Virus-like particles: Next-generation nanoparticles for targeted therapeutic delivery, Bioeng Transl Med 2(1) (2017) 43-57.
[300] F.K. Schur, W.J. Hagen, M. Rumlova, T. Ruml, B. Muller, H.G. Krausslich, J.A. Briggs, Structure of the immature HIV-1 capsid in intact virus particles at 8.8 A resolution, Nature 517(7535) (2015) 505-8.
[301] P. Singh, M.J. Gonzalez, M. Manchester, Viruses and their uses in nanotechnology, Drug Development Research 67(1) (2006) 23-41.
[302] P.K. Dash, R. Kaminski, R. Bella, H. Su, S. Mathews, T.M. Ahooyi, C. Chen, P. Mancuso, R. Sariyer, P. Ferrante, M. Donadoni, J.A. Robinson, B. Sillman, Z. Lin, J.R. Hilaire, M. Banoub, M. Elango, N. Gautam, R.L. Mosley, L.Y. Poluektova, J. McMillan, A.N. Bade, S. Gorantla, I.K. Sariyer, T.H. Burdo, W.B. Young, S. Amini, J. Gordon, J.M. Jacobson, B. Edagwa, K. Khalili, H.E. Gendelman, Sequential LASER ART and CRISPR Treatments Eliminate HIV-1 in a Subset of Infected Humanized Mice, Nat Commun 10(1) (2019) 2753.